Particle Degradation during Vertical Transportation

Contribution of Abrasive Wear on Polymetallic Nodule Degradation

J.T.M. Wijnands

Technische Universiteit Delft

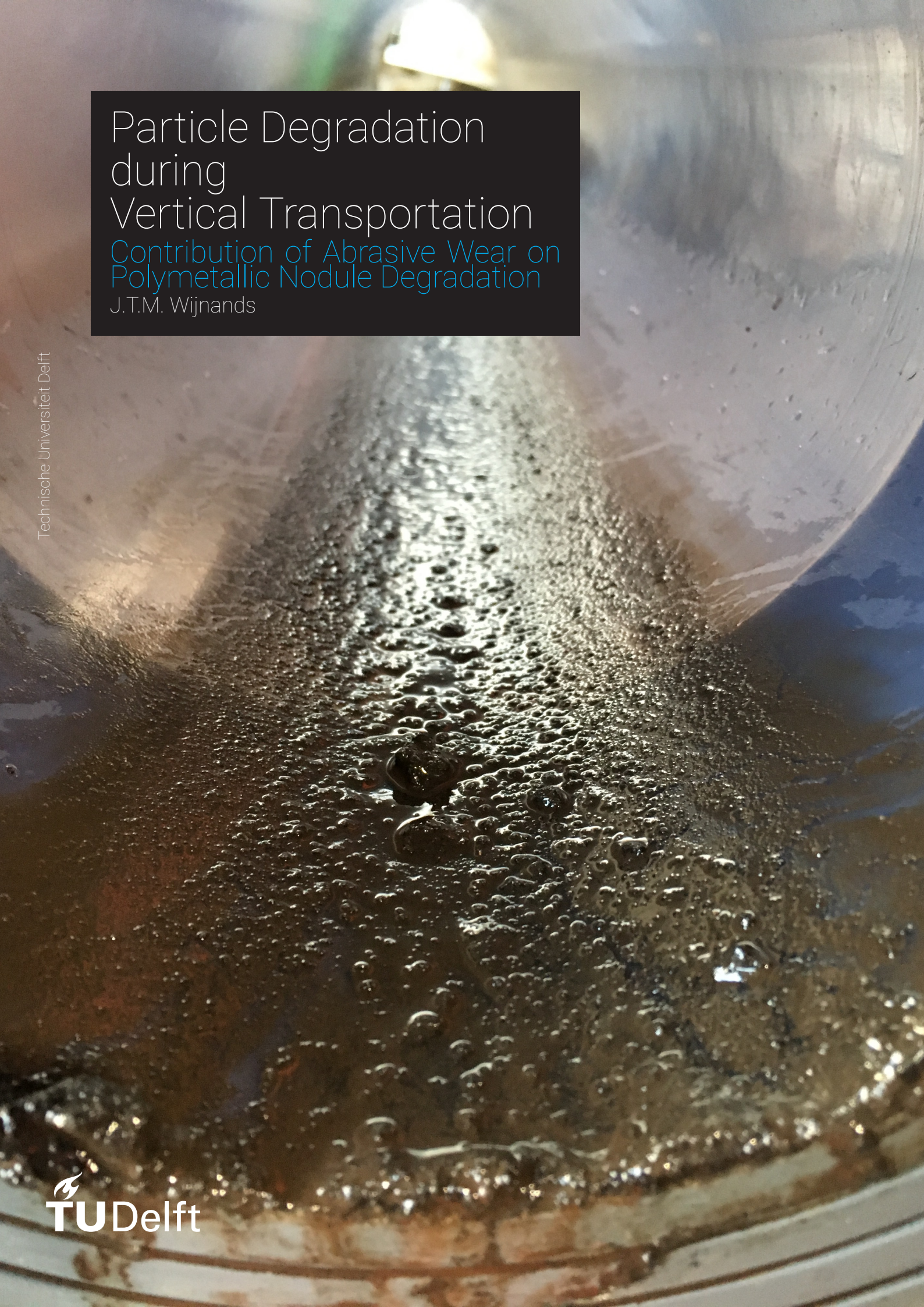

TU Delft

Particle Degradation during Vertical Transportation

Contribution of Abrasive Wear on Polymetallic Nodule Degradation

by

J.T.M. Wijnands

to obtain the degree of Master of Science
at the Delft University of Technology,
to be defended publicly on Wednesday December 19, 2018 at 1:30 PM.

Student number:	4096231	
MTI report number:	AO161	
Project duration:	September 18, 2017 – December 19, 2018	
Thesis committee:	Prof. dr. ir. C. van Rhee	TU Delft
	Dr. ir. A.M. Talmon	TU Delft
	Dr. ir. W.P. Breugem	TU Delft
	Ir. E. de Hoog	IHC MTI

This thesis is confidential and cannot be made public until December 19, 2018.

TU Delft

Abstract

Manganese nodules have been lying on the deep sea soil for centuries before they became known. The first ones to discover the nodules were Murray and Renard, during their scientific cruise between 1872 and 1876 (Murray and Renard, 1876). The Clarion-Clipperton Zone, located between Mexico and Hawaii, appears to have a virtually inexhaustible amount of mineral resources. The manganese nodules consist mainly of manganese, but because they also contain metals such as copper and cobalt, the nodules become more and more interesting for our modern society. Another name for the manganese nodules is polymetallic nodules, because of the content of many other metals.

By means of a vertical hydraulic transport system the manganese nodules will be transported upwards from the seabed. Given that the nodules are located at a depth of about 5000 meter, it is plausible that they come into contact with the pipe wall during transport. When a nodule interacts with the wall, abrasive wear can occur. Abrasive wear, or sliding wear, causes the nodule to degrade, or decrease in mass, through the sliding contact with the pipe wall.

The main research question of this Master Thesis is formed as follows:

What is the contribution of abrasive wear to the degradation of polymetallic nodules, in a vertical transport system?

The contribution of abrasive wear is tested on the basis of the equation of Archard (1953). In the MTI laboratory in Kinderdijk various manganese nodules are tested in a specially designed experimental setup. The polymetallic nodules available for this Master Thesis originate from the Clarion-Clipperton Zone (CCZ). The first set of experiments is focused on single nodule degradation. The nodules are weighted before and after a test run, hereafter the nodule mass after a test run is divided by the initial nodule mass, resulting in the normalized remaining mass. Each test run consists of a specific sliding length. With the sliding length and normalized remains mass, a prediction can be made of the material specific wear rate factor, noted as k [m^2/N]. The experiments resulted into a value of $k = 4.16 \cdot 10^{-9}$ [m^2/N]. With this k-factor, in the worst case, 97% of the original nodule mass is remaining after 1000 meters of sliding contact.

Subsequently, a batch of nodules is tested in the experimental setup, with the expectation that the contribution of abrasive wear increases to the total nodule degradation, due to the presence of particle-particle interaction. Recently, Blue Mining has conducted trials in Freiberg, Germany, in an abandoned mine shaft. A vertical pipe of almost 130 meters has been placed inside, and the effect of abrasion on a batch of nodules has been observed. During the batch experiments in Kinderdijk, where the batch of nodules was in a horizontal position, it is seen that the contribution of abrasion is greater, compared to the tests in Freiberg.

Using the open-source program OpenFOAM, a vertical turbulent pipe flow is modeled. The pipe has similar dimensions to the pipe of the experimental setup. The simulation was done using a Large Eddy Simulation (LES). By means of a one-way coupling, the data of the flow field is linked to the movement of the simulated particle. Subsequently, point particles were released at various points at the entrance of the pipe. The first series of point particles consists of a diameter of one-third of the pipe diameter, corresponding to the common size of a manganese nodule. The collisions between the point particle and the pipe wall are solved with a Discrete Element Method (DEM), which makes use of a (non-linear) spring-damper system.

To test the sensitivity of the model, point particles of one-sixth and one-tenth of the pipe diameter are also released. The number of collisions per total number of simulations are compared with each other. After the sensitivity analysis it turned out that in 15% of the simulations there was contact with the pipe wall, regardless of the diameter of the particle. When this 15% is compared to the experimental results using single nodules, there is a weight loss of around 0.5%. This holds a weight loss of only a single - to a few - gram(s) for the average polymetallic nodule.

It can be concluded, according to the experimental trials with polymetallic nodules from the Clarion-Clipperton Zone and by means of a one-way coupled CFD-DEM model, that the contribution of abrasive wear results into a (maximum) remaining mass of 97%. However, it is advised to extend the computer model with a two-way (or multi-way) coupling between the liquid and the solids. It is also recommended to conduct vertical abrasive wear tests with nodules, in order to validate the model and gain more insight in degradation behaviour.

Samenvatting

Mangaan knollen lagen al eeuwen op de diepzee bodem voordat deze menselijke bekendheid kregen. De eersten die de nodules ontdekten waren Murray en Renard, tijdens hun wetenschappelijk cruise tussen 1872 en 1876 (Murray and Renard, 1876). Met name de Clarion-Clipperton Zone, gelegen tussen Mexico en Hawaii, blijkt over een nagenoeg onuitputtelijke hoeveelheid minerale bronnen te beschikken. De mangaan knollen bestaan voor het overgrote deel uit mangaan, maar doordat er ook metalen als koper en cobalt inzitten, worden de knollen steeds interessanter voor onze moderne samenleving. Een andere benaming voor de mangaan knol is polymetallische nodule, vanwege de content aan vele andere metalen.

Door middel van een verticaal hydraulisch transport systeem zullen de mangaan knollen vanaf de zeebodem naar boven getransporteerd worden. Gezien het feit dat de nodules zich bevinden op een diepte van ongeveer 5000 meter, is het aannemelijk dat deze in aanraking komen met de buiswand gedurende het transport. Wanneer een knol in aanraking komt met de muur, kan er abrasieve slijtage plaatsvinden. Abrasieve slijtage, ofwel glijdende slijtage, zorgt ervoor dat de knol degradeert, ofwel in massa afneemt, door het glijdende contact met de buiswand.

De hoofdvraag van deze Master Thesis is als volgt:

Wat is de bijdrage van abrasieve slijtage ten opzichte van degradatie van mangaan knollen, in een verticaal hydraulisch transport systeem?

De bijdrage van abrasieve slijtage is getoetst aan de hand van de vergelijking van Archard (1953). In het MTI laboratorium te Kinderdijk zijn verschillende mangaan knollen getest in een speciaal gemaakte experimentele opstelling. De mangaan knollen beschikbaar voor deze Master Thesis komen uit de Clarion-Clipperton Zone (CCZ). In de eerste serie experimenten lag de focus op enkele knol degradatie. De knollen zijn gewogen voor en na een testrun, hierna wordt de nodule massa na een testrun gedeeld door de initiële massa, resulterend in de genormaliseerde overblijvende massa. Elke testrun bestaat uit een specifieke glijlengte. Met de glijdende lengte en genormaliseerde overblijvende massa, kan een voorspelling worden gedaan van de materiaal specifieke slijtagefactor, genoteerd als k [m^2/N]. Uit de experimenten is een waarde van $k = 4.16 \cdot 10^{-9}$ [m^2/N] gekomen. Met deze k-waarde blijft er na 1000 meter glijdend contact, in het ergste geval, nog 97% procent van de originele nodule massa over.

Vervolgens zijn er nog proeven uitgevoerd met batches van knollen, waarbij de verwachting is dat de bijdrage van abrasieve slijtage toeneemt aan de totale nodule degradatie, door de aanwezigheid van korrel-korrel interactie. Recentelijk zijn er door Blue Mining proeven uitgevoerd in Freiberg, Duitsland, in een verlaten mijnschacht. Hierin is een verticale buis geplaatst van bijna 130 meter, en is het effect van abrasie op een partij knollen gezien. Gedurende de batch experimenten in Kinderdijk, waarbij de batch van knollen zich in een horizontale positie bevindt, bleek de bijdrage van abrasie groter dan gedurende de Freiberg experimenten.

Gebruikmakend van het open-source programma OpenFOAM, is een verticale turbulente buisstroming gemodelleerd. De buis heeft vergelijkbare dimensies met de buis van de experimentele opstelling. De simulatie is gedaan met behulp van een Large Eddy Simulatie (LES). Door middel van een een-weg koppeling is de data van het stromingsveld gekoppeld aan de bewegingen van de gesimuleerde deeltjes. Vervolgens werden op verschillende plekken aan de ingang van de buis puntdeeltjes los gelaten. De eerste serie puntdeeltjes hebben een diameter ter grootte van eenderde van de buisdiameter, overeenkomende met de veelvoorkomende grootte van een mangaan knol. De botsingen tussen het puntdeeltje en de buiswand worden met een Discrete Element Methode (DEM) opgelost, bestaande uit een (niet-lineair) veer-demper systeem.

Om de gevoeligheid van het model te toetsen, worden er ook puntdeeltjes ter grootte van eenzesde en eentiende deel van de buisdiameter losgelaten in de buis. Het aantal botsingen per totaal aantal simulaties zal vergeleken worden met elkaar. Uiteindelijk bleek dat in 15% van de simulaties er sprake was van kortstondig contant met de buiswand, ongeacht de diameter van het deeltje. Wanneer deze 15% wordt afgezet tegen de experimenten met de enkele knollen, is er sprake van een gewichtsverlies van maximaal 0.5%, wat een gewichtsverlies van slechts een enkele gram voor de gemiddelde mangaan knol zou betekenen.

Geconcludeerd kan worden, aan de hand van de experimentele proeven met mangaan knollen uit de Clarion-Clipperton Zone en door middel van een-weg gekoppeld CFD-DEM model, dat de bijdrage van abrasieve slijtage resulteert in een (maximale) behoudendheid van de originele knol massa van 97%. Er wordt echter wel geadviseerd om het computermodel uit te breiden met twee-weg (of meerweg) koppeling tussen de vloeistof en de vaste stoffen. Tevens wordt er ook aangeraden om extra verticale slijtage proeven te doen met knollen, om zo het slijtage gedrag nog beter te omvatten.

Preface

Dear reader,

Before you lays the Master Thesis of Jasper Wijnands, from the Technical University of Delft. This Master Thesis would not be possible without the Technical University of Delft and IHC MTI (Royal IHC). The main topic of this work is the contribution of sliding wear on the degradation of polymetallic nodules during vertical transportation, from the deep sea floor to the sea surface.

First, I would like to express my gratitude towards Cees van Rhee and Arno Talmon, from the Technical University of Delft. Both for their professional point of view on dredging related problems, and for reading and commenting on my Master Thesis. A thanks is given towards my classmates, interesting discussions about the subject of my Master Thesis resulted very often into new insights. Wim-Paul Breugem from the Process and Energy department of the TU Delft, is thanked for his independent view on this work.

The first one I would like to thank from IHC MTI, is my daily supervisor Edwin de Hoog. I would like to thank him for his advice, broad theoretical knowledge and unbelievable enthusiasm. It was a pleasure and at the same time an adventure, to figure out the mystics of polymetallic nodules together, since there is yet so little known. Also, thanks are given to Joep Goeree and Jort van Wijk. It is an absolute privilege to gain advice from these inspiring persons. Special thanks are given to Maarten in 't Veld, not only because of his critical, but always technical point of view, but also because of the joyful car trips between Dordrecht and Kinderdijk. The sieving lessons from Boris Dzon in the soil laboratory were an unforgettable experience. Last, but not least, many thanks are given to Jazzie Hoebe and Yarno Ketting. With their practical experience and insights, the experimental setup became a success.

Most of all I would like to thank my parents, brother and sister, who were always willing to listing and were always there to support me during the graduation period. I would like to give special gratitude to our lovely dog Luca, who was always in favor for a walk if the work on this Master Thesis became too difficult to continue (for a moment).

Furthermore, I would like to thank my friends. After almost a year I can imagine that they are happy that the stories about polymetallic nodules have come to an end. But without their support and tips, how small they sometimes seemed to be, this had never a been success.

Personally, I enjoyed (almost) every moment of the past year. It has been an incredible journey and it resulted into something I will be very proud of, at least the coming years.

Enjoy reading!

J.T.M. Wijnands
Vogelenzang, December 19, 2018

Contents

Nomenclature

Roman Symbols

Symbol	Description	Unit
A_p	Particle Surface	[m^2]
c_{dmp}	Damper Constant of the DEM Model	[kg/s]
C_D	Coefficient of Drag	[-]
D_{mp}	Pipe Diameter of the Model	[m]
$d_{p,DEM}$	Outer Particle Diameter of the DEM Model	[m]
d_p	Particle Diameter	[m]
e	Void Ratio	[-]
F_B	Force due to Buoyancy	[N]
F_D	Drag Force	[N]
F_G	Force due to Gravity	[N]
F_N	Normal Force	[N]
F_w	Wall Friction Force	[N]
g	Gravitational Acceleration	[m/s^2]
H_{mp}	Pipe Height of the Model	[m]
k	Specific Wear Rate	[m^2/N]
k_{spr}	Spring Constant of the DEM Model	[N m^2]
m_1	Mass of a Polymetallic Nodule before a Test Run in the Abrasive Wear Tester	[kg]
m_2	Mass of a Polymetallic Nodule after a Test Run in the Abrasive Wear Tester	[kg]
$m_{a,p}$	Particle Added Mass	[kg]
m_d	Dry Mass of a Polymetallic Nodule	[kg]
m_n	Normalized Remaining Mass	[-]
m_p	Particle Mass	[kg]
m_w	Wet Mass of a Polymetallic Nodule	[kg]
n	Porosity	[%]
R_p	Pipe Radius	[m]
r_p	Particle Radius	[m]
s	Sliding Distance	[m]

v_{avg}	Average Velocity of a Nodule in the Abrasive Wear Tester	[m/s]
V_p	Particle Volume	[m^3]
V_w	Worn Volume	[m^3]
w	Water Content	[%]
w_f	Vertical Fluid Velocity	[m/s]

Greek Symbols

Symbol	Description	Unit
Δt	Time Step of the Model	[s]
μ_w	Wall Friction Coefficient	[-]
ν_f	Kinematic Fluid Viscosity	[m^2/s]
ρ_d	Dry Density	[kg/m^3]
ρ_f	Fluid Density	[kg/m^3]
ρ_{part}	Particle Density	[kg/m^3]
ρ_{situ}	Situ Density	[kg/m^3]
ρ_s	Solids Density	[kg/m^3]
θ	Angle of Inclination of the Abrasive Wear Tester	[°]

Abbreviations

Symbol	Description
AWT	Abrasive Wear Tester
BTS	Brazilian Tensile Strength
CCZ	Clarion-Clipperton Zone
CFD	Computational Fluid Dynamics
DEM	Discrete Element Method
EEZ	Exclusive Economic Zone
IONF	Indian Ocean Nodule Field
ISA	International Seabed Authority
LES	Large-Eddy Simulation
OD	Old Dendritic zone
OL	Old Laminated zone
PSD	Particle Size Distribution
REE	Rare Earth Elements
UCS	Unconfined Compressive Strength
VTS	Vertical Transport System
YD	Young Dendritic zone
YL	Young Laminated zone

List of Figures

List of Tables

1 Introduction

A study related to deep sea mining always brings new insights. Whether it concerns the vertical transportation technique for deep sea mining, the degradation of deep sea deposits during the transportation to the sea surface, or the discovery of new species on the deep sea floor, like Casper the octopus, which can be seen in Figure 1.1. The focus of this work is related to the second example, polymetallic nodule degradation during vertical transportation.

Figure 1.1: Casper the octopus, a new species of octopus and named after the cartoon figure, discovered 4000 meters below the sea surface in 2016 by scientists (www.pewtrusts.org)

This chapter starts with background information in section 1.1, giving some history and information about the main reason for this topic. The problem description is defined in section 1.2. The objective, main - and secondary research questions are given in section 1.3. This chapter ends with section 1.4, where the outline of this master thesis is provided.

1.1. Background - Global Demand for Mineral Resources

During the past decade the interest in mineral resources has grown exponentially. Responsible for this growth is for example the worldwide demand for portable electronic devices and electrical vehicles. Both contain lithium-ion batteries, with cobalt as one of its elements. The unique properties of cobalt makes it particularly suitable for several goods (Shedd et al., 2017), for example superalloys and magnets, but the biggest part is related to the fabrication of batteries. The global demand for cobalt is plotted against the past years in Figure 1.2.

In an era of depletion of terrestrial mines, the need to discover mines containing mineral resources, is urgent. However, one the first discoveries of mineral resources on the seabed is done more than a hundred years ago, by the scientific cruise of the H.M.S. Challenger (1872-1876). This discovery has been done in the Clarion Clipperton Zone, located between Mexico and Hawaii, in the north central Pacific. The total zone spans 4.5 million square kilometers[1]. A wide variety of polymetallic nodules is encountered in this zone, with an average nodule abundance of 15 kg/m^2 (Baker and Beaudoin, 2013). Polymetallic nodules from the Clarion Clipperton Zone, consist mainly of manganese and are therefore often referred to as manganese nodules.

The Clarion Clipperton Zone distinguishes itself by containing the largest amount of polymetallic nodules and is therefore interesting for mining purposes. The nodules have been, literarily, laying on the seafloor for millions of years. In order to mine these nodules from the seafloor, at some places more than five thousand meters below the sea surface, a complex vertical hydraulic transport system is required. A subsea mining crawler will collect the nodules from the seabed and will pump them inside a vertical hydraulic transport system. From an economical perspective, a sufficient production rate must be achieved. It is likely that nodule damage and nodule degradation will occur during vertical transportation of the polymetallic nodules over these lengths.

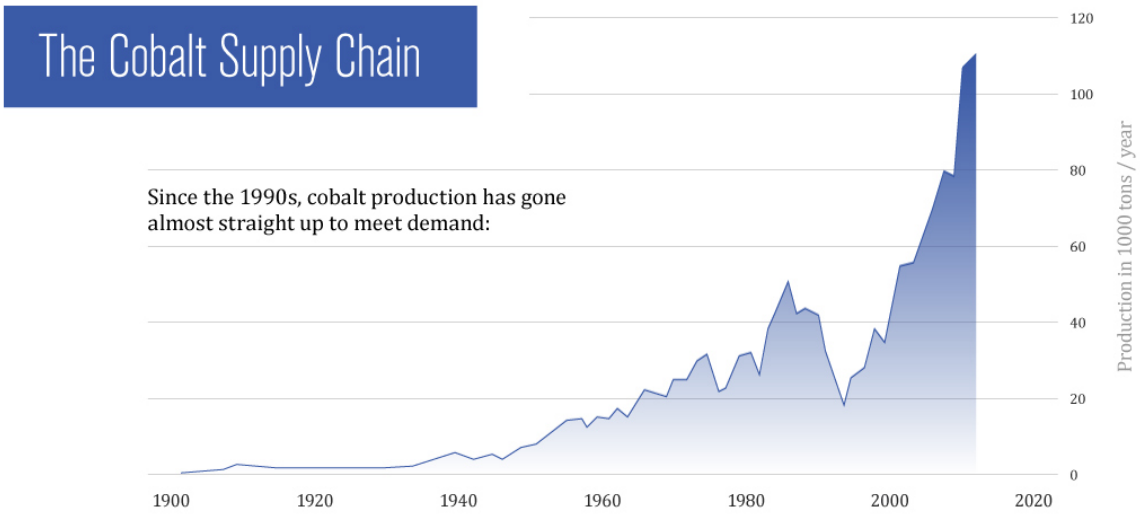

Figure 1.2: Global demand for cobalt plotted against the past years (www.visaulcapitalist.com)

1.2. Problem Description

After the nodules are collected by a subsea mining crawler, the nodules are mixed into a slurry and vertically transported to the processing vessel. An extensive research on a vertical hydraulic transport system has been done for IHC MTI by Van Wijk (2016). In the Master Thesis of De Hoog (2016) the coarse slurry flow in inclined pipes and vertical S-bends is described. Both studies involved the techniques related to coarse particle transport, but did not investigate the effect of particle degradation during transport.

During vertical transportation of the nodules, nodule degradation will happen as a result of: impact with one -or more- impeller blade(s) in one of the centrifugal pumps, particle-particle interaction in the vertical pipe and/or the sliding of nodules along the pipe wall. The aspect of impact wear, the nodule degradation

[1] www.pewtrusts.org

mechanism inside a centrifugal pump, is researched by Zenhorst (2016). Another prediction of nodule degradation during vertical hydraulic transport is given in Van Wijk (2017). In Van Wijk (2017) it is expected that polymetallic nodule degradation will be mainly caused by impact fracturing due to the centrifugal pumps. Thus, the effect of sliding wear on nodule degradation is in both studies, Zenhorst (2016) and Van Wijk (2017), not taken into account. Therefore, to complete the research on degradation of nodules during vertical transportation, the contribution of sliding wear to the total degradation of the mineral resources, is searched for.

1.3. Research Questions and Objective

In the previous section it is stated that the contribution of sliding wear to the total degradation of polymetallic nodules is required to know. Therefore, the main research question is defined as follows:

What is the contribution of abrasive wear to the degradation of polymetallic nodules, in a vertical transport system?

The secondary research questions, which are sorted per chapter, are formed as follows:

- Analysis - Polymetallic Nodules from the Clarion-Clipperton Zone (chapter 2):
  - *What causes the renewed interest of deep sea mining of polymetallic nodules?*
  - *How come that the Clarion-Clipperton Zone is so suitable for deep sea mining purposes?*
- Theory - Degradation of Brittle Agglomerates (chapter 3):
  - *Which types of wear mechanisms could be encountered during slurry transport?*
  - *How can particle degradation be quantified?*
  - *What is the effect of wear mechanisms on brittle agglomerates?*
- Scale Model Experiments I - Degradation of a Polymetallic Nodule (chapter 4):
  - *Is the equation of Archard applicable for polymetallic nodule degradation due to abrasive wear?*
  - *Does the sliding velocity influence the degradation due to abrasive wear?*
- Scale Model Experiments II - Degradation of a Batch of Polymetallic Nodules (chapter 5):
  - *Is the equation of Archard applicable to quantify the degradation due to abrasion for a batch of nodules?*
  - *Until what extent does polymetallic nodule degradation propagate?*
- Modelling - Single Particle in a Vertical Turbulent Pipe Flow (chapter 6):
  - *What is the ratio between the sliding length of the particle against the pipe wall and the total traveling length of the particle?*
  - *Does the ratio of particle diameter over pipe diameter influence the sliding length per meter pipe?*

The first sub-objective is to gain theoretical knowledge about the polymetallic nodules and their origin. Subsequent, research is conducted on the different degradation processes during (coarse) particle slurry transport. Using this theory, scale model experiments are performed. Both experimental results as observations during the experiments will help to form an answer to the secondary research questions. The last sub-objective is to construct a model of a pipe flow in which particles are released in order to get an insight in the sliding length during transportation.

The main objective of this Master Thesis is to combine both experimental, as modelling results and the answers to the secondary research questions, in order to provide an answer to the main research question.

1.4. Outline of this Master Thesis

General analysis of the polymetallic nodules is provided in chapter 2. It gives an insight in the physical properties of the nodules and the reasoning for mining purposes. The origination and growing processes are also described in this chapter.

An overview of state of the art research on (coarse) particle degradation is summarized in chapter 3. Particle degradation as an effect of different wear mechanisms is described, with abrasive wear more in detail.

In chapter 4 a scale model experiment is described, whereas the effect of abrasive wear on nodule degradation is tested. The equation of Archard (1953) is applied on the experimental results and gives a good insight in the linear degradation behaviour due to abrasive wear. Details of the experiments, summarized in tables, can ben found in Appendix A. In Appendix C additional information of the experimental setup can be found.

A second set of experiments is described in chapter 5. These experiments are focussed on the effect of abrasive wear on a batch of nodules. The test results are compared to the results from experiments in an abandoned mining facility, in which a vertical pipe was mounted with a length of almost 130 meters, performed by IHC MTI.

A one-way coupled CFD-DEM model is made, which is described in chapter 6. OpenFOAM is used to construct a turbulent flow profile through a pipe. The dimensions of the pipe are comparable to the pipe used in the experimental setup. With a one-way coupling a particle is released into the flow, using MATLAB, whereas the obtainment of collision forces is done by means of a Discrete Element Method (DEM). The one-way coupling is a simplified approach, it states that the flow only exerts forces on the particle, and not the other way around. The mesh details, the C++ script to construct the mesh using Gmsh and figures from the simulations, related to chapter 6, can be found in Appendix B. The latter also provides algorithms which are used in during the simulations.

The last chapter, chapter 7, gives conclusions about this work and recommendations for future research.

2

Analysis - Polymetallic Nodules from the Clarion-Clipperton Zone

Years have passed by since the first expedition of the H.M.S. Challenger (1872-1876) and the discovery of polymetallic nodules. Their report (*Report Of The Scientific Results of the Exploring Voyage of H.M.S. Challenger during the years 1872-1876*), contains information about the discoveries they did on the seafloor (Murray and Renard, 1876). Polymetallic nodules can be described as: 'potatoes, mammillated cannon balls, marbles, tablets and a number of less recognizable forms' (Mero, 1965). They contain several metals, with a majority of manganese, and therefore polymetallic nodules are often referred to as manganese nodules. Mero (1965) suggested mining of these deep sea deposits, due to its large supplies and its characteristics. Although he stated this more than 50 years ago, the interest for deep sea mining of polymetallic nodules rises again. The nodules available for this research originate from the Clarion-Clipperton Zone (CCZ), located between Mexico and Hawaii and therefore these nodules and region are more explained in detail.

Gradually it will become clear what manganese nodules are and how they could potentially contribute to our modern industry. Two secondary research questions are formed in order to provide an answer to the growing interest in the deep sea mining industry, but also to provide background information of the main topic of this Master Thesis.

Secondary research questions of this chapter:

- *What causes the renewed interest of deep sea mining of polymetallic nodules?*
- *How come that the Clarion-Clipperton Zone is so suitable for deep sea mining purposes?*

An overview of the regions around the world where polymetallic nodules can be found is given in section 2.1. Four zones with high nodule abundance are distinguished and shortly described. In section 2.2 the growing process of polymetallic nodules is described. This section also includes a sieving analyses of the complete batch of nodules, available for this Master Thesis. In section 2.3, both material, as physical properties of the nodules are given. From the physical properties, only the density of the manganese nodules is measured, the rest of the physical properties originates from literature. So, after describing the (possible) mining locations around the world, the different growing processes, and properties of polymetallic nodules, will section 2.4 be focussed on deep sea mining in the CCZ. The concept of deep sea mining by means of a vertical hydraulic transport system (VTS) is given in this section. This chapter encloses with conclusions and recommendations in section 2.5. It provides an answer to the formed secondary research questions and gives recommendations about working with polymetallic nodules.

2.1. Introduction - Global Spread of Polymetallic Nodules

Since the scientific cruise of Murray and Renard (1876) it is known that polymetallic nodules are spreaded in several areas across the ocean floor. In Figure 2.1 four promising zones for mining purposes, because of their nodule abundance, are shown. Each of the zones are shortly described in the following. Because the nodules available for this research originate from the Clarion-Clipperton Zone, a more detailed description about the nodules is given in section 2.3.

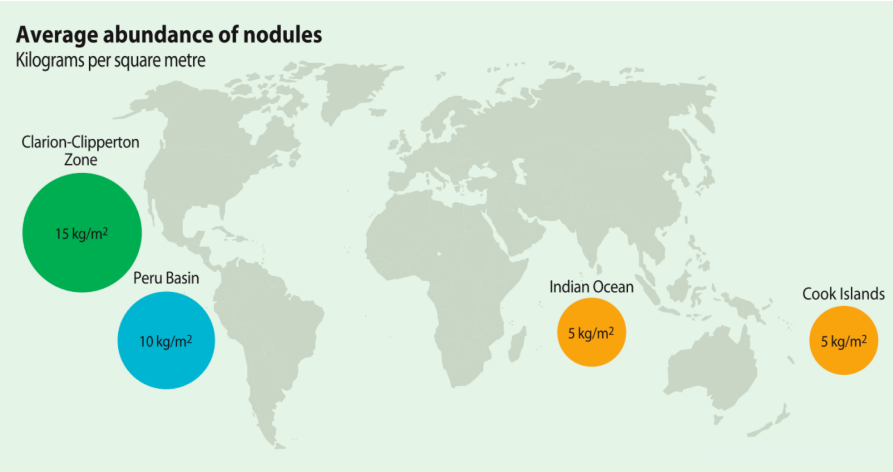

Figure 2.1: Locations of polymetallic nodules around the world (Baker and Beaudoin, 2013)

Clarion-Clipperton Zone

The Clarion-Clipperton Zone (CCZ) is located in the tropical north pacific, between Mexico and Hawaii. The seafloor stretches between the 4000 and 6000 meters below the sea surface (Nimmo, 2013). The typical size of the polymetallic nodules from the CCZ ranges between 10 and 100 mm (Mero, 1965; Skornyakova and Murdmaa, 1992; Van Wijk, 2016). The nodule abundance in this zone is around 15 kg/m^2 (Baker and Beaudoin, 2013; Skornyakova and Murdmaa, 1992) and is therefore the most abundant region around the world. The total content of Rare Earth Elements (REE) of all the nodules in the CCZ, is comparable to the content of the largest REE terrestrial mine, the Bayan Obo mine in China (Hein, 2012). However, it is not the content of REE that makes them interesting for mining industry, but the content of nickel, copper and especially cobalt, makes them valuable.

Cook Islands

The Cook Island Exclusive Economic Zone (EEZ) is located in the south Pacific and covers an area of almost 2 million square kilometers (Hein et al., 2015). The zone has an average depth of about 5000 m (Baker and Beaudoin, 2013). The polymetallic nodule size ranges between the 8 and 50 mm (Cronan, 1990), which makes them relatively small compared to the nodules from the other zones. A small region in the EEZ (close to French Polynesia) has an astonishing nodule abundance of 58 kg/m^2 (Hein et al., 2015), but the average nodule abundance over the entire zone is 5 kg/m^2 (Baker and Beaudoin, 2013). The nodules contain elements like cobalt, nickel and even titanium (Hein et al., 2015).

Indian Ocean Nodule Field

The Indian Ocean Nodule Field (IONF) is located south of India, with depths ranging from 4000 to 5500 m. Most of the nodules are between the 20 and 60 mm, but there are examples of nodule sizes greater than 80 mm (Mukhopadhyay et al., 2018). The average nodule abundance in this region is around 5 kg/m^2 (Baker and Beaudoin, 2013; Mukhopadhyay et al., 2018). The nodules in this area are characterized by their high iron content and therefore often referred to as ferromanganese deposits (Calvert and Cronan, 1978).

Peru Basin

The Peru Basin is located in the eastern equatorial Pacific, with water depths varying between 4000 and 4250 m (Von Stackelberg, 1997). Most of the nodules have sizes of about 40 to 80 mm, but some of the greatest

nodules are even 210 mm. Nodules in this zone are on average quite large, since nodules smaller than 15 mm are rather scarce (Mukhopadhyay et al., 2018; Von Stackelberg, 1997). Remarkable to these nodules is that they are predominately grown diagenetically, since most of them are buried; more information about the diagenetic growing process can be found in section 2.2. The Peru Basin has an average nodule abundance of 10 kg/m^2 (Baker and Beaudoin, 2013), however, there are regions in this zone with abundances of 50 kg/m^2 (Von Stackelberg, 1997).

2.2. Growing Process of Polymetallic Nodules

In the previous section it is shown that the nodules are located in different zones around the world, whereby each zone has its own characteristics. Although each zone differs from the other, they have a common property, it is a real challenge to reach the nodules on the seafloor. In these areas at the seafloor there is no sunlight and the ambient pressure rises up to 500 bars.

Nevertheless, the areas are an ideal environment for the growing of polymetallic nodules, regarding the fact that the nodule abundance in the CCZ is around 15 kg/m^2 (Baker and Beaudoin, 2013; Skornyakova and Murdmaa, 1992). Before the growing process of the nodules is explained in detail, first an example is shown how the nodules lay on the seafloor, in Figure 2.2 and Figure 2.3.

Figure 2.2: Example of the polymetallic nodules on the seafloor in the CCZ (Mero, 1965)

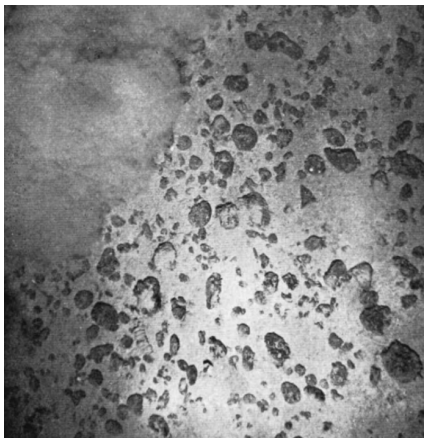

Figure 2.3: Another example of the polymetallic nodules on the seafloor in the CCZ (Mero, 1965)

Figure 2.2 and Figure 2.3 give an idea of the nodule abundance in the CCZ. In section 2.1 the different nodule sizes have been discussed. The growth rate of polymetallic nodules is related to the formation environment (Baker and Beaudoin, 2013). In Figure 2.4, the formation process of manganese nodules is schematically represented.

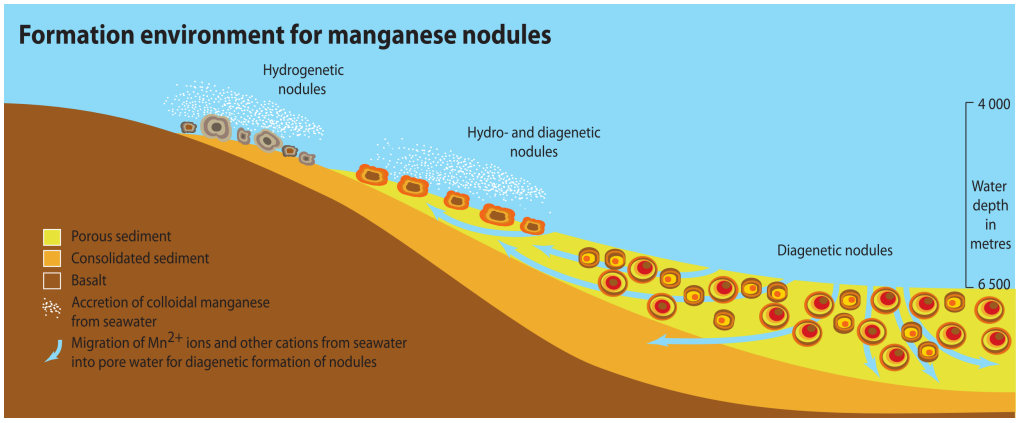

Figure 2.4: Formation process of polymetallic nodules, a process which takes place at depths between 4000 and 6500 meters below the sea surface (Baker and Beaudoin, 2013)

From Figure 2.4 it can be seen that the water depth causes different formed nodules; hydrogenetic nodules, hydrogenetic and diagenetic nodules, and diagenetic nodules. Thus, the formation process of manganese nodules can be separated into two different processes (Baker and Beaudoin, 2013):

1. Hydrogenetically:
   Minerals precipitate from cold ambient seawater
2. Diagenetically:
   Minerals precipitate from sediment pore waters, in other words, seawater that has been modified by chemical reactions within the sediment

The result of a combination of both of the growing processes can be seen in Figure 2.5.

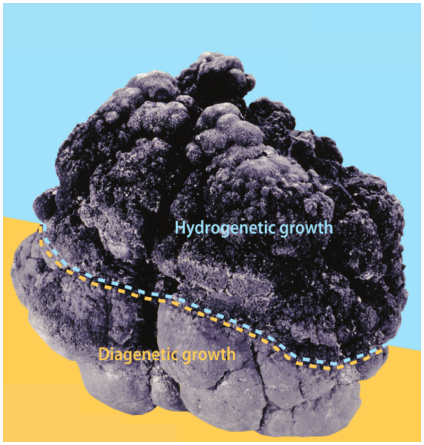

Figure 2.5: Hydrogenetically and diagenetically growth of a nodule (www.bgr.bund.de)

Baturin (1987) did research on the growth rate of polymetallic nodules and estimated it to be several millimeters per million years. Research by Baker and Beaudoin (2013) showed that the growing process depends on the type of nodule. Marchig and Halbach (1982) concluded that the hydrogenetically formed nodules have a smaller growth rate than the diagenetic formed nodules. This is in accordance with the fundings of Baker and Beaudoin (2013), hydrogenetic nodules grow with a rate of 1-10 millimeters per million years, whereas the diagenetic nodules grow with a rate of growth up to hundreds of millimeters per million years. The combination of the growing processes, results into the growth rates as shown in Figure 2.6 and Figure 2.7.

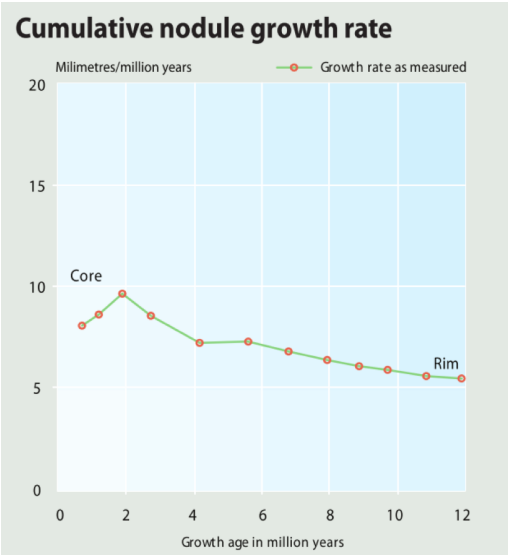

Figure 2.6: Growth age plotted against cumulative grow rate (Baker and Beaudoin, 2013)

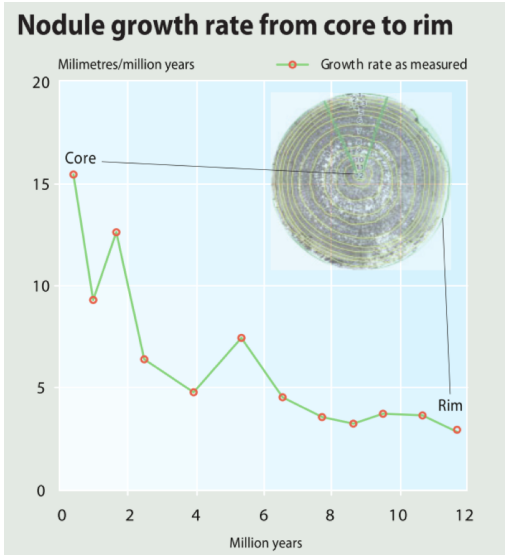

Figure 2.7: Growth rate plotted against nodule age (Baker and Beaudoin, 2013)

Both of the types of nodules occur in the CCZ, the average nodule abundance of diagenetic nodules varies between 1-10 kg/m^2 (Skornyakova and Murdmaa, 1992); whereas the hydrogenetic nodules occur at a higher abundance of more than 10 kg/m^2 (Zenhorst, 2016).

The difference in hydrogenetic and diagenetic formed nodules can also be seen by their difference in surface. Baturin (1987) stated that the faster growing nodules (diagenetic nodules), consists of a rough surface. According to their study it is concluded that the nodules from the CCZ have a ring-like midsection, some sort of equatorial belt. This would indicate a nodule growth at the seafloor-water interface. When the nodules are partly submerged in the ground, like the nodules from Figure 2.2, they would grow diagenetic below the interface and hydrogenetic above the seafloor. The result that follows is a rough lower surface and a smooth upper surface, which can also be seen in Figure 2.5.

Like Baturin (1987), also Marchig and Halbach (1982) did research on the growing processes. But instead of looking at the surface of a nodule, they looked into the inside of polymetallic nodules. They called the different zones inside a nodule 'laminated' and 'dendritic'. Examples of nodules that were examined are shown by Figure 2.8 until Figure 2.11. Marchig and Halbach (1982) contemplates old and young layers, resulting into four different zones inside a nodule:

- Old Laminated zone (OL):
  First zone of growth, consists of laminated material in the centre of the nodule

- Old Dendritic zone (OD):
  Second zone of growth, a zone of changing thickness, in some nodules only partly present, in others completely overgrowing the OL zone

- Young Laminated zone (YL):
  Third zone of growth, showing an almost constant thickness around the nodule

- Young Dendritic zone (YD):
  The fourth zone of growth, the youngest zone of the nodule and appears mostly on the equatorial section of the nodule, fed by sediments

The most important zone of a nodule is almost forgotten in the listing above, without this zone the polymetallic nodules could not even exist. The rock fragment where the nodule is accumulated around, called SF by Marchig and Halbach (1982). This zone however does not need to be necessary a rock fragment, a shark teeth or cetacean ear bones, could also act as the nuclei of a nodule (Mero, 1965). This is because of relatively large crystallites inside, wherefore they are protected against disintegration forces acting on the deep sea floor. Therefore nodules can grow around these objects. Also carbonates, phosphates, zeolites, clays, or various forms of silica can be the nuclei of a polymetallic nodule (Mero, 1965). With all this knowledge, that shark-teeth nodule slightly right from the middle in Figure 2.3, becomes very noticeable all of a sudden.

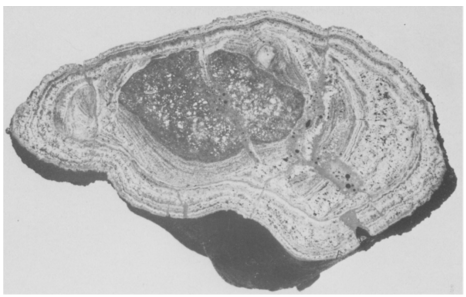

Figure 2.8: Cross section of a nodule with a single core (Marchig and Halbach, 1982)

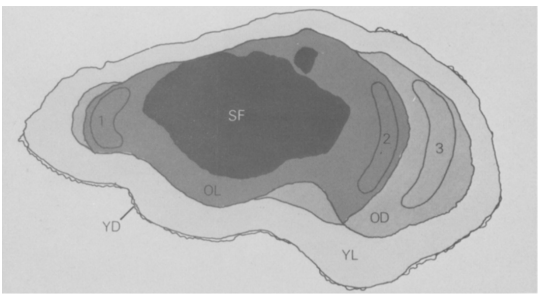

Figure 2.9: Schematic representation of the different layers in a nodule with a single core (Marchig and Halbach, 1982)

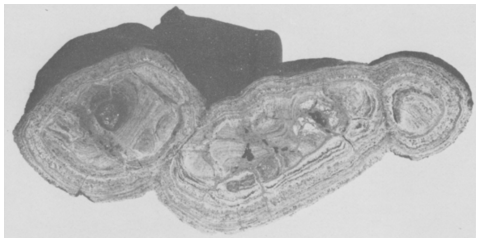

Figure 2.10: Cross section of a nodule with two cores (Marchig and Halbach, 1982)

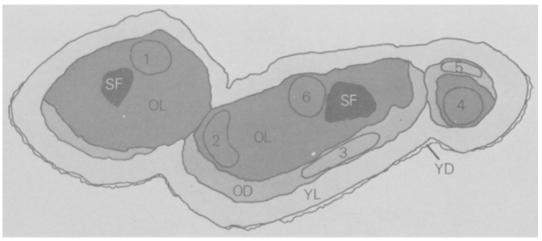

Figure 2.11: Schematic representation of the different layers in a nodule with two cores (Marchig and Halbach, 1982)

The different sizes are thus caused by the different environments and the number of cores inside the nodules. And the different depths causes different growing rates. However, to form a nodule of the size like the one shown by Figure 2.12, it will take millions of years.

2.2.1. Sieving Analysis - Variety of Polymetallic Nodules

Polymetallic nodules can be described as: “potatoes, mammillated cannon balls, marbles, tablets and a number of less recognizable forms” Mero (1965). In Figure 2.12 an example of a real nodule can be seen. The dimensions of this nodule are 10 x 8 x 6 centimeters (length x width x height) and weighs 376.92 grams. This picture was taken before test number 6 (more details on the experiments are given in chapter 4).

Figure 2.12: Example of a polymetallic nodule from the CCZ

The different growing processes results into different nodule sizes. The typical size of the manganese nodules from the CCZ ranges between the 10 and 100 mm in diameter (e.g. Mero (1965); Skornyakova and Murdmaa (1992); Van Wijk (2016)).

In the dredging industry, particles are classified by their size. This classification of soils, according to the American norm ASTM Standard D288[1], is represented in Table 2.1. From this table it can be concluded that manganese nodules from the CCZ, can be classified as cobbles and (medium/coarse) gravel.

[1] TU Delft OpenCoarseWare: Offshore Engineering - Dredge Pumps and Slurry Transport (Chapter 2)

Table 2.1: Identification and classification of soil for dredging purposes

Main type of soil		Particle size	
		Identification	Size [mm]
Boulders	Granular Non-cohesive	-	> 200
Cobbles		-	200 - 60
Gravel		Coarse	60 - 20
		Medium	20 - 6
		Fine	6 - 2
Sand		Coarse	2 - 0.6
		Medium	0.6 - 0.2
		Fine	0.2 - 0.06
Silt	Cohesive	Coarse	0.06 - 0.02
		Medium	0.02 - 0.006
		Fine	0.006 - 0.002
Clay		-	< 0.002

To represent a collection of different sizes, a Particle Size Distribution (PSD) can be made. In a PSD the particle diameter is plotted against the cumulative weight percentage. A sieving analysis is done, on the sample of manganese nodules, to make a PSD curve. When the nodule does not fit through the sieve - regardless of its configuration - it will assigned to this size class. After the sieving is done, all the classes are weighted. Next, the cumulative percentage can be determined for each class and this can be plotted into a figure, to make a PSD curve. The sample of nodules and sieving of the nodules used for this thesis, can be seen in Figure 2.13 and Figure 2.14. In Figure 2.15 the PSD of the complete batch of nodules can be seen.

From an experimental point of view, PSD's are an advantage to represent a batch of material. Regardless of the total weight, it states enough information to reconstruct the curve. Once the mass-median diameter (d_{50}) and at least one other cumulative diameter are known (preferably two diameters), for instance the d_{15} or d_{85}, a PSD could be made. These diameters represent the total mass fraction that is finer than that specific fraction of the total soil sample. For example: the d_{85} denotes the diameter for which 85% of the particles in the sample are finer (by mass)[1]. The d_{50} of the batch of nodules available for this Master Thesis, is equal to almost 67 mm, as can be seen in Figure 2.15.

Figure 2.13: Sample of manganese nodules from the CCZ, available for this Master Thesis

Figure 2.14: Sieving of the manganese nodules at the MTI laboratory in Kinderdijk

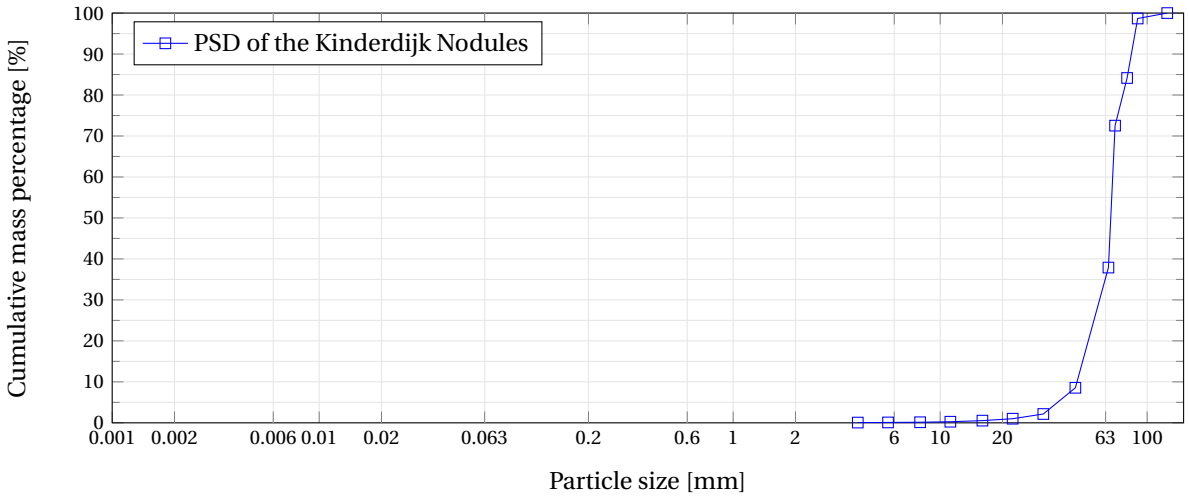

Figure 2.15: PSD curve of the available batch, showed in Figure 2.13, of polymetallic nodules from the CCZ

2.3. Characteristics of Polymetallic Nodules

The shortest answer to the first secondary research question of this chapter would be: "Because of the elements inside a polymetallic nodule". And after reading the background information in section 1.1 it is known that one of the elements inside a polymetallic nodule should be cobalt. And, as the name states, polymetallic nodules will contain many metals. In section 1.1 it is also mentioned that another name for polymetallic nodules is manganese nodules, due to their largest content, manganese. However, these are only two elements of a long list of elements, which is explained in subsection 2.3.1.

In the followup section, subsection 2.3.2, the hardness and strength of polymetallic nodules is discussed. Hereafter, other physical properties are explained in subsection 2.3.3, namely the density and porosity. Due to the fact that several authors came with different measures for the density of polymetallic nodules, for example Mero (1965), Halbach et al. (1975) or Dreiseitl (2017), it is chosen to measure the density of the available nodules for this research. As stated before, the batch of nodules for this Master Thesis, as shown in Figure 2.13, originates from the CCZ and therefore the density measurement results are compared to nodules from the CCZ.

2.3.1. Metal Content of Polymetallic Nodules

(Marchig and Halbach, 1982; Mero, 1965; Usui, 1983; Wegorzewski and Kuhn, 2014) have conducted experiments on the quantification of the metals inside the polymetallic nodules. It can be concluded that the primary elements inside a polymetallic nodule are manganese and iron. However, it is not the manganese or iron what makes the nodules attractive for our modern industry, it is the interest in cobalt, copper and nickel. Especially the rising cobalt demand, as shown in Figure 1.2, makes the manganese nodules interesting for mining purposes.

The nodules from the CCZ are characterized by their relatively high content of cobalt, copper, nickel, and manganese (Skornyakova and Murdmaa, 1992). Research by Mero (1965) has let to a list of all the metals inside nodules from the CCZ. In Table A.1 the elements and their weight percentages are given. Also, the most common metals characterizing nodules from the CCZ are pointed out in bold.

A less known element in polymetallic nodules, but certainly not less useful nowadays, is Molybdenum. Molybdenum has a very high melting temperature (2900 Kelvin) and is often used in superalloys.

2.3.2. Hardness and Strength of Polymetallic Nodules

The hardness of a particle can be expressed in the scale of Moh. The hardness of manganese nodules is around 3-4 on the scale of Moh (Glasby, 1977). The hardness of manganese nodules can vary between 1-4 on this scale according to Mero (1965). The hardness of a material can be seen as an indicator for the degradation process of that material (Van den Berg and Alvarez Grima, 2006). They concluded that relative soft materials, like limestone with a Moh's hardness around 3, show a great resistance against impact wear, but are more sensitive to abrasive wear. The (non-linear) scale of Moh is represented in Table 2.2 (Miedema, 2015b).

Table 2.2: The hardness [Moh] of different minerals

Hardness [Moh]	Mineral
1	Talc
2	Gypsum
3	Calcite
4	Fluorite
5	Apatite
6	Orthoclase
7	Quartz
8	Topaz
9	Corundum
10	Diamond

The UCS value is obtained by dividing the maximum load at the point of failure by the cross-sectional area (Miedema, 2015a). The BTS value provides a measure of the rock toughness as well as its strength (Miedema, 2015a). UCS tests are done by Dreiseitl and Kondratenko (2012) and they concluded that the UCS value depend on the size of the particle. The results vary from a UCS value of 3.26 MPa for nodules within the range of $0 \leq d \leq 20$ mm, to a UCS value of 0.68 MPa for nodules greater than 100 mm. Therefore it can be concluded that smaller nodule sizes are stronger than the larger sized nodules. Once the values for UCS and BTS are known, a conclusion could be made which failure mechanism will occur (Verhoef, 1997). The possible failure modes are discussed in chapter 3.

2.3.3. Density and Porosity of Polymetallic Nodules

In literature, different values for the density of polymetallic nodules can be found. Three different types of density are distinguished: dry density (ρ_d), situ density (ρ_{situ}) and solids density (ρ_s). The dry density is the mass of the solids, divided by the volume of the object (which includes the volume of air, water and solids) (Miedema, 2015a). The situ density, or mixture density (Miedema, 2015a), or volumetric density (Dreiseitl, 2017); defines the ratio between the weight of air, solids and water in a material, and the total volume of air, solids and water. For practical reasons the volume of air is taken as zero (Miedema, 2015a). Last, the solids density, is the ratio between the weight of solids over the volume of the solids, without taking the content of air and water into account.

In order to calculate the solids density of a polymetallic nodule, first the porosity, void ratio and water content should be determined. The porosity (n) is the ratio between the volume of voids (spaces) to the total volume of material (Miedema, 2015a). The void ratio (e) defines the ratio between the volume of spaces and the volume of solids (Dreiseitl, 2017). The water content (w) represents the amount of water contained in a nodule and can be expressed as the ratio of water evaporated (at 105°C) per mass of dry nodule (Dreiseitl, 2017). Equation 2.1 (porosity), Equation 2.2 (void ratio) and Equation 2.3 (water content), show the calculation of these properties.

$$n = w\left(\frac{\rho_d}{\rho_w}\right) \tag{2.1}$$

$$e = \frac{n}{100 - n} \tag{2.2}$$

$$w = \frac{m_w - m_d}{m_d} \tag{2.3}$$

Solid density measurements done by Mero (1965) resulted into a range between 2.07 g/cm^3 and 3.07 g/cm^3, with an average of 2.49 g/cm^3. This measurement was based on a single deposit of polymetallic nodules from the CCZ. Density measurements on nodules from seven different deposits, in the south west area of the CCZ, are done by Halbach et al. (1975). The mean values of the densities are as follows: ρ_d = 1.396 g/cm^3, ρ_{situ} = 1.99 g/cm^3 and ρ_s = 3.334 g/cm^3. Also the porosity was measured, having an average value of 58.31%. Glasby (1977) reported a solids density of 1.96 g/cm^3, which is more than 20% lower than the average value of Mero (1965). Zenhorst (2016) did also measurements on the density of polymetallic nodules from the CCZ. The nodules had a dry density of 1.385 g/cm^3, a solids density of 2.715 g/cm^3 and a situ density of 1.875

g/cm^3. Dreiseitl (2017) compared the physical properties of polymetallic nodules according to their size. The results of his work are represented in Table 2.3.

Table 2.3: Physical properties of manganese nodules according to their size (Dreiseitl, 2017)

Fraction [mm]		w [%]	ρ_{part} [g/cm^3]	n [%]	ρ_s [g/cm^3]	No. of trials
Small	0 - 20	53	1.87	63	3.32	6
	20 - 40	48	1.95	62	3.46	59
Medium	40 - 60	47	1.98	62	3.51	60
	60 - 80	47	1.98	61	3.50	54
Large	80 - 100	46	1.99	61	3.51	18
	> 100	48	1.96	62	3.50	5

Because several authors came up with different results for the density, it is decided to measure the density in the MTI laboratory. The method and results of the measurements are given in subsection 2.3.4.

2.3.4. Density Measurement of the Kinderdijk Nodules

Ten different sized nodules are picked from the available batch. In order to calculate the particle density (ρ_{part}), first the volume of the nodules is determined. The volume is determined in a cup partly filled with water, where the initial water level ($h_{initial}$) is marked. Then, after the nodule is placed inside the cup, the water level rises and the difference is measured (h_{final}). This method is schematically represented by Figure 2.16. The volume of a nodule (V_p) can be obtained, showed by Equation 2.4, using the diameter of the cup (d_{cup}) and the difference in water height for each specific nodule.

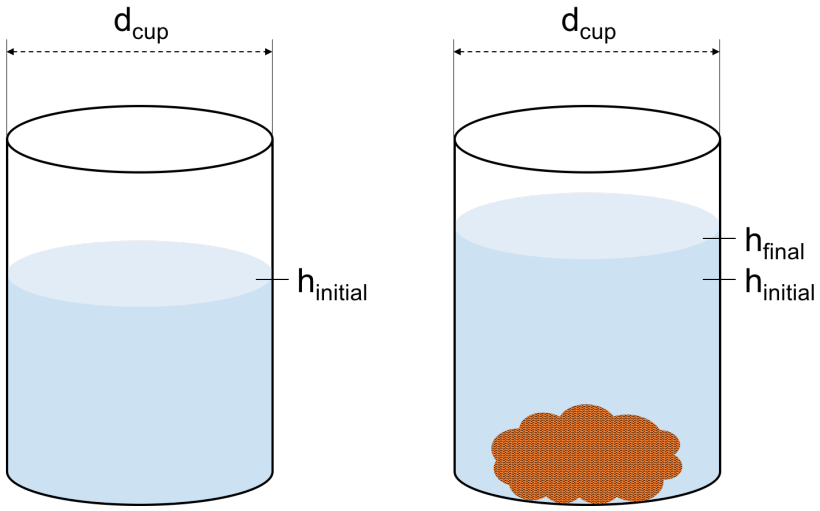

Figure 2.16: Schematic representation of the volume measurement of a polymetallic nodule

$$V_p = \frac{\pi}{4} d_{cup}^2 \left(h_{final} - h_{initial}\right) \tag{2.4}$$

Before each nodule was placed in the cup to measure the density, it was made sure that the nodule was saturated. They were placed in a bucket full of water for several hours. Then, each nodule was weighted to obtain the wet mass (m_w). With the volume of the nodule and its wet weight, the particle density is calculated using Equation 2.5. Results of these measurements can be found in Table A.2.

$$\rho_{part} = \frac{m_w}{V_p} \tag{2.5}$$

Next, in order to determine the other physical properties, the nodules are placed in a furnace at 105°C and their weight is checked after time intervals of hours. The results can be seen in Table A.3, where the numbers

between the brackets denote the time the nodules spend in the furnace. The initial (wet) weight is also given in this table, to point out the difference between a wet nodule and a complete dry nodule. After spending more than 28 hours in the furnace, the mass of the nodules did not decrease considerably.

With the dry mass known, the dry density (ρ_d) can be determined using Equation 2.6. Then, using Equation 2.1, Equation 2.2 and Equation 2.3, all the other physical properties can be calculated. Eventually, the solids density can be calculated using Equation 2.7. The solids density (ρ_s) of the nodules is calculated with the void ratio (e) and the dry nodule density (Dreiseitl, 2017). The obtained results are summarized in Table A.4.

$$\rho_d = \frac{m_d}{V_p} \tag{2.6}$$

$$\rho_s = \rho_d (1 + e) \tag{2.7}$$

As can be seen from Table A.4, the average solids density from the nodules in Kinderdijk is almost equal to the mean density obtained by Mero (1965) and the particle density is comparable to the measurements of Zenhorst (2016). For the calculations in this research it is decided to work with a particle density of ρ_{part} = 1700 kg/m^3 and a solids density of ρ_s = 2500 kg/m^3. The particle density (ρ_{part}) is defined as the density of a wet, porous nodule with water in the pores.

2.4. Deep Sea Mining in the Clarion-Clipperton Zone

Not everyone can just start mining polymetallic nodules from the CCZ. The International Seabed Authority (ISA) divided the CCZ into several different zones. In Figure 2.17 the division of the locations can be seen, whereat the “IHC-area” is located close to the German claim, area F (Zenhorst, 2016). The growing process of the manganese nodules is discussed in the followup subsection.

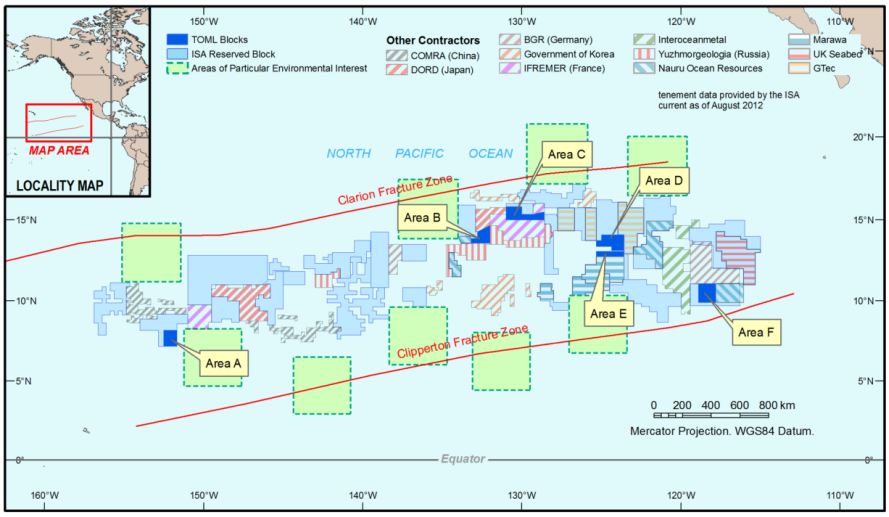

Figure 2.17: Claims of different contractors in the CCZ (Nimmo, 2013)

The CCZ distinguishes itself from the other zones by containing the highest nodule abundance per square meter around the world. Based on an average abundance of 15 kg/m^2 (Baker and Beaudoin, 2013; Skornyakova and Murdmaa, 1992), the International Seabed Authority (ISA) estimated that the total amount of nodules is more than 21 billions of tons (ISA, 2010). With this estimation the ISA concluded that the amount of cobalt could be 0.05 billion tons, which should be enough to satisfy the growing demand for the coming years (Figure 1.2). This makes the concept of deep sea mining an economical interesting opportunity (Van Wijk, 2016; Zenhorst, 2016).

2.4.1. Vertical Hydraulic Transport System

Vertical hydraulic transport from seafloor, at a depth of 5000 meter, to sea surface is a major challenge. Several vertical transport systems (VTS) has been proposed by IHC MTI throughout the years, whereas the most

recent proposal is done by Verichev et al. (2012). After years of research by Van Wijk (2016) and the EU-funded Blue Mining project, the final designing phase reaches its conclusion. The latest concept consists of a vertical pipe with six boosters stations. Each booster station has two centrifugal pumps. In Figure 2.18 an impression of the VTS is given (Verichev et al., 2012). A vertical S-bend will compensate for the motions of both the crawler as for the collection vessel. Research on coarse particle transport in vertical S-bends is done by De Hoog (2016).

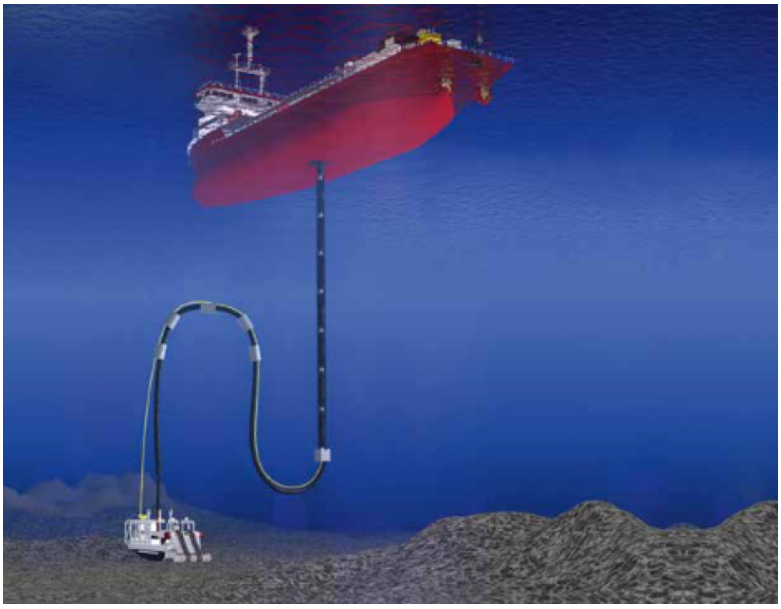

Figure 2.18: Impression of the VTS (Verichev et al., 2012)

2.5. Conclusions and Recommendations

The following secondary research questions were formed at the beginning of this chapter:

- *What causes the renewed interest of deep sea mining of polymetallic nodules?*
- *How come that the Clarion-Clipperton Zone is so suitable for deep sea mining purposes?*

2.5.1. Conclusions

What causes the renewed interest of deep sea mining of polymetallic nodules?

One of the pillars of the renewed interest in deep sea mining is the growing global demand for mineral resources, for example the rising demand for cobalt, as shown in Figure 1.2. The coming years cobalt becomes more valuable because of its unique properties and its applicability in many modern applications (Shedd et al., 2017). But also the content of rare earth elements makes the nodules valuable, subsection 2.3.1. A complete list of all the metals inside a polymetallic nodule can be found in Table A.1.

How come that the Clarion-Clipperton Zone is so suitable for deep sea mining purposes?

This chapter showed the global spread of polymetallic nodules, whereas four regions are distinguished. The Clarion-Clipperton Zone has a nodule abundance of 15 kg/m^2, which makes it the most abundant region in the world. With the increasing demand of mineral resources the coming years, this area will become very interesting. The total amount of nodules in the CCZ is estimated to be 21 billions of tons (ISA, 2010). With this estimation the ISA concluded that the amount of cobalt could be 0.05 billion tons, which should be enough to satisfy the growing demand for the coming years (Figure 1.2).

2.5.2. Recommendations

Polymetallic Nodule related Recommendations

During the experiments at the MTI laboratory, it became clear that manganese nodules are very brittle. With the sieving of the nodules many nodules broke on the sieve. Especially with the dry nodules from the furnace, for the density measurements, caution is required. It appeared that the nodules, once dried out, had lost their strength. This was caused by the clay layers inside the nodules that had lost their cohesive effect, sometimes referred to as sticky effect, due to the heating process. Therefore caution is required when working with (dried) polymetallic nodules. Furthermore it is recommended not to throw with nodules, Figure 2.19 shows the result of a nodule which has fallen from a desk.

Figure 2.19: Broken polymetallic nodule after falling from a desk

3

Theory - Degradation of Brittle Agglomerates

Degradation literally means *'the process in which the beauty or quality of something is destroyed or spoiled'*. As the title states, this chapter concerns the degradation of brittle agglomerates. Agglomerates, a word that can be described as *'a mass or collection of things'*. From the previous chapter it is learned that this description is completely valid for polymetallic nodules. The term brittle indicates that it is about agglomerates which are easily broken. In short, this chapter explains the destroying process of a rather weak collection of things, polymetallic nodules. This is done by means of three secondary research questions.

Secondary research questions of this chapter:

- *Which types of wear mechanisms could be encountered during slurry transport?*
- *How can particle degradation be quantified?*
- *What is the effect of wear mechanisms on brittle agglomerates?*

In section 3.1 an introduction on particle degradation during slurry transport is given. Complete slurry transport systems could be optimized due to particle degradation. For example, pumping power could be adjusted once coarse particles degraded to smaller sizes. In section 3.2, a description is given of particle degradation due to different wearing mechanisms. Also in this section, degradation due to abrasive wear is specified. This is followed by section 3.3, where an overview of earlier research on particle degradation is given. This chapter ends with section 3.4, containing an answer to the formed secondary research questions, conclusions and recommendations.

3.1. Introduction - Degradation during Slurry Transport

During slurry transport collisions are inevitable. Whether it concerns particle-particle collisions, particle-wall collisions or possible collisions with impeller blades of pumps. In Figure 3.1 the effect of particle degradation during slurry transport is shown. Particles become smaller and are rounded due to degradation. This research mainly concerns the effect of abrasive wear on particle degradation, however, in section 3.2 the other possible wear mechanism are shortly explained.

Figure 3.1: Example of particle degradation during slurry transport (Van den Berg and Alvarez Grima, 2006)

3.2. Particle Degradation caused by Wear Mechanisms

To understand the particle degradation inside the vertical transportation system (VTS), the principles and mechanisms of particle degradation should be grasped. Particle degradation can be described as the breakage of a (single) particle into multiple pieces, or as the mass loss of the parent particle (Zenhorst, 2016). Several authors, (Beekman, 2000; Pitchumani et al., 2004), defined four different failure mechanisms responsible for particle degradation: abrasion, attrition, chipping and fragmentation. These authors described the failure mechanisms as follows:

- Abrasion:
  Exertion of relative low tangential forces on a particle

- Attrition:
  Exertion of relative low normal forces on a particle

- Chipping:
  Exertion of relative high tangential forces on a particle

- Fragmentation:
  Exertion of relative high normal forces on a particle

As can be seen from the short description of the failure mechanisms, a distinction is made between the exertion of relatively low and high forces. The low force failure mechanisms can be assigned to wear, whereas the high force failure mechanisms are assigned to fracture. The wear mechanisms are schematically represented by Figure 3.2 (Beekman, 2000).

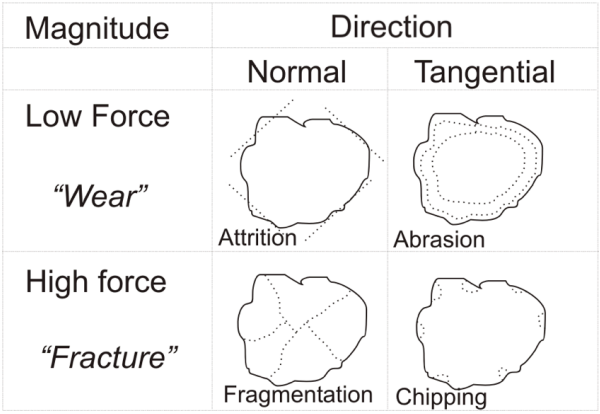

Figure 3.2: Different failure mechanisms, comparing to the force magnitude and direction (Beekman, 2000)

This research focuses on the low force tangential wear mechanism, abrasion. It is expected that this wear mechanism occurs when a particle slides along the pipe wall. In mining industry, wear due to abrasion is the most common type of wear (Petrica et al., 2013).

3.2.1. Distinction in Degradation due to Abrasion

Two main types of abrasive wear can be distinguished (e.g. Burwell (1957); Stachowiak and Batchelor (2014); Zum Gahr (1987)):

- Two-body abrasive wear:
  Hard asperities or rigidly held grits pass over the surface like a cutting tool (e.g. sandpaper on a surface)

- Three-body abrasive wear:
  The grits are free to roll as well as slide over the surface, since they are not held rigidly (e.g. Abrasive Wear Tester used for the experiments, section 4.2)

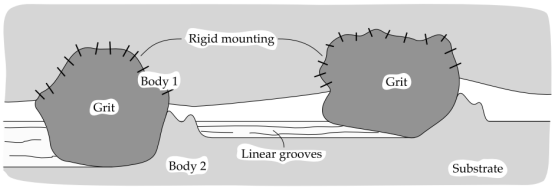

Figure 3.3: Two-Body Abrasion (Stachowiak and Batchelor, 2014)

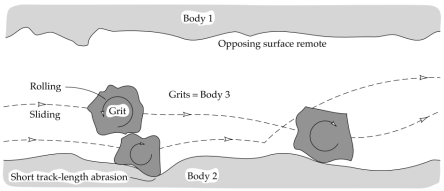

Figure 3.4: Three-Body Abrasion (Stachowiak and Batchelor, 2014)

In Figure 3.3 two-body abrasion is schematically shown and in Figure 3.4 three-body abrasion can be seen. It is likely that both occur in the VTS, however from the description above, it is assumed that three-body abrasive wear mainly occurs.

In three-body abrasion the abrasivity of particles plays an important role. The following three modes are considered:

- Very brittle grit particle

- Self-sharpening grit particle of moderate brittleness

- Very tough grit particle

In Figure 3.5 the three modes are schematically represented.

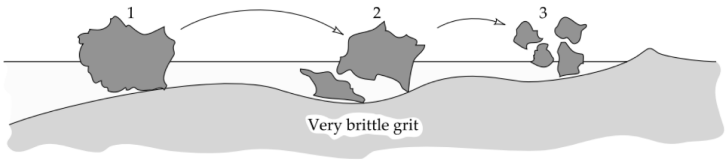

(a) Very brittle particle

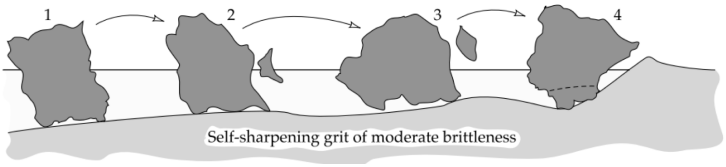

(b) Moderate brittle particle

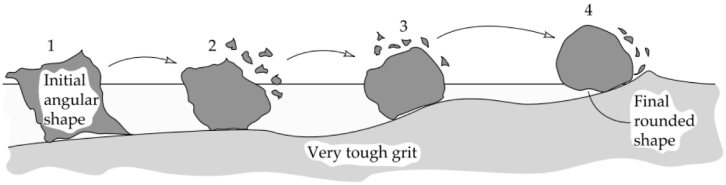

(c) Tough brittle particle

Figure 3.5: Effect of grit brittleness and toughness on abrasion effect (nodule degradation) (Stachowiak and Batchelor, 2014)

Physical properties such as particle hardness, particle shape and size (section 2.3) are dominant factors in the brittleness of a particle (Stachowiak and Batchelor, 2014). Polymetallic nodules are reported as weak particles with a relatively low UCS value (Zenhorst, 2016). Nodules with a low rate of calcium carbonate are brittle and easy to crush (Zenhorst, 2016).

3.2.2. Archard's Equation for Abrasive Wear

To quantify the contribution of abrasive wear other wear mechanisms (e.g. impact wear) should be excluded. The equation of Archard (1953) gives the relation between the sliding distance (s), the applied normal load (F_N) and its specific wear rate (k) (e.g. (Archard, 1953; Hutchings and Shipway, 2017; Van Beek, 2012)). The equation of Archard (1953) is given by Equation 3.1.

$$V_w = k\, F_N\, s \tag{3.1}$$

In Equation 3.1, V_w represents the worn volume in [m^3], k is the (material) specific wear rate in [m^2/N], F_N is the normal force acting on the material in [N] and s represents the sliding distance in [m]. The material specific wear rate of polymetallic nodules is unknown. This value will be determined experimentally in chapter 4. A table with specific wear rates of different materials is given in Table 3.1. The higher the class, as shown in Table 3.1, the faster the volume of the object is worn, according to Equation 3.1.

Table 3.1: Classification of the specific wear rate (k) (Van Beek, 2012)

$k \cdot 10^{-15}$ [m^2/N]	Class
0.0001 - 0.001	0
0.001- 0.01	1
0.01 - 0.1	2
0.1 - 1.0	3
1.0 - 10	4
10 - 100	5
100 - 1000	6
1000 - 10000	7
>10000	8

3.3. Earlier Research on Particle Degradation

From the pioneers Worster and Denny (1955) until today, particle degradation during slurry transport is an interesting subject. Complete slurry transport systems could be optimized due to particle degradation. First, in subsection 3.3.1, an overview of experimental setups and its results is described, which is followed by a discussion in subsection 3.3.2.

3.3.1. Overview of Experimental Setups and its Results

In this section an overview of earlier research on particle degradation is given. For each research first an introduction is given, followed by a description of the experimental setup. Then, the used materials and its properties is described. Thereafter the results are given, for some authors this is done by means of an equation, for others this is done by means of a graph or prediction. Each part is finished with the conclusions of the researches and how they relate to this research on polymetallic nodule degradation.

Worster and Denny (1955)

One of the earliest works on particle degradation was done by Worster and Denny (1955). In their research, they distinguished '*degradation by machinery*' and '*degradation of coal traveling along pipes*'. For this research the results and conclusions of the latter is of importance.

To mimic large traveling distances and to minimize space in their laboratory, the authors used a continuously rotating ring. In Figure 3.6 a part of the experimental setup can be seen. Experiments were done with different rotating speeds, in order to investigate the effect of velocity on particle degradation. Worster and Denny (1955) used batches of goal weighing 2 lb (≈ 0.9 kg) and 3 lb (≈ 1.4 kg). The passings of the coal varied from 1/16 inch (≈ 1.6 mm) to 1 inch (≈ 25.4 mm). The density of coal is around 1350 kg/m^3.

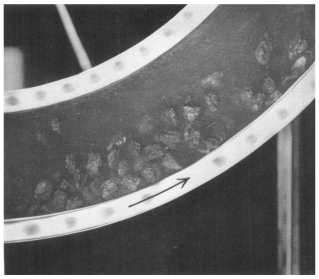

Figure 3.6: Particle degradation tester used by Worster and Denny (1955)

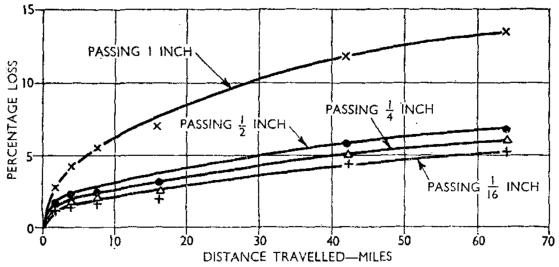

Figure 3.7: Particle degradation results obtained by Worster and Denny (1955)

After the experiments a relation between the total loss of material (coal), the rotational speed and corresponding distance was obtained. The relationship is given in Equation 3.2. In Figure 3.7 the results of their research can be seen. The results are plotted as percentage loss (in %) against the traveling distance (in miles).

$$Total\ loss \propto (speed)^3 \sqrt{(distance)} \tag{3.2}$$

Due to the rolling of the particles inside the test rig, the authors concluded that attrition was the acting wear mechanism. They found that the degradation of coal not only results in a reduction of the market value, but also produces very fine material which creates an effluent problem. This has all to do with the dewatering costs and the settling time of fine material. Also, it must be kept in mind that these tests were done with batches of coal and not with a single coal particle. Thus, in the degradation experiments of Worster and Denny (1955) particle-particle interaction also plays a role, which probably leads to an extra wear mechanism.

To compare the results and conclusions of Worster and Denny (1955) with the degradation of polymetallic nodules, is by means of the size of the biggest coal particles (passing 1 inch). This size is however relatively small for a nodule from the CCZ, but this size certainly occurs in the pumped up batches. Because attrition is the main degradation mechanism in their experiments, the comparison will probably hard.

Van den Berg and Alvarez Grima (2006)

The effect of particle degradation on slurry performance is studied by Van den Berg and Alvarez Grima (2006). They wanted to see whether a hydraulic transport system could be optimized using the effect of the degradation during transport.

In the MTI laboratory in Kinderdijk, a 310 mm recirculating flow loop was made. The test setup has a total length of 124 m and consists of 10 90° bends. The experimental setup is shown in Figure 3.8. Experimental results were compared with four materials: limestone, rock salt, coarse gravel and quarts sand. In the flow loop limestone and coarse gravel were tested, for the rock salt and quartz sand data from practice is used.

The limestone had a mean grain size of 18 mm, a solids density of around 2290 kg/m^3 and a hardness of 3 Moh. The material was tested for 4 kilometers in the flow loop until the material was almost completely degraded. It was concluded by the authors that the degradation process for limestone will be determined mainly by abrasion. This will not only hold for limestone, but also for other weak homogeneous materials. It implies that abrasion will occur continuously during the transportation process.

Rock salt, which was dredged in Saudi-Arabia, has a density of 2160 kg/m^3 and a hardness of 2-3 Moh. The dimensions before entering the dredging system were 50 x 50 x 70 mm (very coarse angular lumps). But after the first 600 m the dimensions already reduced to 20 x 20 x 30 mm. After 2500 m and three pumps the material reduced a factor ten, the dimensions of rock salt were 5 x 5 x 5 mm. Van den Berg and Alvarez Grima (2006) concluded that the lumps of rock salt showed the same degradation behaviour as for the limestone. The crushing of the material was an effect of the frictional forces in the sliding bed, whereas the lumps were broken by impact due to the presence of pumps.

The coarse gravel tested by Van den Berg and Alvarez Grima (2006) had a mass median diameter (d_{50}) of 17.2 mm and a mixture density of 1200 kg/m^3. On the scale of Moh, the harness of gravel is 7. The total sample contained particles between the 10 and 30 mm. The mixture velocity inside the flow loop was 5 m/s.

For quarts sand the authors concluded that the degradation due to abrasion is so slow, that it is negligible in most transport situations.

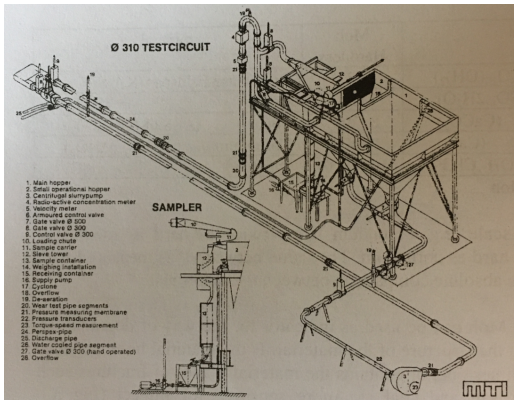

Figure 3.8: Experimental setup of Van den Berg and Alvarez Grima (2006)

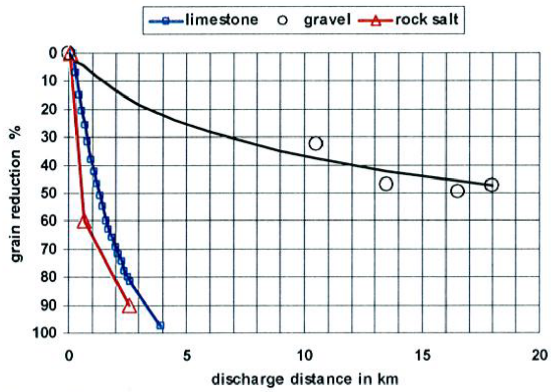

Figure 3.9: Particle degradation results obtained by Van den Berg and Alvarez Grima (2006)

Limestone and rock salt almost completely degraded, as can be seen in Figure 3.9. Rock salt showed a very strong degradation behaviour. For the coarse gravel the grain size reduction was 50%. In their conclusion, Van den Berg and Alvarez Grima (2006) made a distinction in degradation as an effect of impact (pumps and bends) and degradation by abrasion (pipeline). They concluded that materials with at least a hardness of 5 Moh, the degradation process is mainly caused by impact and less by abrasion.

The authors concluded, like Worster and Denny (1955), that fines not only greatly increase the dewatering and drying costs, but fines could also result in a higher viscosity of the transportation medium. Van den Berg and Alvarez Grima (2006) stated that the dewatering costs of 6 mm fine coal are almost 10 times as those of the particles greater than 6 mm.

In order to compare the results of Van den Berg and Alvarez Grima (2006) with the degradation of polymetallic nodules, is by means of the coarse gravel due to its size and density. Although the size and density are comparable, the hardness of the particles differs greatly. Also, the presence of a pump and bends in their setup is a disadvantage when testing the effect of abrasion as degradation mechanism, because impact wear will occur inevitably.

Van Laarhoven (2010)

The effect of attrition, abrasion and compression on brittle agglomerates is studied by Van Laarhoven (2010). For the abrasive wear tests an abrasive wear tester is developed. This tester was specially designed to exert only tangential forces on particles, in order to exclude the effect of other wear mechanisms.

The experimental setup consists of a rotating arm with a DC (direct current) motor on one end and a counter weight on the other end of the arm. The experimental setup is shown in Figure 3.10. A particle box is connected to the DC motor, causing a planetary motion of the box. Due to the rotating motion of the arm and the particle box, centrifugal force will act on the particle, whereas the centrifugal forces of the arm are greater than the centrifugal forces of the particle box. This results into a particle which is continuously sliding and rolling in the box (Van Laarhoven, 2010).

Three different materials were tested: sodium benzoate granules, placebo granules and sugar crystals. A narrow PSD curve is made by sieving the particles on a 1.4 mm sieve and collecting those who remained in the mesh after sieving. This is done in order to reduce the particle size effect on the results (Van Laarhoven, 2010).

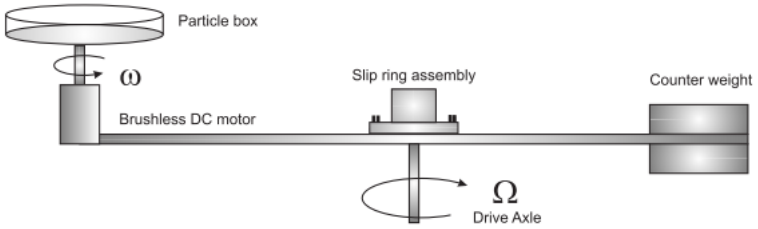

Figure 3.10: Abrasive wear tester developed by Van Laarhoven (2010)

After the experiments, the particles remaining on the 1.4 mm sieve are weighted again and a PSD is determined. The weight remaining on the sieve is divided by the initial weight, resulting into a ratio between the new and initial mass. Next, this remaining mass ratio is plotted against testing time. The results are shown for the sodium benzoate granules, for three different velocities of the particle box, in Figure 3.11.

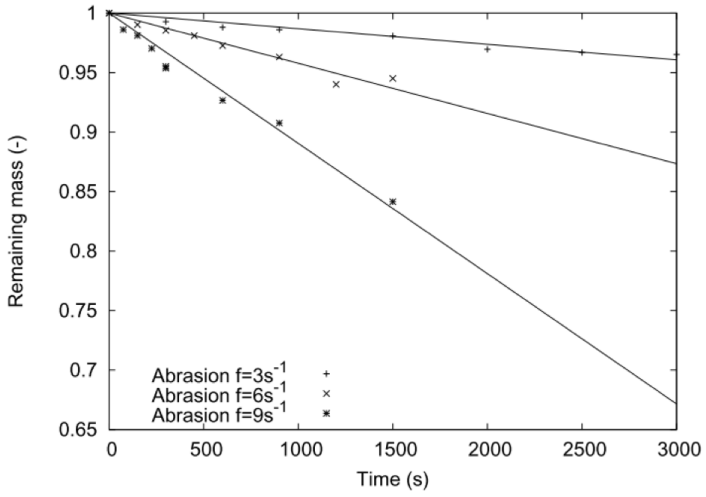

Figure 3.11: Normalized remaining mass on a 1.4 mm sieve, plotted against time (sodium benzoate granules) (Van Laarhoven, 2010)

Van Laarhoven (2010) defined the normalized remaining mass (m_n), which is plotted on the vertical axis of Figure 3.11, as follows by Equation 3.3. In Equation 3.3, the initial mass is defined as m_1 and m_2 gives the mass after sieving.

$$m_n = \frac{m_2}{m_1} \tag{3.3}$$

In his study the author tested particles with a diameter of 1.4 mm, which are very small compared to the nominal size of manganese nodules. Notable of the results in Figure 3.11, is the linear trend of the graphs. This behaviour is also expected when the theory of Archard (1953) is applied on the degradation of polymetallic nodules due to abrasion. Therefore, the results of the experiments for this research are also expressed as normalized remaining mass. Only then plotted against distance instead of time, since the equation of Archard (1953), Equation 3.1, contains (sliding) distance.

Vlasák et al. (2015)

In '*experimental investigation of coarse particle conveying in pipes*' by Vlasák et al. (2015) basalt pebbles are pumped in their 100 mm inner diameter flow loop. Their main goal was to investigate the flow behaviour experimentally, depending on the mixture velocity and concentration of the particle-water mixtures. During their experiments they found that the used basalt pebbles degraded and had changed from angular shape to a round-off shape.

The experimental setup consists basically of three sections; a horizontal, vertical and inclined section. The experimental setup used in the research of Vlasák et al. (2015) is shown in Figure 3.12. As stated before, the used material were basalt pebbles with a density of 2787 kg/m^3. Particle diameters ranged from 8 mm to 16 mm, whereas the mass median diameter (d_{50}) was initially equal to 11.7 mm. The initial, angular shaped basalt pebbles, are shown in the left figure of Figure 3.14.

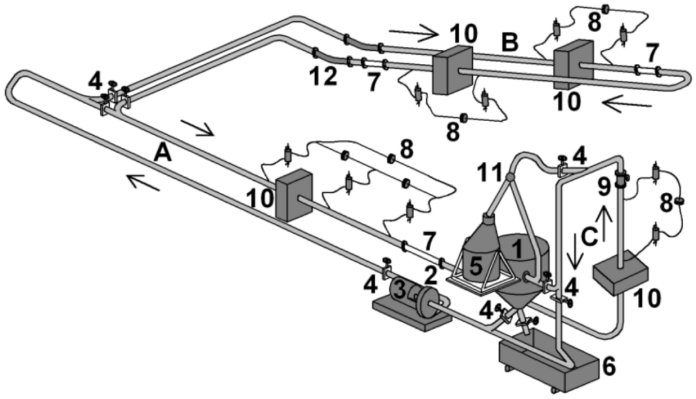

Figure 3.12: Experimental setup by Vlasák et al. (2015)

After shortly pumping at a mixture velocity of 3.5 m/s, the authors saw that the particle shape and size became partially stable. They concluded that the degradation of solids occurs when mixture velocities exceed 3 m/s, or when a mixture contains a high concentration of solids. The (d_{50}) of the basalt pebbles was shifted from 11.7 mm to 11.0 mm, whereby particles had formed smaller than 5 mm. Although the created particles smaller than 5 mm did not exceed 10% of the total mass, this is another example of the creation of fines during coarse particle transport. The wear mechanisms acting in this setup were probably dominated by abrasion and attrition, even with the presence of a pump. Basalt has a hardness of around 3 Moh, and with the conclusion of Van den Berg and Alvarez Grima (2006) it holds that basalt is more susceptible for abrasive wear instead of impact wear.

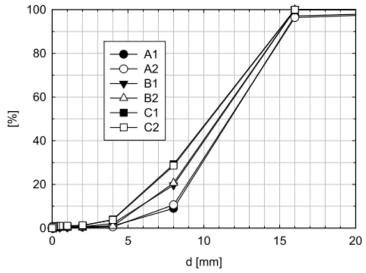

Figure 3.13: PSD of the basalt pebbles from Vlasák et al. (2015)

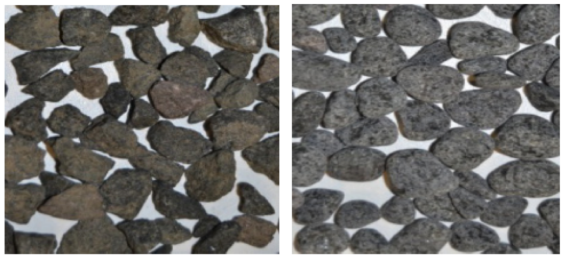

Figure 3.14: Graded basalt pebbles by Vlasák et al. (2015)

In order to compare basalt pebbles with polymetallic nodules, the hardness of both materials is more ore less the same. The density of basalt and particle sizes that has been used for the work of Vlasák et al. (2015) differs. The round-off process, as seen for their pebbles, is also expected to see for the nodules. The nodules are quite angular formed, as described in section 2.3. From the results of Vlasák et al. (2015) that relate to degradation of coarse particles, it is stated that the d_{50} only slightly changes after pumping, about 94% of its initial value. From the PSD in Figure 3.13 the creation of fines could be seen as an increase of the cumulative percentages from the smaller particle sizes, which were (possibly) not present in the initial batch. This is due to the fact that in the initial batch no particles exist smaller than 8 mm. And after pumping, part of the batch, almost 10% is smaller than 5 mm. In their experiments, Vlasák et al. (2015) noticed a production of fine material. This should also be noticed during the batch experiments in this research, which is explained in chapter 5.

Zenhorst (2016)

The degradation of polymetallic and artificial nodules in centrifugal pumps is tested by Zenhorst (2016). The degradation process is mainly caused by the impact between the nodules and the impeller blades of the centrifugal pump. During the experiments of Zenhorst (2016), polymetallic nodules from the CCZ and two types of artificial nodules are used.

In order to test the effect of impact wear on the degradation of nodules, an experimental setup consisting of a centrifugal pump and a short circuit is used. A schematic representation of the experimental setup of Zenhorst (2016) is given in Figure 3.15. In Figure 3.16 a picture is given of the setup. The materials that the author used were polymetallic nodules from the CCZ and self-made nodules. The initial PSD curve of the real polymetallic nodules is represented in blue in Figure 3.17.

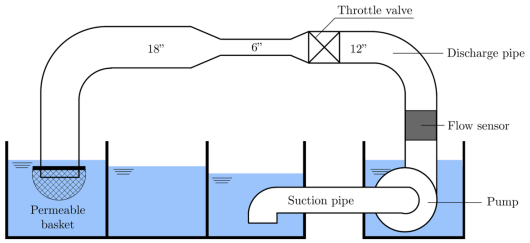

Figure 3.15: Schematic representation of the experimental setup of Zenhorst (2016)

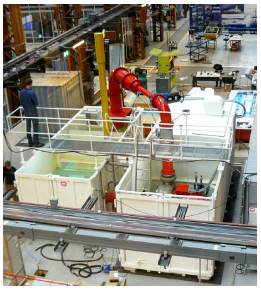

Figure 3.16: Picture of the experimental setup of Zenhorst (2016)

The results of the impact experiments by Zenhorst (2016) are plotted as a PSD curve. Other than the degradation of the basalt pebbles from Vlasák et al. (2015), the d_{50} changed quite a lot. The downside from the experiments from Zenhorst (2016) is that the fines could not be recovered, otherwise an increase in cumulative mass percentage of (very) fine material could be seen. Although, the author gave an insight in what impact wear does to a batch of nodules, as shown by the author pictures the took (Figure 3.18 and Figure 3.19).

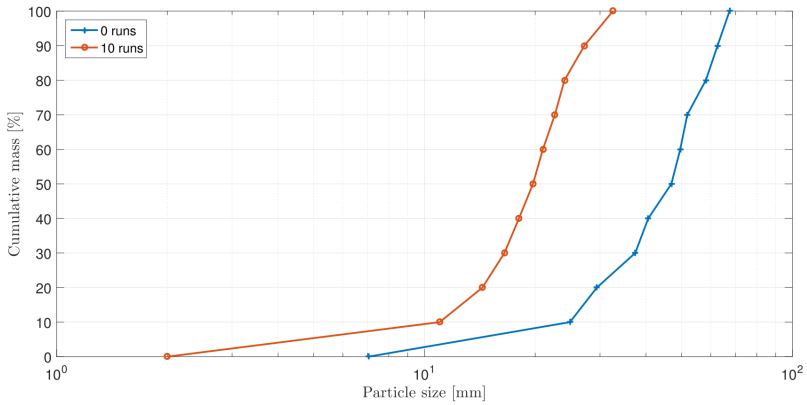

Figure 3.17: Particle degradation results obtained by Zenhorst (2016)

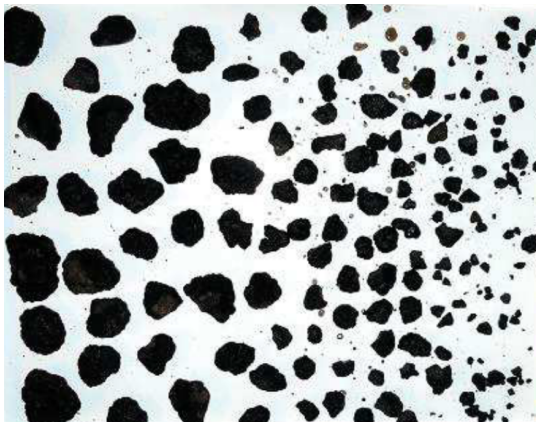

Figure 3.18: Batch of nodules before the experiments of Zenhorst (2016)

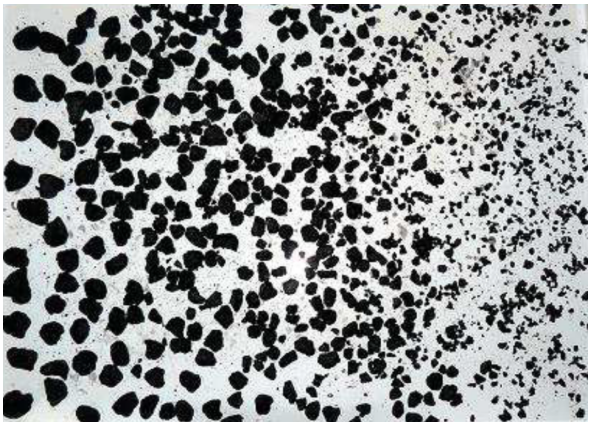

Figure 3.19: Batch of nodules after the experiments of Zenhorst (2016)

The advantage of the experiments by Zenhorst (2016) is that there was tested with real manganese nodules. It is learned from his work that the d_{50} decreases largely due to impact wear. Thus, for the abrasive wear tests in this research, a very small decrease in d_{50} should be seen, otherwise impact wear would prevail above abrasive wear.

Van Wijk (2017)

Theoretical research on nodule degradation during vertical hydraulic transport is performed by Van Wijk (2017). The modeling of degradation in his work is done by means of Equation 3.4.

$$\frac{d_{i,N}}{d_{i,0}} = x_i \, e^{-k_i N} \tag{3.4}$$

In Equation 3.4 the initial particle diameter is given by $d_{i,0}$ with i representing the fraction in the PSD. The N represents the number of passages through the centrifugal pump and k_i is a fraction specific constant. The result is plotted in Figure 3.20. In Figure 3.20, the effect of particle degradation on a distribution curve is plotted after each booster station in the VTS.

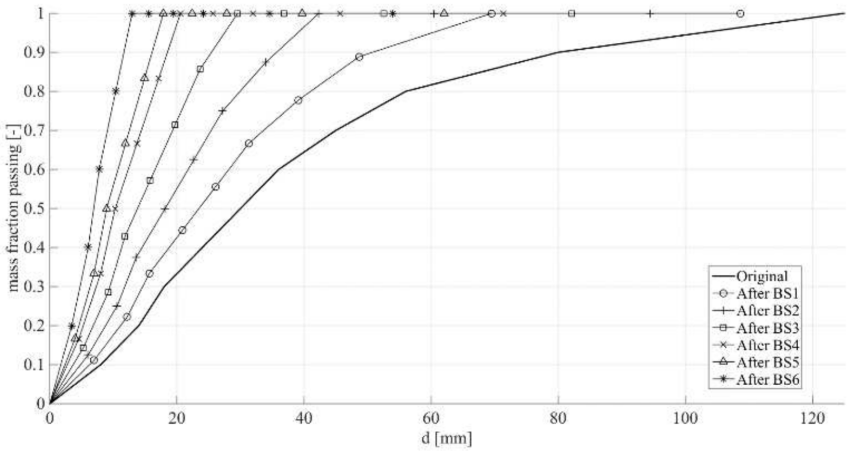

Figure 3.20: Particle degradation results obtained by Van Wijk (2017)

The narrowing of the PSD after the booster stations, is an effect of impact wear in the booster stations. Again, a large decrease in d_{50} can be seen, which was noticed in the work of Zenhorst (2016). This research of Van Wijk (2017) is mainly focussed on the effect of impact wear in the booster stations of the VTS. There is no effect of sliding wear along the pipe wall taken into account.

3.3.2. Discussion on Earlier Research

The experimental setup of Worster and Denny (1955) consist of a rotating ring in which, without the presence of a pump, large traveling distances can be tested. The disadvantage of this setup is that particle degradation due to abrasion cannot be guaranteed. The authors concluded that attrition was the main wear mechanism. But, impact wear will not be present due to the absence of pumps and bends.

The conclusions of Van den Berg and Alvarez Grima (2006) are useful to understand the relation between degradation and material properties. They linked the hardness of a material with the sensitivity to a specific wear mechanism. If the hardness is lower than 5 on the scale of Moh, it is likely that abrasive wear will prevail the particle degradation. Unfortunately their setup consisted of a pump and several bends, so the effect of impact wear cannot be excluded during the testing trials.

Van Laarhoven (2010) has shown a linear trend in particle degradation due to abrasive wear. The fact remains, however, that the used particle sizes are small, compared to the polymetallic nodules. Though, the experimental results of the single nodule experiments, given in chapter 4, shall be plotted as normalized remaining mass against sliding distance.

With the work of Vlasák et al. (2015), it is known that the d_{50} will not decrease significantly due abrasive wear and attrition. What is seen, is a production of fines, which causes an increase in cumulative percentage of the smaller particle sizes. This conclusion is useful for batch experiments with nodules (chapter 5).

From Zenhorst (2016) it is clear that impact wear decreases the d_{50} of a batch of nodules. Together with the work of Vlasák et al. (2015), it could be concluded that a PSD curve partly shifts to the left, due to impact wear and that the smaller particle size classes contain more material, due to the effect of abrasive wear.

The theoretical model of Van Wijk (2017) made an insight of polymetallic nodule degradation during vertical transport over a distance of 5000 meter. However, this model only incorporates the effect of impact wear on nodule degradation. The effect of abrasion on the nodules should be added to this model. Then, a prediction of the particle degradation during vertical transport can be made.

3.4. Conclusions and Recommendations

The following secondary research questions were formed at the beginning of this chapter:

- *Which types of wear mechanisms could be encountered during slurry transport?*
- *How can particle degradation be quantified?*
- *What is the effect of wear mechanisms on brittle agglomerates?*

3.4.1. Conclusions

Which types of wear mechanisms could be encountered during slurry transport?

Four different failure mechanisms are responsible for particle degradation during slurry transport: abrasion, attrition, chipping and fragmentation. Each mechanism is an effect of the exertion of a force in a specific direction.

How can particle degradation be quantified?

In this research particle degradation is quantified as an effect of abrasive wear. This done by means of the equation of Archard (Archard, 1953). In order to test this for polymetallic nodules, in case a single nodule is used, the parent nodule is weighted before and after a test. Then, the weight loss is quantified as particle degradation due to abrasive wear.

For a batch of nodules the creation of fine material will be used as a quantification of particle degradation. The percentage increase of particle sizes which were not present in the initial PSD is quantified as particle degradation.

What is the effect of wear mechanisms on brittle agglomerates?

Brittle agglomerates, as the name states, are soft materials. For polymetallic nodules the hardness varies between the 1-4 Moh, subsection 2.3.2 (Mero, 1965). According to Van den Berg and Alvarez Grima (2006) it is likely that materials with a hardness of less than 5, are more effected by abrasive wear than impact wear. Particles will be rounded during transport, until they have reached a certain size. The polymetallic nodules have a higher strength for smaller particle sizes (Dreiseitl, 2017).

3.4.2. Recommendations

Polymetallic Nodule related Recommendations

It is recommended to perform research while using polymetallic nodules from the zone which is considered to mine in the future. Lessons could be learned from degradation research of other materials, however, the best insight in the degradation behaviour is provided using the desired material.

Experimental Setup related Recommendations

In order to quantify particle degradation due to abrasive wear, it is recommended that other wear mechanisms are excluded as good as possible. As seen in section 3.3, pumps and bends in experimental setups resulted into impact (fragmentation) wear on particles. For testing the effect of abrasive wear, pumps and bends should not be present in an experimental setup.

4

Scale Model Experiments I - Degradation of a Polymetallic Nodule

A scale model is known as *'a representation or copy of an object that is larger or smaller than the actual size of the object being represented'*. An experimental setup with the actual size of a deep see mining vertical transport system does not fit inside the MTI laboratory in Kinderdijk. Therefore, a scale model provides an ideal solution. This chapter describes the first set of experiments and provides an answer to two secondary research questions.

Secondary research questions of this chapter:

- *Is the equation of Archard applicable for polymetallic nodule degradation due to abrasive wear?*
- *Does the sliding velocity influence the degradation due to abrasive wear?*

In section 4.1, an introduction is given of this chapter, whereas the design of the experimental setup is shortly explained. This section also provides a list of assumptions, used during the experiments. The theory behind the experimental setup and hypotheses are provided in section 4.2. In section 4.3, first the experimental setup is explained in detail. This is followed by the experimental plan, whereas the test parameters are given. Last of this section is the experimental data processing. The experimental results and a discussion about the obtained results can be found in section 4.4. This chapter ends with an answer to the formed secondary research questions, conclusions and recommendations in section 4.5. In Appendix A details of the experiments can be found (mass data of the used polymetallic nodules for example). In Appendix C a measurement scheme for the test setup can be found. Also in this appendix a kinematic analysis of the test setup is provided.

4.1. Introduction - The Abrasive Wear Tester

In order to mimic the effect of abrasive wear on polymetallic nodules during transport, an experimental setup is developed in the MTI laboratory, in Kinderdijk.[1] The experimental setup is basically a tilting pipe, like a seesaw. The repeating seesaw motion of the ends will cause the nodule to slide from one side to the other, over and over again, so that large sliding distances can be simulated. As described in section 3.2, abrasion occurs due to relative low tangential forces on a particle (Pitchumani et al., 2004). Therefore, it is necessary to maintain a sufficient low speed, in order to secure the sliding motion of the nodule and exclude the possible effects of other wear mechanisms. A computer render of the experimental setup is shown in Figure 4.1. The experimental setup is called the Abrasive Wear Tester and is referred to as AWT. Details of the AWT can be found in subsection 4.3.1.

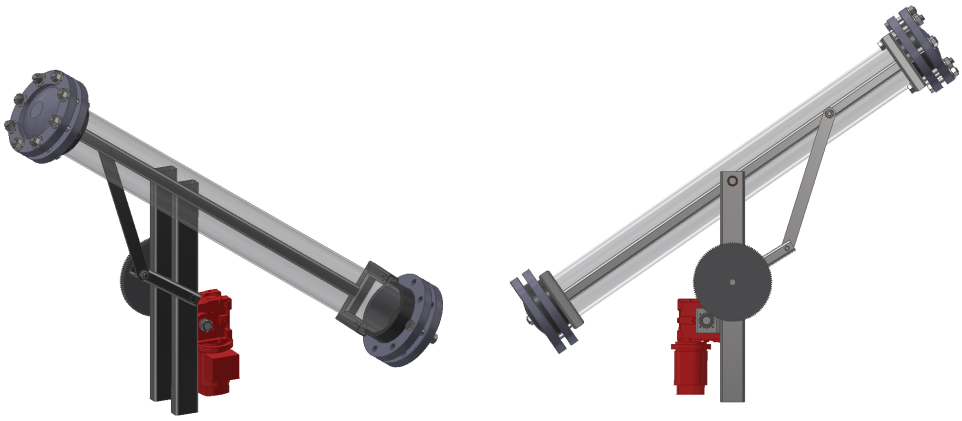

(a) 3D view (b) Back view

Figure 4.1: Computer render of the Abrasive Wear Tester (AWT)

Experimental Assumptions

The assumptions used for the experiments are listed below. After each assumption there is referred to the specific (sub)section where it is used and/or clarified.

1. It is assumed that the particle density, ρ_{part}, remains constant during a test run (subsection 4.3.2).
2. The mass loss of a nodule during a test, does not influence the applied normal force (F_N), considerably (subsection 4.3.2).

4.2. Theory - Abrasive Wear in the Experimental Setup

In subsection 3.3.1 - Overview of Experimental Setups and its Results - it is shown that different setups were used in the past to study the effect of (coarse) particle degradation. It is also concluded that if the effect of abrasive wear on polymetallic nodule degradation is studied, other wear mechanisms should be excluded. In the Abrasive Wear Tester (AWT), shown by Figure 4.1, there is no effect of impact wear due to the presence of a centrifugal pump and/or bends in the setup.

Using the AWT, whereas the nodule is in constant contact with the pipe wall, it is validated if the equation of Archard (1953) can be used to predict nodule degradation due to abrasive wear. The equation is shown in Equation 3.1 and its details are given in subsection 3.2.2. The use of this equation and its applicability to this experimental setup is explained in section 4.3.

$$V_w = k\, F_N\, s \tag{3.1 revisited}$$

In order to make sure abrasive wear is the acting wear mechanism inside the AWT, rubber packings which cover the flanges are used on both ends. The rubber will act as a damper or cushion while slowing the nodule down. Furthermore, the AWT rotates with a sufficient low speed, whereas the nodule stays in contact with the pipe and does not start bumping over the pipe wall during its downward motion.

[1] In cooperation with Dr. ir. J.M. van Wijk and Ir. E. de Hoog from IHC MTI

4.2.1. Hypotheses

The following hypotheses are formed based on the secondary research questions given in this chapter:

- *Hypothesis 1:*

  The abrasive wear equation of Archard is valid for polymetallic nodule degradation due to abrasive wear; there is a linear relation between the worn volume and sliding distance.

  Materials have their own classification of specific wear rate (k), as shown in Table 3.1, therefore the specific wear rate of polymetallic nodules should be found first in order to apply the equation of Archard (1953). Using the value for the k-factor, the linear degradation behaviour can be validated.

- *Hypothesis 2:*

  Abrasive wear can be written as a function of sliding distance, but also as a function of sliding velocity, integrated over (sliding) time.

  The equation of Archard (1953), Equation 3.1, can be written as follows by Equation 4.1. In order to obtain the velocity of the sliding nodule, nodules are tracked during a test run, subsection 4.3.3. Thereafter, the velocity profiles can be integrated over time and substituted into Equation 4.1.

$$V_w = k\,F_N\,s = k\,F_N \int_{t=t_0}^{t=t_n} v_{slide}\,dt \tag{4.1}$$

A validation or falsification of these hypotheses can be found in subsection 4.5.1.

4.3. Experiments - Polymetallic Nodule Degradation of a Single Nodule

In this section first the specifics of the experimental setup are given in subsection 4.3.1. The experimental plan, whereas the test parameters are explained, is provided in subsection 4.3.2. This section ends with the experimental data processing in subsection 4.3.3. A measurement scheme for the fulfillment of the experiments with the AWT, can be found in Appendix C.

4.3.1. Experimental Setup

In this subsection the equipment used for the test setup and its dimensions, is described. Before the construction of the setup, a computer render was made, shown in Figure 4.1. The experimental setup consist of the following parts:

- 150 mm inner diameter transparent PVC pipe and a length of 1.50 m
- High speed camera to record the motion of the nodule
- Step counter to keep track of the total sliding distance
- Two rubber packings which cover the complete flanges (except for two small holes for water in- and outflow) - to prevent impact wear between the sliding nodule and the flange
- Frequency controller which controls the input of the electrical motor
- Data logger and computer for data collection
- Tapping points for water in- and outlet

The high speed camera is used to film the nodule, and thereafter obtain the sliding velocity of the nodule, as described in subsection 4.3.3. These velocity profiles are used to validate hypothesis number 2 (subsection 4.2.1). In order to control the sliding distance of a nodule, s, which is set on beforehand of a test run, a step counter is used. The step counter registers the moment when the lever arm which holds the pipe, comes by. It should be kept in mind that if the step counter registers a step, the nodule has slid from left to right and in opposite direction. One additional step holds a sliding length of two times the length of the pipe. *For example, if a sliding distance of 600 meters is desired, the test run should be stopped if the number of steps is equal to 200.* In Figure 4.2 a picture of the AWT can be seen.

Figure 4.2: Picture of the Abrasive Wear Tester at the MTI laboratory

Specifics of the used equipment for the experimental setup is given in Table 4.1.

Table 4.1: Used equipment for the experimental setup

Data acquisition	DEWE-43A & DEWESoft SIRIUS
Electric motor	Euronorm Drive Systems (1,1 kW; 15 kN)
High-speed camera	DEWESoft DS-CAM-600 (Velociraptor)
Photoelectric sensor	Banner Engineering QS18VP6LPQ8 (10-30V)
Rotary encoder	Contelec Vert-X 13
Software	DEWESoft X

4.3.2. Experimental Plan

First, experiments are executed with a single nodule. The experiments with a batch of nodules are described in chapter 5. In case a single nodule is used, the effect of particle-particle interaction is excluded. This is a first step to gain insight in the specific wear rate of manganese nodules (k) and to use this result in the abrasive wear equation of Archard (1953) (Equation 3.1). Tests are performed with several different nodules and different testing lengths.

$$V_w = k\, F_N\, s \tag{3.1 revisited}$$

The sliding distance, represented by s in Equation 3.1, is the only test parameter which can be set before a test run. Multiple nodules will therefore be tested on equal sliding distances, in order to compare the degradation due to abrasive wear on a nodule.

The result of the Equation 3.1, is the worn volume (V_w). In order to measure the worn volume of a polymetallic nodule, the nodule is weighted before (m_1) and after (m_2) a test. Then, using the particle density, obtained in subsection 2.3.4, the worn volume can be determined. It is assumed that the particle density, ρ_{part}, remains constant during a test run. This holds that the particle density before a test is equal to the particle density after a test. The worn volume leads to a volume decrease what in fact causes a different nodule density, but with the decrease in mass kept in mind, this is effect is considered to be negligible. The worn volume of a polymetallic nodule can be calculated using Equation 4.2.

$$V_w = \frac{m_1 - m_2}{\rho_{part}} \tag{4.2}$$

Equation 4.2 can be substituted into Equation 3.1. After substitution and rewriting, the specific wear rate (k) can be calculated, which is shown in Equation 4.3. Several different nodules will be tested on different,

and equal sliding lengths (s), in the Abrasive Wear Tester (shown in Figure 4.2). By using different nodules and different sliding lengths, the (average) specific wear rate can be determined.

$$k = \frac{m_1 - m_2}{F_N \, s \, \rho_{part}} \tag{4.3}$$

The last parameter which influences the specific wear rate, is the applied normal force, F_N. The tilting motion of the Abrasive Wear Tester (AWT) results into a varying normal force during the experiment, this is schematically represented by Figure 4.3. The normal force reduces with an increasing angle, therefore it is necessary to take the angle variation into account. In Figure 4.3 a schematic representation of the increasing pipe angle (θ) and the resulting force balance can be seen. Using a force balance in y-direction, Equation 4.4 can be derived.

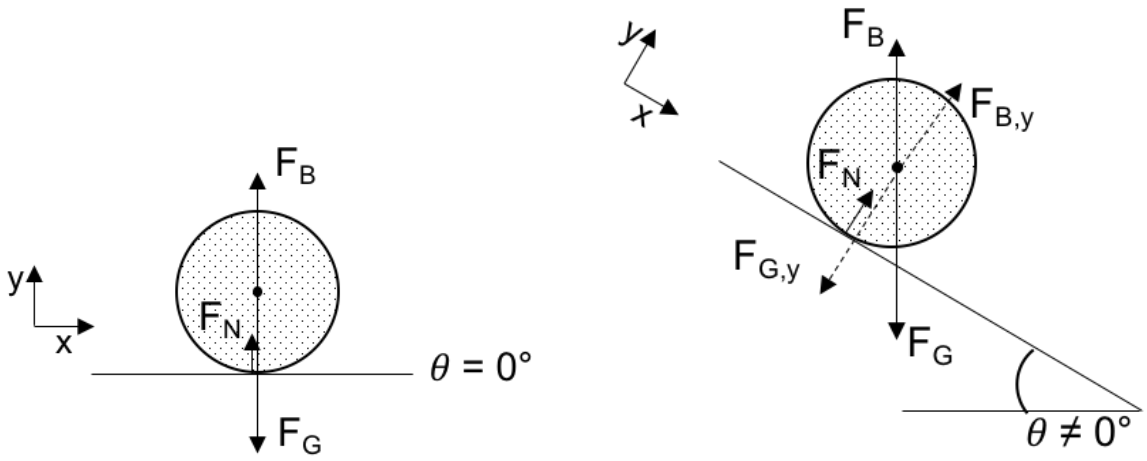

Figure 4.3: Variation of normal force (F_N) with increasing pipe angle (θ) schematically represented

$$F_N = (F_G - F_B)\cos(\theta) \tag{4.4}$$

From the force balance in Equation 4.4 it can be concluded that the normal force (F_N) is decreasing when the angle of inclination of the AWT increases. This is due to the fact that the cosine is maximal for zero, so the normal force will decrease when it travels from left to right, or in opposite direction. During the motion of the AWT, the pipe angle continuously increases, until the motion is reversed for the next sliding path.

The force due to gravity (F_G) and the force due to buoyancy (F_B), are a function of the nodule mass. It is assumed that the mass loss of a nodule during a test, does not influence the magnitude of these forces considerably. Therefore Equation 4.4 can be written as a function of the initial mass of a polymetallic nodule (m_1), given in Equation 4.5.

$$F_N = \left(m_1 - \rho_f \, V_p\right) g \cos(\theta) \tag{4.5}$$

The volume of a nodule, denoted by V_p in Equation 4.5, can calculated using the initial mass and particle density of a nodule. Therefore Equation 4.5 can be rewritten as follows by Equation 4.6.

$$F_N = \left(m_1 - \rho_f \left(\frac{m_1}{\rho_{part}}\right)\right) g \cos(\theta) \tag{4.6}$$

The result of equation Equation 4.6 can be substituted into Equation 4.3, which results into the specific wear rate of polymetallic nodules. Once the specific wear rate is determined, based on different nodules and different sliding lengths, the mass loss of a nodule can be predicted for a predefined distance. First, Equation 4.3 needs to be rewritten in the form of Equation 4.7.

$$m_1 - m_2 = k \, F_N \, s \, \rho_{part} \tag{4.7}$$

In order to plot the normalized remaining mass (m_n) against sliding distance, like Figure 3.11, as presented in the work of Van Laarhoven (2010), Equation 4.7 needs to be dived by the initial nodule mass on

both sides. The normalized remaining mass is defined as the ratio between the nodule mass after an experiment (m_2) and the initial mass (m_1). Using this ratio (Equation 3.3), Equation 4.7 can be rewritten as follows by Equation 4.8.

$$m_n = \frac{m_2}{m_1} \tag{3.3 revisited}$$

$$m_n = 1 - k \left(\frac{F_N}{m_1} \right) s \rho_{part} \tag{4.8}$$

After the determination of the specific wear rate (k), from Equation 4.3, it can be used in Equation 4.8. With Equation 4.8, the remaining mass can be plotted against sliding distance, as can be seen in Figure 4.17.

4.3.3. Experimental Data Processing

In this section the processing of the experimental data will be explained. First, the tracking of a single nodule during an experiment by using a velocity crosscorrelation method in MATLAB is shortly explained. Next, the synchronization of the measurements is shown. The last part of this section provides information about the angle measurement during an experiment.

Nodule Tracking during Experiments

The experiments are filmed with a high speed camera (Velociraptor). As described in subsection 4.3.1 the pipe continuously tilts. In order to film the nodule - and be able to track it - it is chosen to let the camera move along with the motion of the test setup. The camera is connected with steel arms, which results in a moving world around the experimental setup, but a pipe section at standstill, seen from the high speed camera. A picture from the camera connected to the AWT can be seen in Figure 4.4 and a snapshot seen from the high speed camera, can be seen in Figure 4.5.

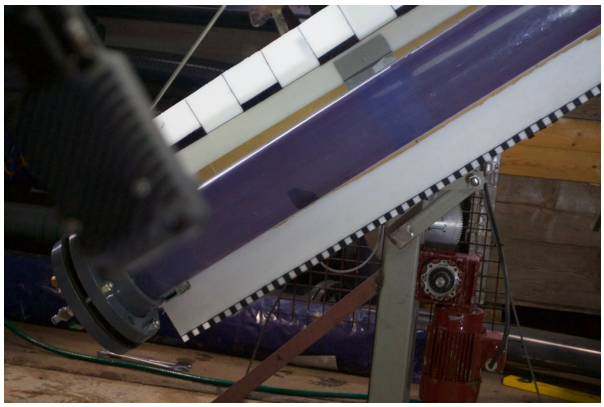

Figure 4.4: The Abrasive Wear Tester with the moving high speed camera, whereas the sliding nodule can be seen, slightly left from the middle of the picture

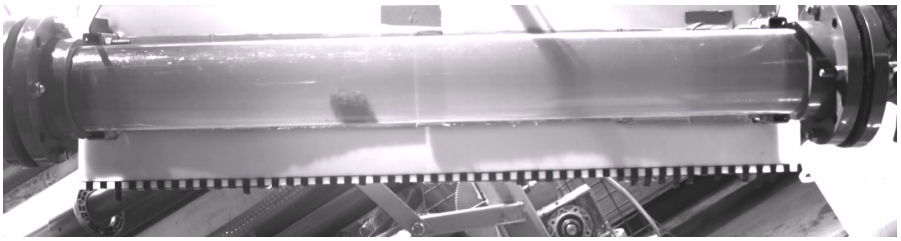

Figure 4.5: Snapshot of a nodule during an experiment, seen from the high speed camera

Next, the result of the video is tracked with a video cross-correlation method using MATLAB, made by De Hoog (2016). The script uses a reference image (in this case the nodule) and searches in each of the consecutive frames the position of this reference image. The strongest correlation between the reference

image and the complete image, is the position of the reference image, the position of the nodule. The shift in reference image can be related to the velocity of the nodule, using the frame rate of the high speed camera and the shift in pixels. An example of the tracking of a nodule during an experiment can be seen in Figure 4.6. The tracking box of the script is represented in this figure with a yellow square.

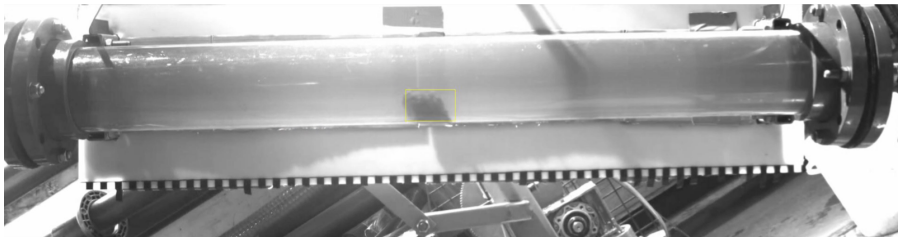

Figure 4.6: Tracking box (represented in yellow) around the polymetallic nodule, using MATLAB

With the use of the MATLAB script, the velocity profiles in both horizontal as vertical direction can be obtained. The nodule should only have a horizontal velocity (u), because of the motion of the camera with the pipe. However, there are often some minor differences seen in the vertical velocity (v). The arms holding the high speed camera are relatively long, wherefore a small vibration and/or movement could cause a small disruption in the video image. The resultant velocity profile of the sliding nodule is obtained as follows by Equation 4.9. An example of a velocity profile can be seen in Figure 4.7.

$$v_{slide} = \sqrt{\left(u^2 + v^2\right)} \tag{4.9}$$

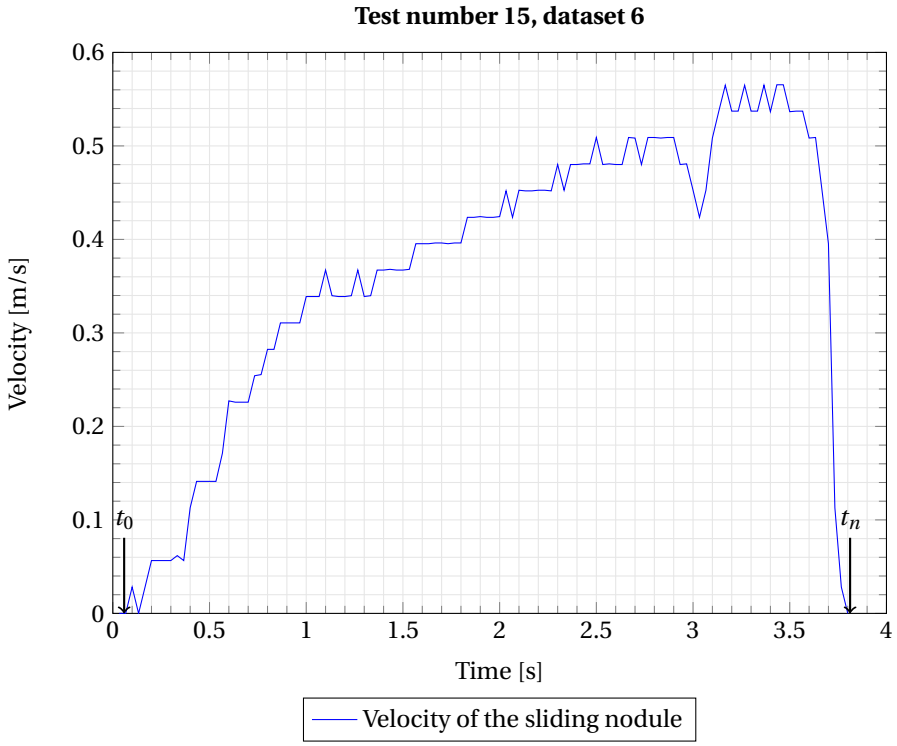

Figure 4.7: Velocity of the sliding nodule, obtained from particle tracking with the high speed camera

In order to check whether this velocity profile is correct, the velocity profile can be integrated over time, which should result in the length of the pipe. The total length of the transparent PVC pipe is 1.50 m (subsection 4.3.1). However, this represents the length including the flanges - spots where the nodule cannot be followed by the script. Therefore the integrated result should be around 1.35 m, the length of the transparent section between the flanges. It is assumed that the peaks and bumps in the velocity profile cancel each other,

the result of the integral would be more or less the same as for a smooth velocity profile. The interval is set from the moment the signal starts (t_0), until the moment that the nodule disappears behind a flange (t_n). The integral which can be used to calculated the sliding distance is given by Equation 4.10. This disappearance is represented in Figure 4.7 with the large derivative in velocity at the right - the latter shall be explained in the following. *If the velocity profile of Figure 4.7 is integrated using Equation 4.10, it results into a distance of 1.38 m.*

$$S_{slide} = \int_{t=t_0}^{t=t_n} v_{slide}\, dt \tag{4.10}$$

Synchronization of the Measurements

At least eight paths of the nodule are tracked and processed using the cross-correlation method. It is assumed that four velocity profiles per side - because the tilting motion results in different velocity profiles, as described in subsection 4.3.1 - are sufficient for obtaining an average velocity profile of the nodule, which is representative for the complete duration of an experiment. The result can be seen in Figure 4.8 and in Figure 4.9. These figures belong to *'Test number 15'*, but each of the other tests resulted into comparable velocity profiles (details of the other tests can be found in Appendix A).

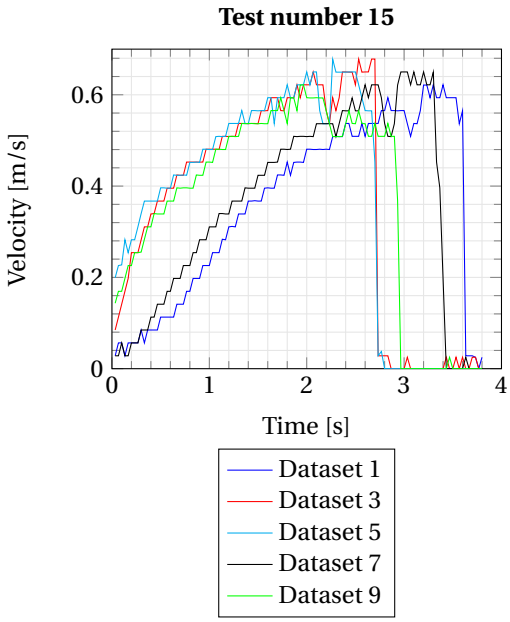

Figure 4.8: Velocity profile of a nodule sliding from left to right

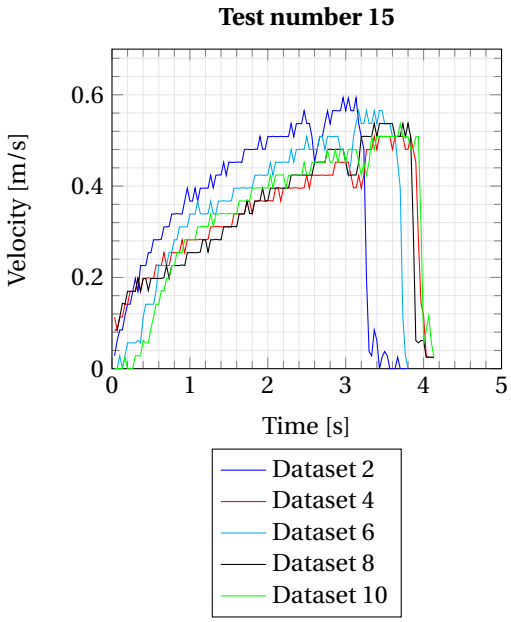

Figure 4.9: Velocity profile of a nodule sliding from right to left

As can be seen from Figure 4.8 and Figure 4.9 the measurements do not start and finish at the same time. This is a result of the start and/or end frame, or the total number of frames. The movement of the nodule is never completely the same. Before an average velocity can be determined, the measurements should be synchronized. From Figure 4.8 and Figure 4.9 it can be seen that each velocity profile has a major difference in its derivative. The large difference in derivative is caused when the nodule 'disappears' behind a flange, in other words: the end of the pipe is reached. The disappearance of the nodule behind the flange and the pausing of the tracking box is shown by Figure 4.10. The synchronization time is therefore defined as follows by Equation 4.11.

$$T_{sync} = t(i) = t\left(\max\left(\frac{d\,v_{slide}}{dt}\right)\right) \tag{4.11}$$

If, for example, five datasets are needed to be synchronized, this results into five different results of T_{sync}, according to Equation 4.11. Next, all the datasets are shifted towards the maximum value of T_{sync}, because then it is made sure no velocity data is lost (negative times are not possible). The results of the synchronization can be seen in Figure 4.11 and Figure 4.12.

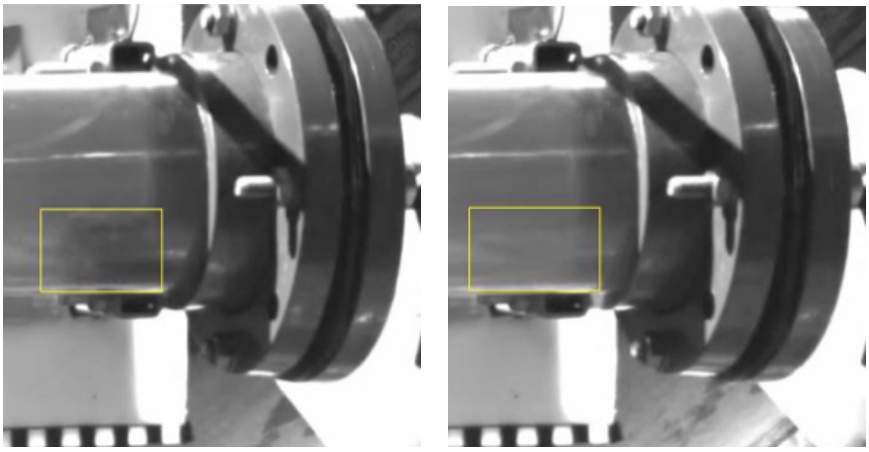

(a) Nodule before the flange (b) Nodule behind the flange

Figure 4.10: Example of the disappearance of a nodule and the reason of the large derivative in the velocity profile

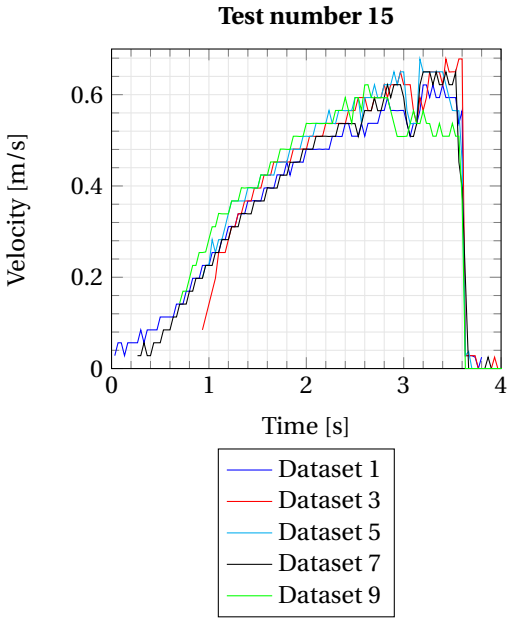

Figure 4.11: Velocity profile of a nodule sliding from left to right

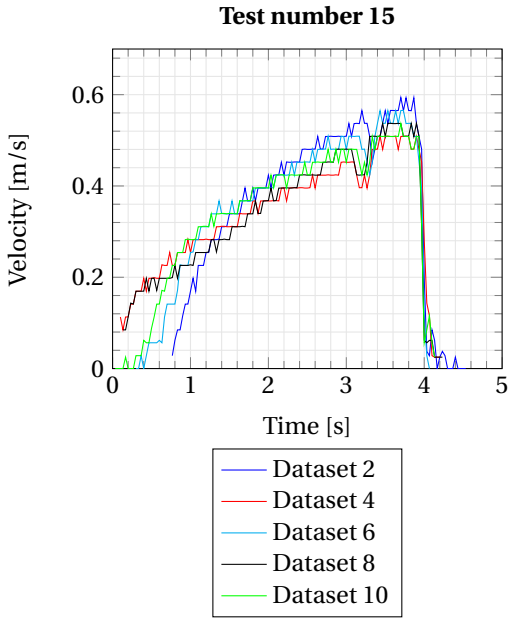

Figure 4.12: Velocity profile of a nodule sliding from right to left

With the velocity profiles synchronized, the average velocity can be determined. However, as can be concluded from Figure 4.11 and Figure 4.12, not every point in time has the same number of velocity profiles ($n_{profiles}$), especially in the starting phase of the nodule. The average velocity is based on the total number of velocity profiles at that moment. This can be represented in formula form as follows by Equation 4.12.

$$v_{avg}(t(i)) = \frac{\sum_{i=1}^{n} v_{slide}(t(i))}{\sum_{i=1}^{n} n_{profiles}(t(i))} \tag{4.12}$$

The average velocity profiles are represented by Figure 4.13. The average velocity is only determined until the first datapoint after the largest derivative, after that the nodule is behind the flange and all velocity differences obtained by the MATLAB script are measurement errors.

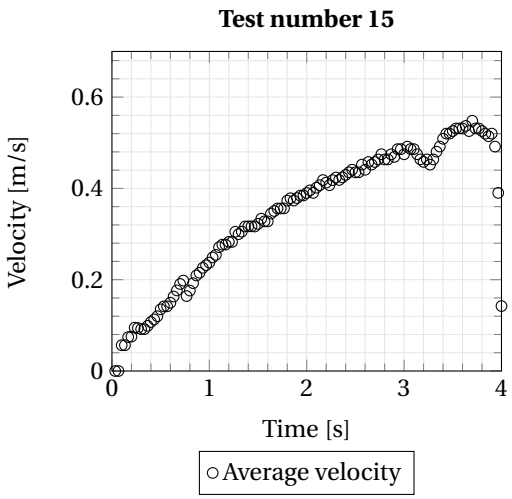

Figure 4.13: Average velocity profile of a nodule sliding from left to right

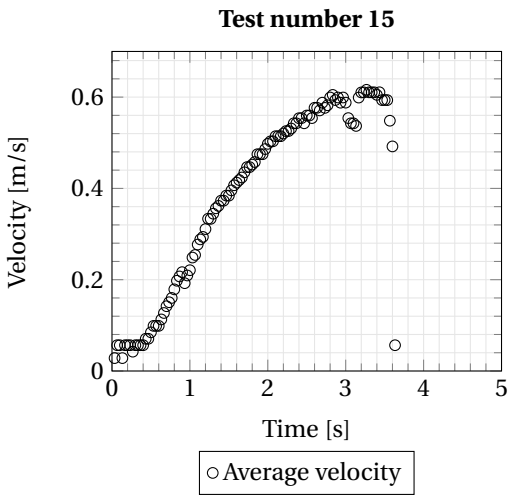

Figure 4.14: Average velocity profile of a nodule sliding from right to left

With the obtained average velocity profile, the pipe angle (θ) can be determined between the start time (t_0) and the end time (t_n) of the sliding motion. As same as for the determination of the average velocity, the pipe angle will also be an average of the number of profiles at that moment in time. More information on the measurement and calculation of the pipe angle can be found in the followup section.

Angle Measurement during Experiments

The pipe angle was continuously measured during each experiment (using a rotary encoder, Table 4.1). Because the total number of steps of the AWT could increase up to 200 for example (which holds a sliding distance of 600 meter), this resulted into a lot of data. However, the nodule does not slide at every measured angle. Especially during the times when the AWT had to lift itself up again from the lowest position. Therefore it is chosen to solve the motion of the experimental setup kinematically. Then, when the start and end position of the nodule are known due to the nodule tracking, the corresponding angles can be calculated. The calculated angles can be compared with the measured angles, which results into a large reduction in data. The kinematic solution of the AWT can be found in Appendix C. The calculated pipe angle plotted against time can be seen in Figure 4.15.

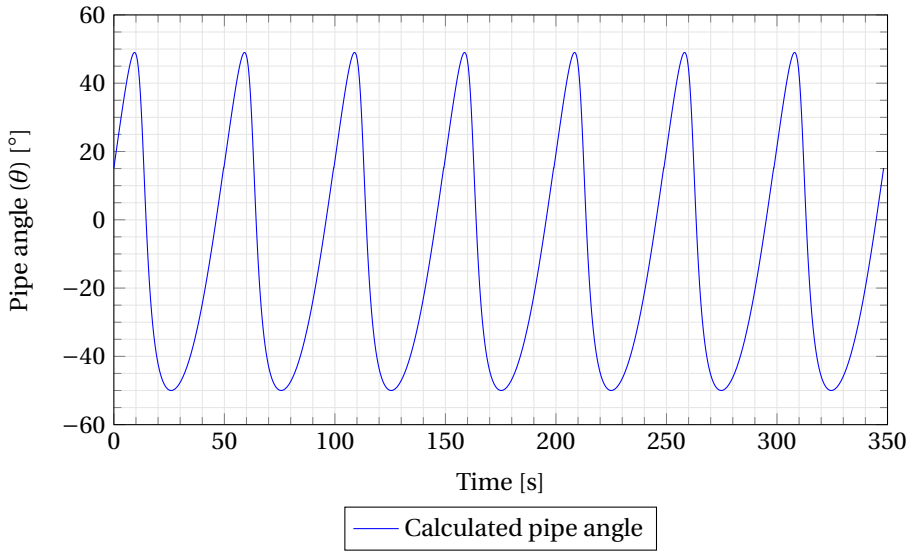

Figure 4.15: The calculated pipe angle plotted against time

In order to fit the calculated angle on the measured angle, two shifts are necessary, a shift in time and a downwards shift. The downwards shift is caused by the fact that the experimental setup has a mass, and in the MATLAB script not. The shift in time is required since the measurement(s) did not start exactly at the same time nor position as the animation. The result of the measured pipe angle versus the calculated angle can be seen in Figure 4.16.

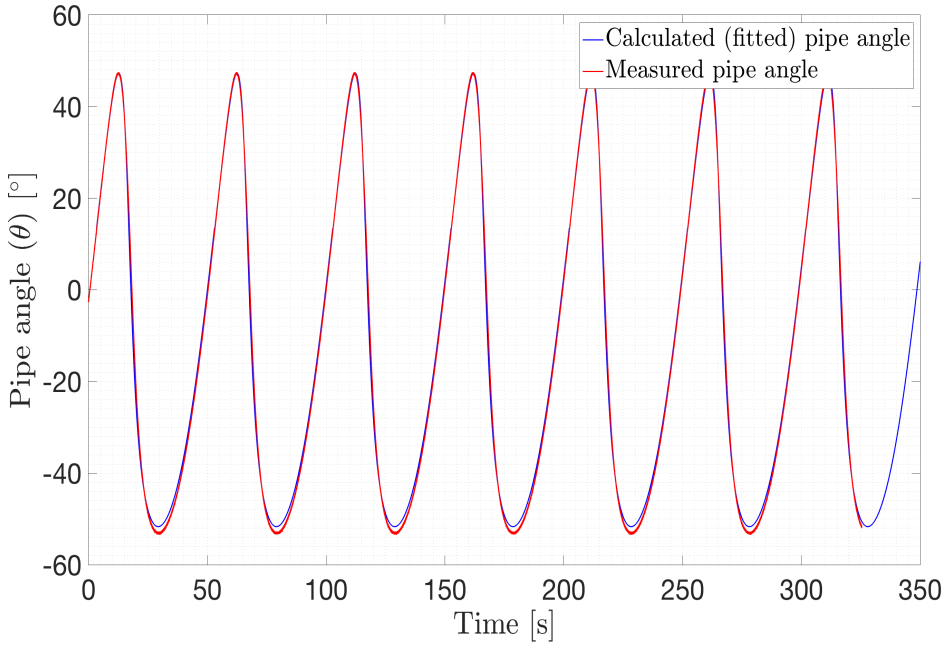

Figure 4.16: Calculated (fitted) pipe angle versus measured pipe angle

With the times of the average sliding velocity profiles (Figure 4.13) the measurement and calculation of the pipe angle can be determined. As can be seen from Figure 4.16, the calculated and measured pipe angle are almost equal. However, not the complete signal is used, only the angles whereas the nodule slides. For '*Test number 15*' for example, the angle range from the left to right motion was -26.96°≤θ≤-47.11° and 18.12°≤θ≤36.24°, for the opposite direction. Substitution this result into Equation 4.4, results into the applied normal force (F_N) during the motions of the AWT, which can be used into the equation of Archard (1953).

Summarized, the experimental data processing holds the following:

- The pipe angle (θ) is required to obtain the normal force (F_N)
- Nodule tracking is required to synchronize the measurements
- The synchronized measurements are used to obtain the pipe angle

4.4. Experimental Results and Discussion

The results of the experiments with single polymetallic nodules are given in subsection 4.4.1. Details concerning the sliding distance and nodule properties, of the tests can be found in Appendix A. In the discussion, in subsection 4.4.2, the outcome of the experimental results and the experimental assumptions (stated in section 4.1), are discussed.

4.4.1. Results - Single Nodule Experiments

As explained in subsection 4.3.2, the nodules are weighted before (m_1) and after (m_2) an test, in order to obtain the normalized remaining mass (m_n), Equation 3.3. The normalized remaining mass is plotted on the y-axis of Figure 4.17, whereas the x-axis corresponds to the sliding distance (s), respectively.

$$m_n = \frac{m_2}{m_1} \tag{3.3 revisited}$$

For each successful test (a test is successful if the nodule did not break into multiple pieces), a material specific wear rate (k) is determined, by using Equation 4.3. Next, an average k-factor is determined over all of the test results, resulting in $k = 4.16{\cdot}10^{-9}$ [m^2/N].

$$k = \frac{m_1 - m_2}{F_N \, s \, \rho_{part}} \tag{4.3 revisited}$$

The equation of Archard (1953) using the obtained k-factor, is plotted in Figure 4.17. In this figure also a ±25% range of the specific wear rate is given. This is done visualize the deviation of the specific test results compared to the obtained average value of k. So, the 'upper'-boundary consists of a value of $k_{up} = 3.12{\cdot}10^{-9}$ [m^2/N], and the 'lower'-boundary has a value of $k_{low} = 5.20{\cdot}10^{-9}$ [m^2/N].

From Figure 4.17 it can be seen that the results of tests 10 and 15 until 17 are not within the ±25% range of the specific wear rate. Tests 1 until 5 were used to find the optimal rotational velocity, in order to secure a sliding behaviour of the nodule. The data of test number 8 was unfortunately lost.

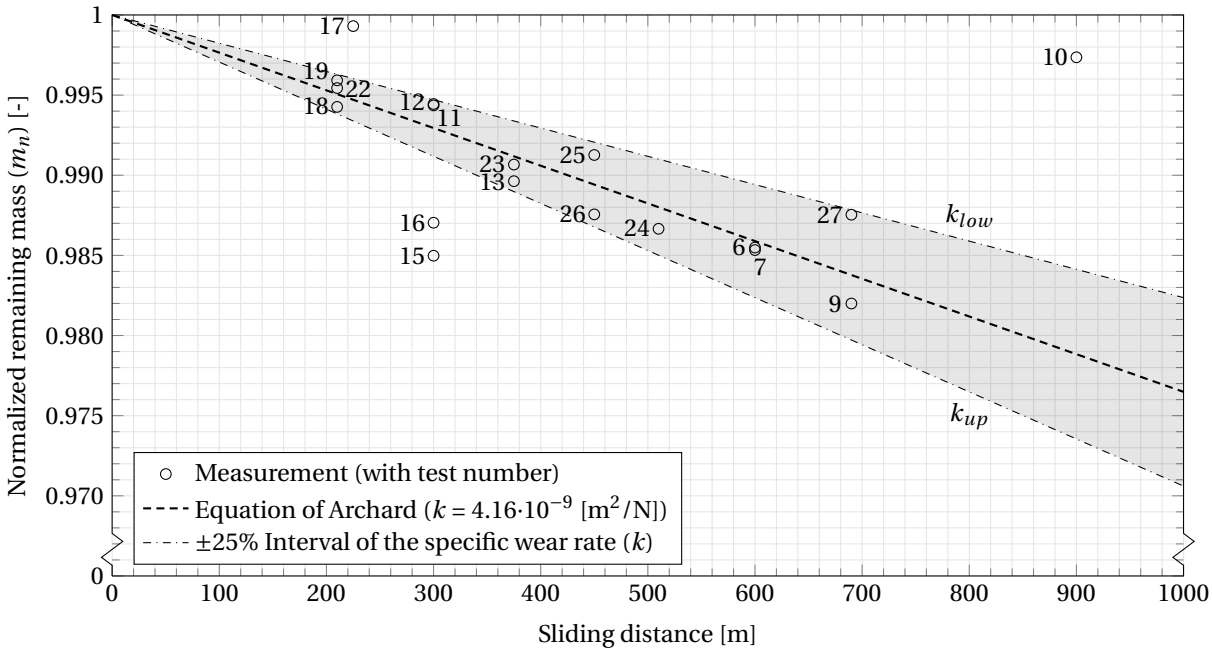

Figure 4.17: Normalized remaining mass plotted against the sliding distance

In order to validate hypothesis 2, first Equation 4.1 is repeated here.

$$V_w = k \, F_N \, s = k \, F_N \int_{t=t_0}^{t=t_n} v_{slide} \, dt \tag{4.1 revisited}$$

From subsection 4.3.3 it is known that t_0 denotes the starting time of the sliding nodule and t_n the ending time. However, this time interval represent only one slide from one side to the other. In order to compare the results from the velocity integral with the total sliding distance, Equation 4.1 needs to be multiplied with the number of slides, since the results of the integral equals the transparent section of the AWT (Equation 4.10). Therefore Equation 4.1 is written in the form as follows by Equation 4.13, in which n_{slide} denotes the total number of slides over the transparent section of the AWT.

$$V_w = k \, F_N \left(\int_{t=t_0}^{t=t_n} v_{slide} \, dt \right) n_{slide} \tag{4.13}$$

The other parameters, as the worn volume (V_w), the applied normal force (F_N) and particle density (ρ_{part}), are the same as used in Equation 4.3. The specific wear rate is now determined as follows by Equation 4.14.

$$k = \frac{m_1 - m_2}{F_N \, \rho_{part} \left(\int_{t=t_0}^{t=t_n} v_{slide} \, dt \right) n_{slide}} \tag{4.14}$$

The results of Equation 4.14 are plotted in Figure 4.18. Also, the results from Equation 4.3 are plotted to see the (minor) differences. Values of the specific wear rates determined with both equations, are obtained in Table A.6.

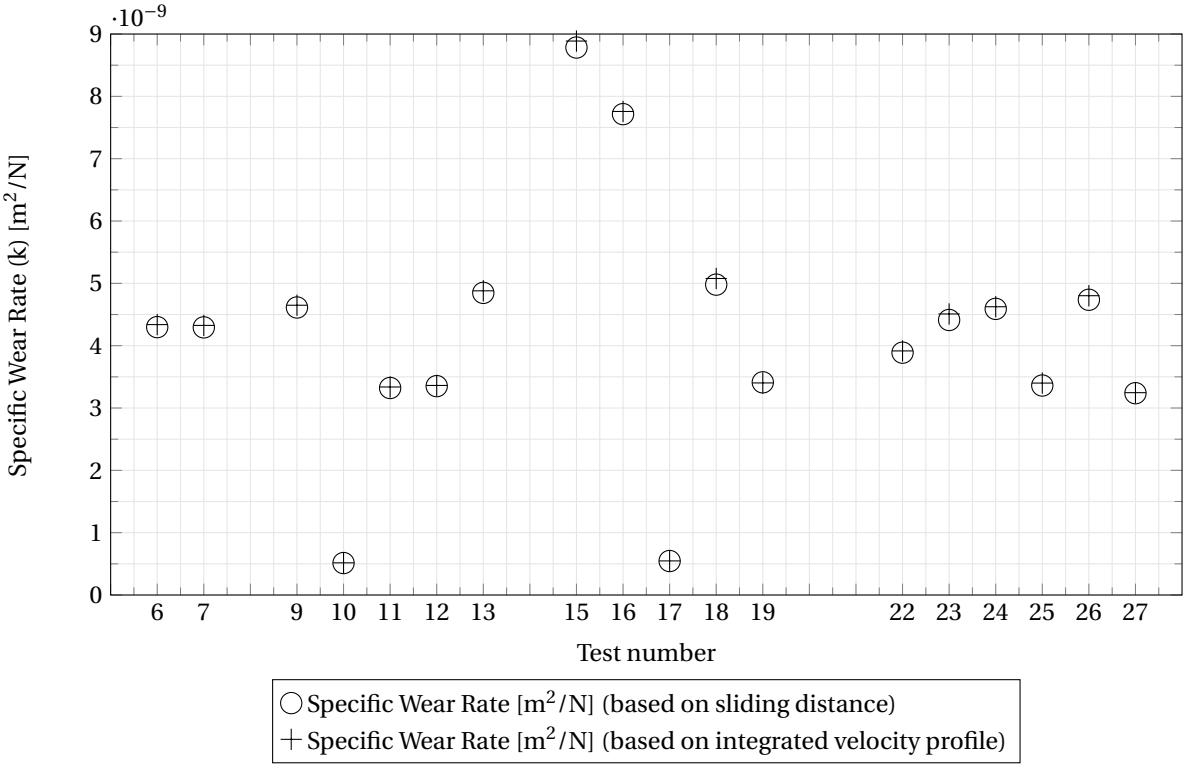

Figure 4.18: Specific wear rate based on sliding distance compared to specific wear rate based on integrated velocity profile per test

4.4.2. Discussion

Discussion on the Experimental Assumptions

First the experimental assumptions from section 4.1 are repeated and discussed.

1. It is assumed that the particle density, ρ_{part}, remains constant during a test run (subsection 4.3.2).

   Abrasive wear causes rounding of particles, as seen in the work of for example Vlasák et al. (2015) (graded basalt pebbles, Figure 3.14). The rounding of the particles is accompanied by a volume reduction of the particles. However, this rounding will also cause a decrease in weight per single particle. Since the density of a particle is determined by the ratio between the weight and volume, both decreases will not strongly effect the particle density. Especially not in mass losses due to abrasive wear, since this is for some sliding distances less than two percent of the initial nodule weight (as can be seen in Figure 4.17).

2. The mass loss of a nodule during a test, does not influence the applied normal force, F_N, considerably (subsection 4.3.2).

   From Figure 4.17 it can be seen that the nodule decreases one percent in mass (for a sliding distance of 400 meter) for example. If the initial mass of a nodule is 400 g, this will result in a normal force of (with a pipe angle of $\theta = 0°$), $F_N = 1.62$ N (Equation 4.6). After sliding 400 meter, the nodule mass decreased by one percent, which results into an applied normal force of 1.60 N, at the end of the test run. Thus, the normal force decreases during the test run with 0.02 N. Although there is a decrease in normal force, this will not be noticed in the result for the specific wear rate. Since the order of this rate is 10^{-9}, it will not matter if the decrease in normal force is taken into account.

Discussion on the Experimental Setup

The advantage of the Abrasive Wear Tester (AWT) above other setups, as described in subsection 3.3.1, is the exclusion of other wear mechanisms. A pump is not present in the setup, so there is no impact wear by pumps during a test run. No bends are used, which holds that the impact wear due to bending pipe sections is also prevented. Large distances can be covered by the AWT, since the motion is repeatable, as seen from the velocity profiles, which were equal to each other.

The disadvantage of the AWT is that the fluid is quiescent in the pipe instead of flowing. In this setup the nodule is in continuous contact with the wall, what might be not the case if there is a flow which drives the movement of a particle. Also, the normal force acting on the nodule is driven by gravity and buoyancy, whereas in the VTS the normal force will be a result of the hydrodynamic drag force.

Discussion on the Experimental Results

It should be noted that the specific wear rate is valid for this batch of nodules, Figure 2.13 and this experimental setup (the Abrasive Wear Tester), Figure 4.2. Using other setups could result into a different specific wear rate due to the presence of pumps for example. From chapter 2, it is known that there is a wide variety of polymetallic nodules, which could also lead to a different specific wear rate.

Comparing the obtained results for the specific wear rate, $k = 4.16{\cdot}10^{-9}$ [m^2/N] and the specific wear rates given by Table 3.1, it can be concluded that the obtained value is not in one of the wearing classes. This holds that the nodules wear faster.

From Figure 4.18, it can be seen that it does not matter if the sliding distance or integrated velocity profile is substituted into the equation of Archard (1953), for the determination of the specific wear rate.

4.5. Conclusions and Recommendations

The following secondary research questions were formed at the beginning of this chapter:

- *Is the equation of Archard applicable for polymetallic nodule degradation due to abrasive wear?*
- *Does the sliding velocity influence the degradation due to abrasive wear?*

4.5.1. Hypotheses

The following hypotheses have been formed in subsection 4.2.1.

- *Hypothesis 1:*

  The abrasive wear equation of Archard is valid for polymetallic nodule degradation due to abrasive wear; there is a linear relation between the worn volume and sliding distance.

  The first hypothesis has been validated. The obtained material specific wear rate of $k = 4.16{\cdot}10^{-9}$ [m^2/N], gives a good prediction of the linear degradation behaviour due to abrasive wear. The result is plotted in Figure 4.17. As is given in subsection 4.4.2, the results are based on the used experimental setup (AWT) and the available batch of polymetallic nodules from the Clarion-Clipperton Zone (CCZ) (Figure 2.13).

- *Hypothesis 2:*

  Abrasive wear can be written as a function of sliding distance, but also as a function of sliding velocity, integrated over (sliding) time.

  The second hypothesis has been validated. The influence of sliding velocity on the material specific wear rate (k) has been tested. There were some minor deviations in some of the tests, as shown in Figure 4.18, however, on the scale of the specific wear rate, the differences are negligible.

4.5.2. Conclusions

Is the equation of Archard applicable for polymetallic nodule degradation due to abrasive wear?

The variety of nodules causes a deviation in the specific wear rate (k). But with an average k experimentally determined, the equation of Archard (1953) can be used for single polymetallic nodule degradation caused by abrasive wear. From Figure 4.17 the linear degradation behaviour can be seen.

Does the sliding velocity influence the degradation due to abrasive wear?

Although the nodules had different sliding velocities during the experiments, from the results of subsection 4.4.1 (Figure 4.18) it is clear that both approaches can be used. Therefore both the integrated velocity profile, times the number of slidings, or the total sliding length can be used in the equation of Archard (1953). However, it must be stated that the sliding velocity of the nodule originates from movement of the Abrasive Wear Tester and not by a flow.

4.5.3. Recommendations

Polymetallic Nodule related Recommendations

During the experiments the nodule should not break, because if the nodule breaks, particle-particle interaction causes more degradation compared to degradation due to abrasive wear.

The video cross-correlation script, made by De Hoog (2016), proved to be an outstanding method to obtain velocity data. In this case it was used to track the sliding velocity of the polymetallic nodules, however, for many other slurry related problems this script could be used.

Different sliding lengths with different nodules are tested inside the AWT. Each rotation of the pipe, equivalent to three meters of sliding, took approximately 55 seconds. A test run whereas 600 meter sliding distance was desired, took therefore roughly 3 hours. All that time the nodule is inside the water. Therefore, it must made sure that saturated polymetallic nodules are used. Otherwise not only the initial weight of the nodule (m_1) is incorrect, but also the weight after the test (m_2) run is not correct. Which will lead to a different (wrong) specific wear rate (k).

Experimental Setup related Recommendations

The Abrasive Wear Tester (AWT) was designed to test the effect of abrasive wear on polymetallic nodules. Influences of impact wear due to the presence of a pump or bends are prevented. In order to extent the research on particle degradation by abrasive wear in a vertical transport system, it is recommended to exclude the influences of other wear mechanisms. A proposal for an experimental setup would be a setup which contains a vertical pipe section, whereas the nodules would be only present in this section and will not circulate around, like a fluidization experiment. Using single - or batches of - nodules and sieving them on a specific size, like the work of Van Laarhoven (2010), whereas particles are used of a diameter only greater than 1.4 mm, only then representative for polymetallic nodules. After the experiment the batch is sieved and in the result it should be seen how particle-wall interaction and particle-particle interaction changes the PSD curve. It is also recommended to research the influence of a flow on the effect of abrasive wear.

5

Scale Model Experiments II - Degradation of a Batch of Polymetallic Nodules

The first set of experiments was focussed on the degradation due to abrasion of a single nodule (chapter 4). This set of experiments is focussed on the degradation due to abrasion of a batch polymetallic nodules. During experiments in Freiberg, conducted by IHC MTI (for the Blue Mining project), degradation tests were performed using polymetallic nodules from the Clarion-Clipperton Zone (CCZ). In Kinderdijk the Freiberg nodule degradation experiment is mimicked in the Abrasive Wear Tester (AWT), to check whether it gives a representative result. After the experiments, the influence of particle-particle interaction should be seen. Especially when the test results are compared to the results of chapter 4. This chapter describes the second set of experiments and provides an answer to two secondary research questions.

Secondary research questions of this chapter:

- *Is the equation of Archard applicable to quantify the degradation due to abrasion for a batch of nodules?*
- *Until what extent does polymetallic nodule degradation propagate?*

This chapter starts with section 5.1, which provides information about the large scale slurry transport tests in an abandoned mine shaft in Freiberg, Germany. In section 5.2, theory of the degradation experiments in Freiberg is given, whereas in subsection 5.2.1 hypotheses are given, based on the secondary research questions of this chapter. In the following, in section 5.3, the experimental plan and experimental data processing are discussed. The experimental setup used for the batch experiments is the Abrasive Wear Tester (AWT), which is described in section 4.2 (Figure 4.2). Details of the batch used for these experiments can be found in subsection 5.3.1. The results of the experiments are given in section 5.4. In this section also a comparison is made between the degradation of a batch and single nodule degradation (subsection 5.4.2). It compares the degradation results of a batch with the equation of Archard (1953); whereas the specific wear rate (k) for nodules is based on the experimental results of section 4.4. Before an answer to the secondary research questions, conclusions and recommendations are given in section 5.5, a discussion is provided about the obtained results, in subsection 5.4.4. Furthermore, in Appendix A, sieve data from the experiments is provided.

5.1. Introduction - Freiberg Testing Trials

In order to develop a vertical hydraulic transport system (VTS) which spans a length of 5000 meters, a logical step is to start with laboratory scale experiments. The Blue Mining project took the laboratory experiments to an abandoned mineshaft, in Freiberg, Germany[1]. Tests were done with sand, coarse gravel and polymetallic nodules from the Clarion-Clipperton Zone (CCZ). The test setup is used for the validation of mathematical flow models, which are related to friction losses and slurry transport velocities (Dasselaar et al., 2018b). Also, the occurrence of density waves during vertical transport was investigated.

A vertical riser is placed in an abandoned mineshaft, with a total length of 127 meters, which makes it one of the largest vertical hydraulic transport systems in Europe (Dasselaar et al., 2018a). In Figure 5.1 a section of the vertical riser can be seen. Further, the setup consisted of a centrifugal pump, a vertical pipe downwards and an U-bend with a dump valve. Above the ground hoppers were used in order to add sediments to the flow loop. During the testing trials it was possible to remove fine sediments from the loop (Dasselaar et al., 2018b).

The test runs with polymetallic nodules from the CCZ showed degradation behaviour (Dasselaar et al., 2018b). The Freiberg testing was done with pre-crushed nodules, therefore it is assumed that particle degradation is dominated by abrasive wear. Even if impact wear is present during these tests - with relative small nodules, the particle strength of smaller nodules is much larger than for bigger nodules, which was one of the conclusion from the work of Dreiseitl (2017).

Results showed that nodule degradation is quite severe after twelve pump passages (Dasselaar et al., 2018b). In the proposed prototype of the VTS six booster stations are present, consisting of two centrifugal pumps each. In total the VTS contains thirteen pumps. In order to obtain more insight in the effect of abrasive wear on a batch of polymetallic nodules, it is chosen to mimic the Freiberg test in the Abrasive Wear Tester (AWT), the experimental setup used for the single nodule experiments, shown in Figure 4.2.

Figure 5.1: Picture of the Blue Mining test facility in Freiberg, Germany

5.2. Theory - Polymetallic Nodule Degradation of a Batch

In Freiberg, two types of experiments with polymetallic nodules are performed, first with polymetallic nodule sizes between 8-16 mm. The second experiment was assigned to degradation, in which nodule sizes between 16-30 mm are used. The volumetric concentration during the tests with polymetallic nodules was 5% (Dasselaar et al., 2018b).

The tests were performed using pre-crushed manganese nodules, so it is expected that abrasive wear will prevail the degradation behaviour (Dasselaar et al., 2018b). The same phenomena should be seen as Vlasák et al. (2015), rounding of the particles which causes a production of fines. In his work the d_{50} changed slightly, after the test run the obtained d_{50} was 94% of its original value and a production was seen of particles smaller than 10 mm. The graded basalt pebbles are shown in Figure 3.14.

[1] www.bluemining.eu

The Particle Size Distribution (PSD), before and after a test run in the test facility in Freiberg, is given in Figure 5.2. It can be seen that the d_{50}, which denotes the mass-median diameter, decreased very little (from 11.40 to 11.30 mm), and the cumulative mass percentage of smaller particle sizes does increase. In Table A.7, the PSD data of the Freiberg test with polymetallic nodules can be found.

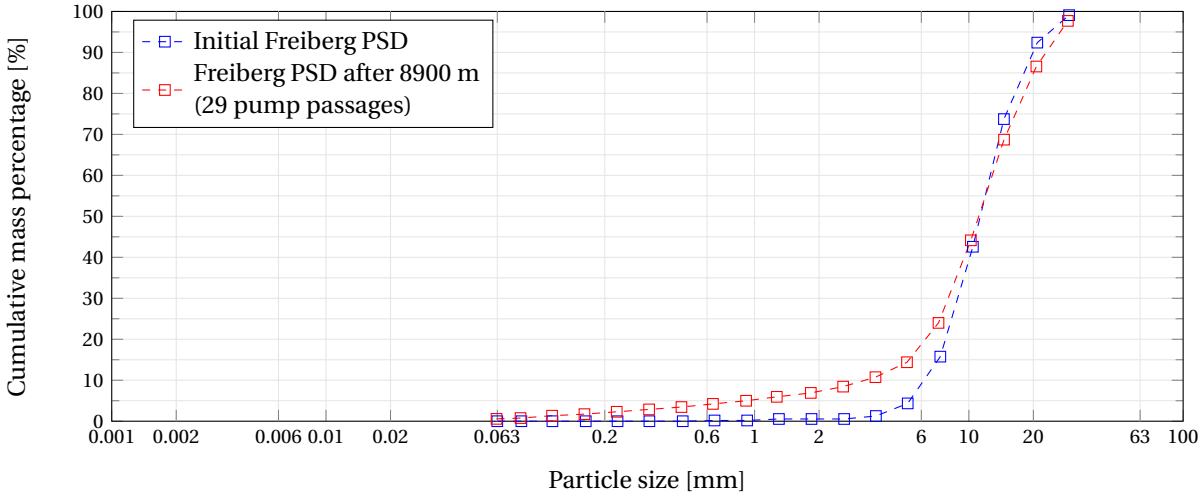

Figure 5.2: PSD curve of polymetallic nodules from the CCZ used in the Freiberg testing trials (De Hoog, 2018)

In order to quantify the degradation of a batch of nodules due to abrasive wear, the equation of Archard (1953) is used, in which the specific wear rate (k), based on the single nodule experiments, subsection 4.4.1, is substituted. In the single nodule experiments this equation was used to determine the worn volume, or remaining mass of the nodule, after a test run. But the question arises how to define the normalized remaining mass (m_n) or worn volume (V_w) of a batch of nodules. First, in order to calculate the normalized remaining mass, Equation 4.8 is revisited here.

$$m_n = 1 - k \left(\frac{F_N}{m_1} \right) s \, \rho_{part} \tag{4.8 revisited}$$

As can be seen from Figure 5.2, a production of fines is clearly seen in particle sizes ranging from 0.063-5 mm. If a particle size of 1.4 mm is considered, it can be concluded from Figure 5.2, that the cumulative increase is around 6%. This holds that 6% of the batch of nodules contains material which is ≤1.4 mm, after the test run. Initially, the cumulative percentage of particles ≤1.4 mm was 0%.

The creation of fines during the test run resulted into a cumulative mass percentage increase of 6%. As explained in subsection 4.3.2, the normalized remaining mass (m_n) is defined as the ratio between the nodule mass after an experiment (m_2) and the initial mass (m_1). The normalized remaining mass has an initial value of 1, and decreases linearly (as can be seen in Figure 4.17).

In this set of experiments a batch of nodules is used. Therefore, the initial mass is taken as the initial mass of the batch. The mass after an experiment is taken as the mass of the batch with equal particle sizes, compared to the initial batch. This would hold for the Freiberg batch, after the test run, that the particles which are ≤1.4 mm, are not taken into account. The amount of the particles ≤1.4 mm, are shown as an increase in cumulative mass percentage (CMP) in the PSD, and this amount should be, together with the value of the normalized remaining mass, equal to 100%. In other words, the decrease in remaining mass equals the increase in cumulative mass percentage, which is represented by Equation 5.1. In Equation 5.1, CMP denotes the cumulative mass percentage, in [%] and m_n the normalized remaining mass, also denoted in [%].

$$CMP = 100 - m_n \tag{5.1}$$

Experimental Assumptions

The assumptions used for the experiments are listed below. After each assumption there is referred to the specific (sub)section where it is used and/or clarified.

1. It is assumed that the particle density, ρ_{part}, remains constant during a test run (subsection 4.3.2).

5.2.1. Hypotheses

The following hypotheses are formed based on the secondary research questions given in this chapter:

- *Hypothesis 1:*

  The equation of Archard can be used to predict the degradation due to abrasive wear for a batch of polymetallic nodules.

  The results of section 4.4 gave a specific wear rate (k) for polymetallic nodules. Experiments were performed using single nodules, which holds that there is no effect of degradation due to particle-particle interaction. Because the nodules are pre-crushed and therefore less susceptible for impact wear caused by particle-particle interaction, the degradation effect due to abrasive wear could prevail the degradation behaviour, and therefore the equation of Archard (1953) can be used.

- *Hypothesis 2:*

  Particle degradation causes a production of fines until a size class which no longer degrades.

  With the rounding of particles, like is seen from Vlasák et al. (2015), fine material is produced. In the work of Van Laarhoven (2010) the effect of abrasive wear is tested on relatively small particles (compared to polymetallic nodules). The effect of abrasive wear can be seen as gentle polishing of particles (Van Laarhoven, 2010). Therefore, it is not likely that the very fine factions (e.g. particle sizes smaller than 63 μm), which are rounded and contain (almost) none angularities, will still produce finer material.

A validation or falsification of these hypotheses can be found in subsection 5.5.1.

5.3. Experiments - Polymetallic Nodule Degradation of a Batch

In order to mimic the degradation experiments from Freiberg, the batch of polymetallic nodules is recreated in the MTI laboratory in Kinderdijk. The experimental setup, the Abrasive Wear Tester (AWT), which is used for these batch experiments, is described in subsection 4.3.1. The experimental plan can be found in subsection 5.3.1. Information of the data processing after the batch experiments can be found in subsection 5.3.2.

5.3.1. Experimental Plan

The total testing length of the Freiberg testing trials equals 8900 meter (Dasselaar et al., 2018b). In order to test a distance of 8900 meter with the AWT, it is decided to split the test into two parts. First, a distance of 4500 meter is tested, whereafter the experimental setup is completely emptied and the batch is sieved. The test of the first 4500 meter is referred to as '*Test 1*'. The test of the second 4500 meter is referred to as '*Test 2*'.

The AWT is emptied after *Test 1*, halfway of the total testing length of the Freiberg tests. The complete slurry is collected in buckets for fine particle collection. A sieving analysis is done on the wet batch, whereas the smallest sieve has a size of 2.8 mm (the sieving analysis can be seen in Figure 2.14). The particles which were collected underneath this sieve went into the furnace to dry (at a temperature of 105°C, to evaporate the water). Caution is required, the fines cannot dry too quickly in the furnace, it would cause plaques. Therefore, the fines are first rested at room temperature, whereafter they are placed in the furnace in steps. By each step the period in the furnace increases. After the drying these particles were sieved in a sieving tower with sieve sizes ranging from 0.038-2 mm. The drying of the fine material takes a lot effort and therefore they do not re-enter the AWT for *Test 2*. After *Test 2*, with its own production of fines, the fines will be summed with the fines of *Test 1*.

First, the PSD which is used in the Freiberg degradation test is recreated at the MTI laboratory with the Kinderdijk nodules. During the Freiberg degradation test, there is worked with pre-crushed nodules (Dasselaar et al., 2018b). In order to recreate the Freiberg batch, nodules from the bigger size classes needed to be crushed, since the batch available for this Master Thesis contains very large nodules (Figure 2.15). The crushing is done using a hammer. A picture of the initial, crushed, batch of polymetallic nodules can be seen in Figure 5.3. The PSD curve from both the Kinderdijk as the Freiberg batch, can be seen in Figure 5.4. The PSD data from both batches, is given in Table A.9.

Figure 5.3: Picture of the initial (crushed) batch of the Kinderdijk nodules

The initial batch of nodules, before *Test 1*, is shown in Figure 5.3. The initial batch looks to consists of dry nodules in this picture, however, this was a result of the crushing, since a lot of sediment appeared from the inside of the nodules. This batch is made (almost) identical to the initial batch of the Freiberg experiments, as can be seen in Figure 5.4. The deviation between the particle sizes of 2-6 mm was the result of not using the same sieves. The d_{50} of the Kinderdijk PSD (12.36 mm) is slightly higher than the Freiberg PSD (11.40 mm).

Abrasion will produce fines from the larger particle sizes, which are then redistributed into the smaller particle sizes (Vlasák et al., 2015). An increase in cumulative mass percentage of the smaller sizes should be witnessed. Especially, in the smaller size classes which did not contain material initially. As can be seen from Figure 5.4, both the initial Kinderdijk PSD as the initial Freiberg PSD, contain no particles ≤1.4 mm. Therefore, the total production of fines is measured from this size class.

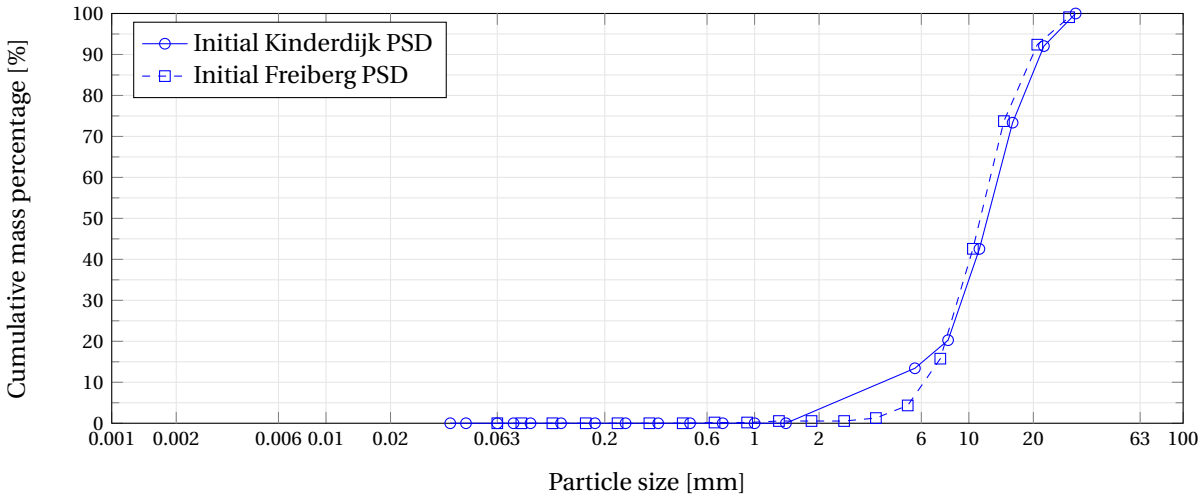

Figure 5.4: Initial PSD curve from abrasive wear experiments compared with the initial PSD curve used in Freiberg

It is known from the work of Zenhorst (2016) that impact wear causes a large reduction in the d_{50} of a distribution. One of the conclusions of Vlasák et al. (2015) was that angular particles are rounded due to abrasion and which holds a production of fines. Considering these two conclusions, it is expected that abrasive wear does not change the d_{50} sufficiently, and that, due to the rounding of the particles, fine particles are produced. A production of fines causes an increase in cumulative mass percentage from the smaller particle sizes, which were initially not present in the Particle Size Distribution (PSD). In subsection 3.3.1, it is stated that fines not only greatly increase the dewatering and drying costs, but fines could also result in a higher viscosity of the transportation medium (Van den Berg and Alvarez Grima, 2006; Worster and Denny, 1955). Van den Berg and Alvarez Grima (2006) stated that the dewatering costs of 6 mm fine coal are almost 10 times as those of the particles greater than 6 mm.

5.3.2. Experimental Data Processing

After *Test 1*, and also after *Test 2*, the AWT tester is emptied and the batch is collected. In the first place, this collection mainly contains the larger sized particles. At the front page of this Master Thesis the inside of the AWT is shown after *Test 1*, also represented by Figure 5.12. It can be seen that a lot of fines cover the bottom of the pipe. The pipe can easily be cleaned using a water hose and the fines are collected in a bucket.

The bottom of the pipe is not the only place were fines are present after a test. Part of the fines is suspended in the water, as can be seen in Figure 5.10, due to its dark color. Therefore it is chosen to collect all of the water after a test and let it rest in buckets for at least a week. With a settling velocity calculation, from the work of for example Ferguson and Church (2004), it could be calculated that in 13 hours particles with a diameter of 38 μm have settled. Therefore a week at rest is more than sufficient. The water is sucked out of the buckets and the fines are collected. These fines are also going into the furnace and are sieved afterwards. As denoted in subsection 5.3.1, caution is required when placing the fines in the furnace. A picture of a part of the slurry collected in buckets can be seen in Figure 5.13.

Together with the sieving data from the bigger nodules (particles greater than 2.8 mm) a PSD curve can be made. However, the bigger nodules were sieved directly after the test inside the AWT and were still wet. Therefore, the nodule sizes which are at least 2.8 mm, need to be recalculated to a dry weight. This is done by Equation 5.2, using the obtained densities (ρ_{part} = 1700 kg/m^3 and ρ_s = 2500 kg/m^3) from subsection 2.3.4. In Equation 5.2, m_d represents the dry weight, m_w represents the wet weight of the nodules remaining on a specific sieve. In Figure 5.5 an example of wet nodules on a sieve can be seen and in Figure 5.6 dried, unsieved fines can be seen.

$$m_d = m_w \left(\frac{\rho_{part}}{\rho_s} \right) \tag{5.2}$$

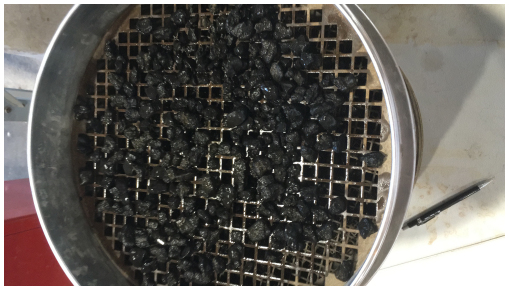

Figure 5.5: Picture of wet nodules on a sieve after *Test 1*

Figure 5.6: Fines remaining after *Test 1* and dried in the furnace

The large fractions can be weighted on a normal weigh scale, but when the particle size reduces the weight might be out of the measurement range of the scale. To measure the weight of the fine particles, an analytical balance is used. These balances can measure up to one-thousandth of a gram accurate. An example of fines on the analytical balance can be seen in Figure 5.7 and Figure 5.8.

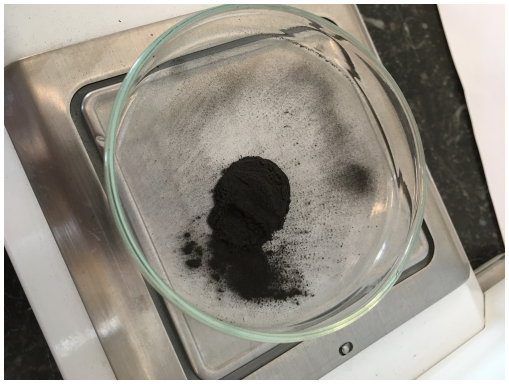

Figure 5.7: Sieved fines on the analytical balance at the MTI laboratory (45 μm)

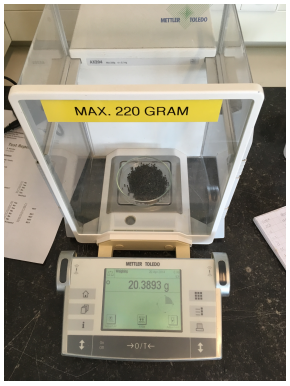

Figure 5.8: Analytical balance at the MTI laboratory

5.4. Experimental Results and Discussion

In this section the experimental results are given and it also provides a discussion of its outcome. The results presented in this section are separated into three different subsections. The first subsection, subsection 5.4.1, gives the results of the batch experiments in the Abrasive Wear Tester (Figure 4.2), using the Kinderdijk nodules (Figure 2.13). The followup subsection, subsection 5.4.2, compares the batch degradation with the results of the single nodule degradation experiments, from subsection 4.4.1. This is followed by subsection 5.4.3, where the results of the batch tested in the MTI laboratory are compared to the test results of the Freiberg testing trials. The final subsection of this section, subsection 5.4.4, provides a discussion about the obtained results.

5.4.1. Results I - Batch Properties of the Kinderdijk Nodules

Snapshots directly after the start of the experiment can be seen in Figure 5.9. Only after a few rotations of the test, the water become very dark all of a sudden, which can be seen in Figure 5.10. This was also one of the observations during the Freiberg testing trials according to Dasselaar et al. (2018b). It was therefore not possible to track the batch, as done for the single nodule degradation experiments (subsection 4.3.3). The slurry became so dark, that only by listening the sliding of the batch could be noticed. As can be seen in Figure 5.10, the water turned very dark. It even looked as if a black pipe had been used to make the experimental setup instead of a transparent PVC pipe (Figure 4.2).

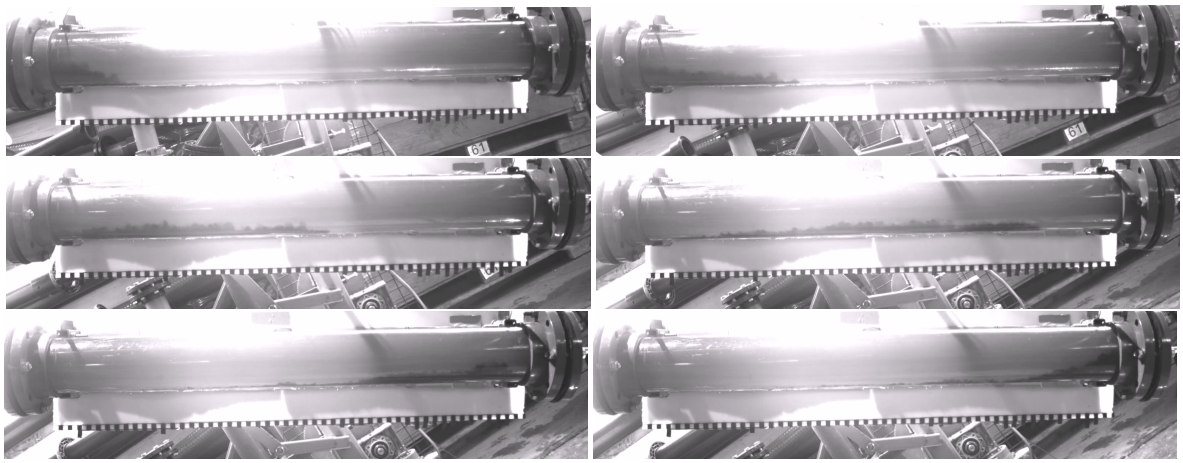

Figure 5.9: Snapshots during the abrasive wear experiments with the initial Kinderdijk batch of nodules (just after the start of *Test 1*)

Figure 5.10: Dark water after a few rotations of the batch in the Abrasive Wear Tester

Figure 5.11: Kinderdijk batch after *Test 1* and before *Test 2*

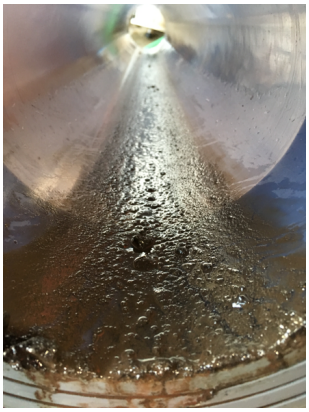

Figure 5.12: Picture of the inside of the Abrasive Wear Tester after *Test 1*

Figure 5.13: Picture of a part of the slurry from the Abrasive Wear Tester after *Test 1*

The sieved batch after *Test 1*, containing only particles greater than 2.8 mm, is shown in Figure 5.11. As stated in subsection 5.3.1, this batch is used for the remaining 4500 m, *Test 2*. The PSD curve after *Test 1* is given in Figure 5.14, which also contains the sieving of the fines. The collection of the slurry in buckets in shown in Figure 5.13. The fines produced during *Test 1* is indicated with a light grey color in Figure 5.14. Because initial there were no particles ≤1.4 mm present in the batch. Fines remaining in the Abrasive Wear Tester after the 4500 m test, can be seen in figure 5.12. The increase in cumulative percentage of the size classes ≤1.4 mm, equals 20.31%.

Remarkably, after the sieving of the fine fractions, it appeared that the fraction that remained on the 45 micron sieve was heavier than the fraction on the 63 micron sieve. This could be related to the clay content inside or on the nodules (Marchig and Halbach, 1982). In total, the cumulative percentage of the fraction ≤63 μm is 0.36%. The complete dataset of the sieving analysis can be found in Table A.10.

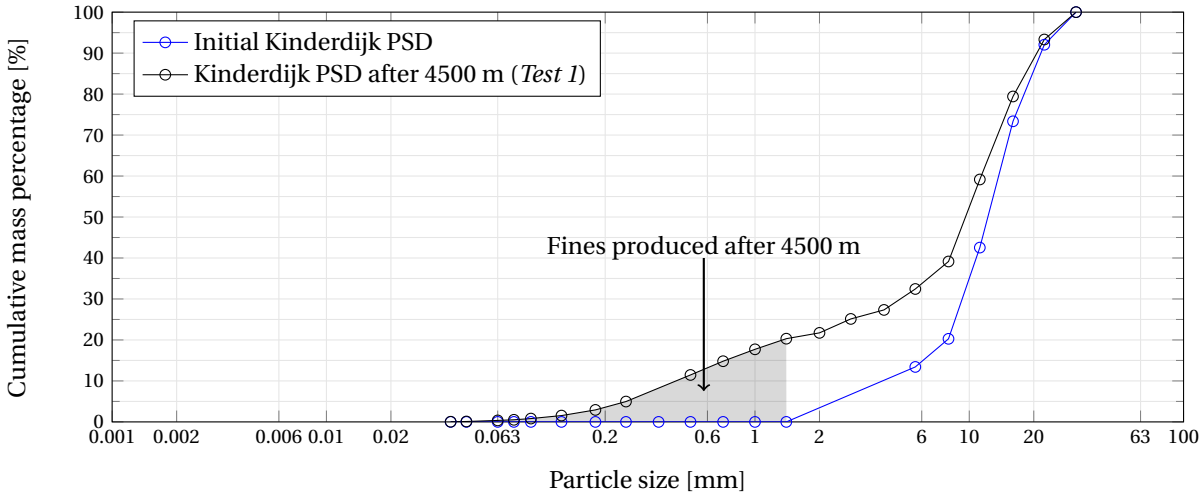

Figure 5.14: PSD curve from abrasive wear experiments after a testing length of 4500 meters (*Test 1*)

From Table A.11 a relatively large decrease in d_{50} can be seen (from 12.36 mm to 9.74 mm), compared to Vlasák et al. (2015) for example, whereas the d_{50} was 94% of its initial value after the test. This implies that the wear mechanism acting during this experiments was not purely abrasive wear. Considering the fact that the d_{90} and d_{100} did not decrease drastically, which implies a rounding process as seen in the experiments with basalt pebbles from Vlasák et al. (2015), abrasive wear is indeed present. The cumulative mass percentage of particle sizes ≤1.4 mm did increase with more than 20%.

The complete procedure is repeated for *Test 2*. The initial batch of *Test 2* is shown in Figure 5.11. After the test, the batch is collected and the slurry is collected in buckets (comparable to Figure 5.13). After the sieving analysis a PSD is made. The PSD curve *Test 2* is given in Figure 5.15, in which the produced fines are highlighted with a light red color. The PSD characteristics are given in Table A.13.

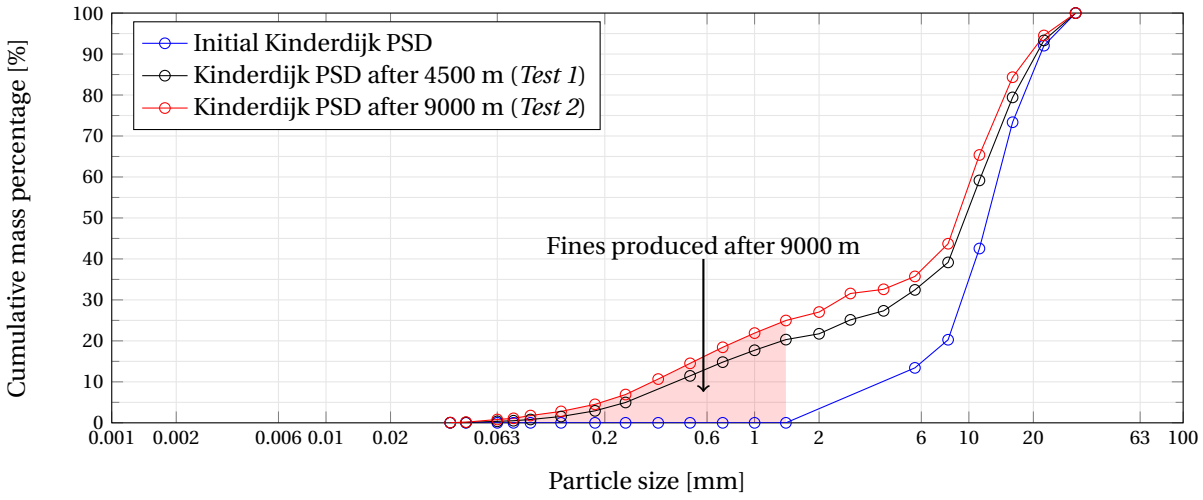

Figure 5.15: PSD curve from abrasive wear experiments after a testing length of 9000 meters (*Test 2*)

Figure 5.16: The batch of Kinderdijk nodules inside the Abrasive Wear Tester after *Test 2*

It can be concluded that, after the batch experiments with the Kinderdijk batch of polymetallic nodules, there is a cumulative increase of particles ≤1.4 mm of 24%, shown in Figure 5.16. The cumulative increase of particles ≤63 μm is equal to 0.81%. During *Test 1*, the d_{50} decreased more than during *Test 2* (from 9.74 mm to 8.93 mm), which could indicate that the batch used in *Test 2* are less angular or smoother than in *Test 1*. Figure 3.5 shows effect of the rounding of particles due to abrasion. With the rounding of the nodules during *Test 1*, it therefore produced less fine material in *Test 2*. Also, during the sieving analysis, it became clear that the clay fraction could lead to sticky problems when the fines were dried too quickly.

5.4.2. Results II - Batch Degradation Compared with Single Nodule Degradation

In section 4.4 it is proven that the equation of Archard (1953), can be used to predict single nodule degradation due to abrasive wear. The question arises whether this equation can also predict the effect of abrasive wear on a batch of polymetallic nodules.

In order to validate if the equation of Archard (1953) is applicable for batch experiments, the specific wear rate (k) from the results of section 4.4 and the sliding distances of the batch experiments, are substituted into this equation. First, the equation of Archard (1953) is revisited here.

$$V_w = k\, F_N\, s \tag{3.1 revisited}$$

For the calculation of the normal force (F_N), the two-layer model of Wilson (1976) is used. The two-layer model considers a fluid layer and a solids layer, which is schematically represented in Figure 5.17. This model can be used for predicting stratified slurry flows, especially when the main friction mechanism is mechanical friction of particles sliding against the pipe wall (De Hoog, 2016). There are different approaches to calculate the normal force, however, in this case the so-called hydrostatic normal stress approach is used. The calculation is given by Equation 5.3 (Wilson, 1976). A broad description of the use and outcome of the different approaches can be found in the work of De Hoog (2016).

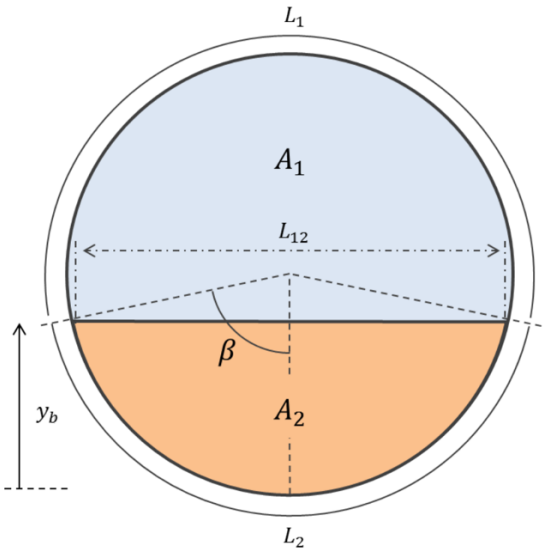

Figure 5.17: The two-layer model from the work of Wilson (1976), picture from De Hoog (2016)

$$F_N = \frac{D^2}{2}\, g\, C_{vb} \left(\rho_s - \rho_f\right) L_p \left(\sin\left(\beta\right) - \beta\cos\left(\beta\right)\right) \tag{5.3}$$

In Equation 5.3 and Figure 5.17, y_b represents the bed height. Because the water colored black after a few rotations (Figure 5.10), the only information of the bed height is given by the snapshots in Figure 5.9. Based on these snapshots the bed height is estimated to be one-fifth of the pipe diameter. Then, this estimated bed height can be used to calculate the angle between the top of the bed layer and the vertical symmetry axis, β. The position of this angle can be seen in Figure 5.17. The angle β is calculated as follows by Equation 5.4 and its result can be substituted into Equation 5.3. It should be noted that the angle β needs to be calculated in radians.

$$\beta = \cos^{-1}\left(1 - \frac{2y_b}{D}\right) \tag{5.4}$$

The bed concentration, denoted by C_{vb} in Equation 5.3, is estimated to be 55%. Eventually, with the normal force calculated from Equation 5.3, it can be substituted into Equation 4.8, in order to obtain the normalized remaining mass (m_n).

$$m_n = 1 - k\left(\frac{F_N}{m_1}\right) s\, \rho_{part} \tag{4.8 revisited}$$

In Equation 4.8, ρ_{part} represents the density of a wet nodule (1700 kg/m^3, see subsection 2.3.4) and m_1 denotes the weight of the batch before the test (*Test 1* or *Test 2*, respectively). The results from Equation 4.8

can be seen in Figure 5.18. Figure 5.18 is based on Figure 4.17, only extrapolated to a sliding length of 10000 meter, in order to plot the results of the Kinderdijk and Freiberg batch of nodules. The k factor used is in the equation of Archard (1953) is $k = 4.16{\cdot}10^{-9}$ [m^2/N]. The measured values for the remaining mass of the batches are based on the cumulative mass percentage of the particles ≤1.4 mm and are denoted by a black 'x' and '+'. For the result of Freiberg, also the cumulative mass percentage of the particles ≤1.4 mm is used, and the result is denoted by a black 'o'.

In Figure 5.18 also a ±25% range of the specific wear rate is given. Whereas, the 'upper'-boundary consists of a value of $k_{up} = 3.12{\cdot}10^{-9}$ [m^2/N], and the 'lower'-boundary has a value of $k_{low} = 5.20{\cdot}10^{-9}$ [m^2/N].

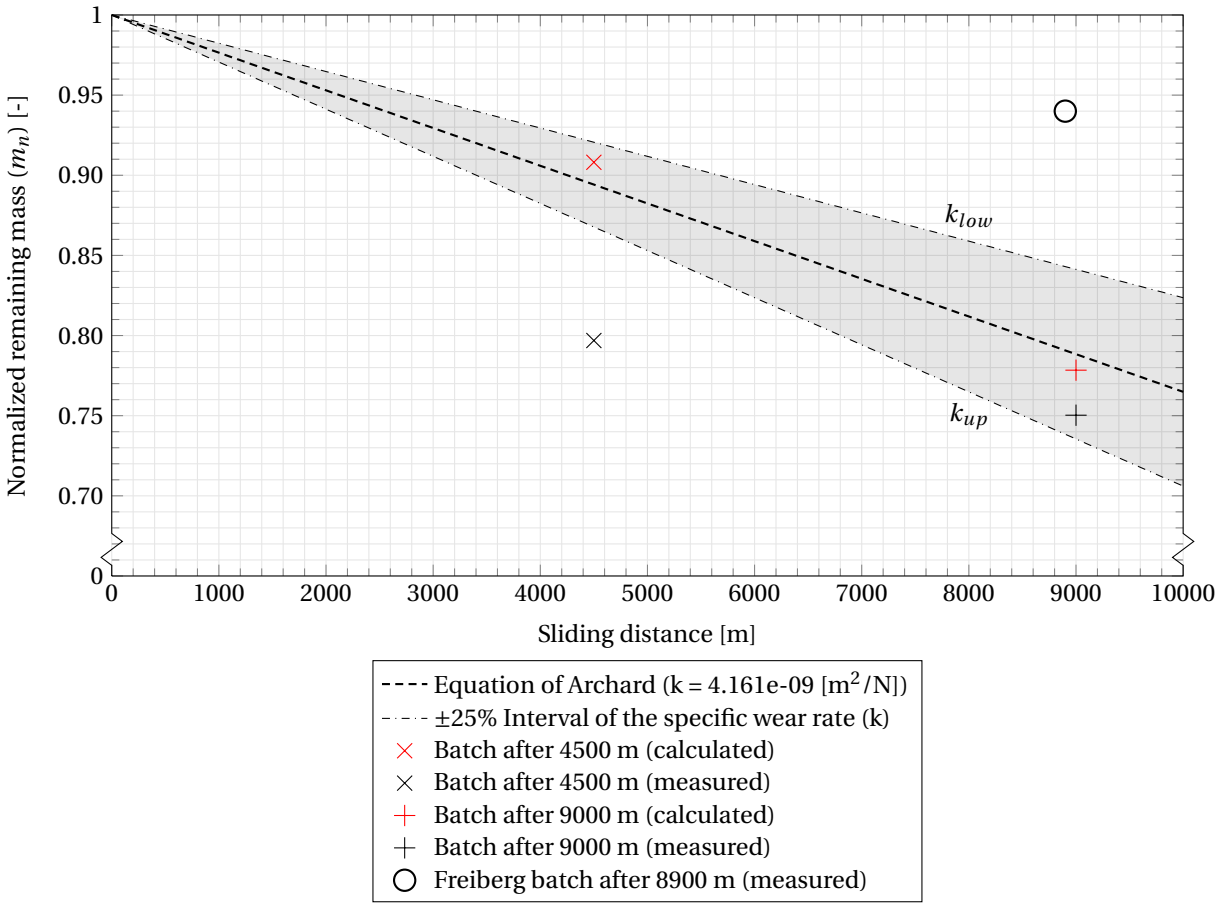

Figure 5.18: Normalized remaining mass plotted against the sliding distance

From Figure 5.18, it can be seen that the results of Equation 4.8 are within the ±25% range of the specific wear rate (k), while this value is obtained for single nodules. And also the measured value for *Test 2* is within this range. The measured results from *Test 1* and the Freiberg test deviate a lot from the obtained range, as shown in Figure 5.18. Because the data only consists of three data points, a good comparison is not really possible to make.

5.4.3. Results III - Comparison between the Kinderdijk and Freiberg Batch Properties

The PSD data of the Kinderdijk experiments (*Test 1* and *Test 2*) is compared with the PSD data from the Freiberg testing trials and its result is shown in Figure 5.19. A bigger production in fines in the Kinderdijk experiments compared to the Freiberg tests, can be seen. The d_{50} decreased more during the experiments in Kinderdijk, in total almost 28%, compared to roughly 1% in the Freiberg tests. This could be the effect of particle-particle interaction. During the tilting motion of the Abrasive Wear Tester (AWT) the particles move from one side to the other. Next, some particles will bump into the batch of particles which are waiting in front of the flange. This causes probably impact wear and therefore a relatively large decrease in the d_{50} of the batch.

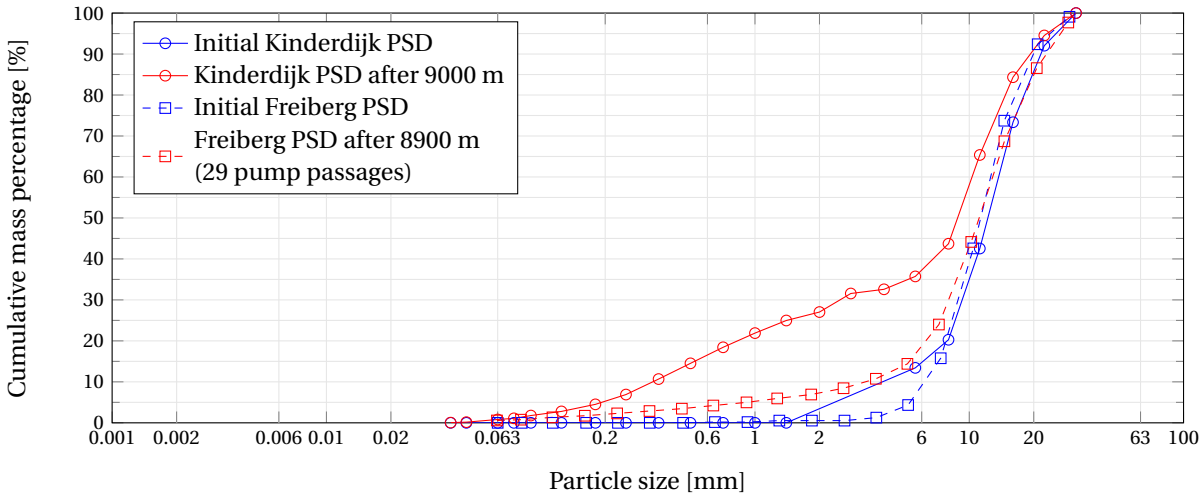

Figure 5.19: PSD curves from the abrasive wear experiments compared with the PSD curves from the Freiberg testing trials

From Figure 5.19, it can be concluded that the production of particles ≤1.4 mm during the Kinderdijk batch experiments are 4 times greater than during the Freiberg testing trials. The cumulative increase of particles ≤63 μm is equal to 0.81%. Most of the fine particles are created between the 0.2 and 2 mm.

5.4.4. Discussion

Discussion about the obtained results from the batch experiments in the Abrasive Wear Tester (AWT).

Discussion on Experimental Results I

The d_{50} decreased more for *Test 1* than for *Test 2*. Partially this is a good result for *Test 2*, because impact wear was hardly present during this test, but for *Test 1*, it holds that impact wear was present. This might be because of the particle-particle interaction, or due to the 'not enough' crushing of the nodules (crushing proceeded during *Test 1*).

After the fines came from the furnace, some of them stuck together as a paste. This could be caused by the clay content which, if it is dried too quickly, sticks together. Therefore, a small part of the fines were lost during the sieving and drying process. However, the clay fraction, with possibly some nodules in it, was obtained from the carrier fluid of the AWT. After the testrun the complete fluid was collected in buckets and these stood in the MTI laboratory for a week, to let the smallest particles settle. Further (chemical) research should point out what is the clay content inside the smallest fractions.

Discussion on Experimental Results II

The equation of Archard (1953) is partially valid, but as stated in subsection 5.4.2, a comparison is very difficult to make. There are too less data points to make a good comparison between the results. Although the calculated results showed a good agreement with the results from the single nodules experiments, the measured results (for a specific particle diameter) showed too much difference.

In Figure 5.18, the cumulative mass percentage of particles ≤1.4 mm after the Freiberg tests is plotted. As stated in section 5.2, the cumulative mass percentage of particles ≤1.4 mm increased with 6%. The total length of the test was 8900 meter, but the experimental setup consisted of both horizontal as vertical parts, as well as bends and a centrifugal pump. Therefore a comparison is in fact not possible.

Discussion on Experimental Results III

As can be concluded from Figure 5.19, the production of fines was greater in the Abrasive Wear Tester (AWT) than during the Freiberg testing trials. Also, a large decrease in d_{50} of the Kinderdijk batch is seen, which indicates impact wear during the test. Before the test the nodules were crushed, subsection 5.3.1, which should hold that they are less susceptible to impact wear, according to the work of Dreiseitl and Kondratenko (2012).

5.5. Conclusions and Recommendations

The following secondary research questions were formed at the beginning of this chapter:

- *Is the equation of Archard applicable to quantify the degradation due to abrasion for a batch of nodules?*
- *Until what extent does polymetallic nodule degradation propagate?*

5.5.1. Hypotheses

The following hypotheses have been formed in subsection 5.2.1.

- *Hypothesis 1:*

  The equation of Archard can be used to predict the degradation due to abrasive wear for a batch of polymetallic nodules.

  The first hypothesis has been partially falsified. As can be seen from Figure 5.18, the equation of Archard (1953) could be hypothetically used for a sliding distance of 9000 meter. However, the measured results are based on a cumulative mass percentage of particles ≤1.4 mm, which were initially not presented before *Test 1*. Also, the calculated results are based on estimated values, as mentioned in subsection 5.4.2. The shortage of data points makes that a good comparison with the results from the single nodule experiments, subsection 4.4.1, is impossible.

- *Hypothesis 2:*

  Particle degradation causes a production of fines until a size class which no longer degrades.

  The second hypothesis has been partially validated. From the sieving analysis it appeared that the mass remaining on the sieves, decreased as the sieve size became smaller, until the size class of 63 μm, see Table A.12. However, considering the data of the sieving analysis it can be concluded that the smallest sieve sizes, 38 μm and 45 μm did increase in mass. This could be related to the clay content, but the remaining mass on the sieve was not chemically analyzed.

5.5.2. Conclusions

Is the equation of Archard applicable to quantify the degradation due to abrasion for a batch of nodules?

From Figure 5.18 it can be seen that the result for a sliding distance of 9000 meter is within the specified range and thus that the result can be obtained using the equation of Archard (1953). However, the measured result of *Test 1*, after a sliding distance of 4500 meter, is far below the specified range. The calculated results are based on several assumptions and are highly hypothetical. For example, the material specific wear rate (k), obtained during the single nodule experiments of chapter 4, is used in the equation of Archard (1953). Also, the results of the single nodule experiments are extrapolated by a factor ten.

Until what extent does polymetallic nodule degradation propagate?

The smallest sieve size at the MTI laboratory was 38 μm, and in the container underneath this sieve were also particles present, after sieving. However, the color of this content was more brown than black, which could indicate a strong content of clay. It is not chemically analyzed, but there is a strong suspect that this is indeed clay. One of the conclusions of the work of Marchig and Halbach (1982) was that clayey material occurs in the inner regions of the polymetallic nodules, this could declare the production of clay during the batch experiments.

5.5.3. Recommendations

Polymetallic Nodule related Recommendations

Research on the chemical content of the smallest sieve sizes is recommended, what is for example the content of clay in the batch which remained on the 38 μm sieve. There are techniques to investigate these small sizes, by use of a laser particle sizer for example.

Particle Size Distribution related Recommendations

In this chapter the effect of abrasive wear on a PSD is investigated, but only a single distribution is used. For further research is it therefore recommended to investigate all sorts of different distributions, to gain more insight in the effect of abrasive wear on a distribution curve. For example, a comparison of the effect of abrasive wear on a narrow distribution and a wide distribution, could be researched.

Experimental Setup related Recommendations

It is recommended to research the influence of bends on the material specific wear rate (k). Also, the combination of centrifugal pumps and piping sections on the k-factor is an interesting subject. More research should be done to investigate the effect of particle-particle interaction in a batch on the material specific wear rate, whereby the batch does not continuously bumps into itself, what is the case in the Abrasive Wear Tester.

6

Modelling - Single Particle in a Vertical Turbulent Pipe Flow

When the vertical transportation system (VTS) is operational in the near future, the slurry flow through its pipes will be turbulent. In order to model a vertical turbulent pipe flow the open-source CFD package OpenFOAM is used. After the flow is generated, a single particle will be released into the flow on different locations at the inlet, in order to obtain an insight in the sliding distance due to particle-wall interactions. The addition of a single particle is done by use of MATLAB, whereas a DEM model is used to calculate the interaction forces between the particle and the pipe wall. This chapter provides an answer to two secondary research questions.

Secondary research questions of this chapter:

- *What is the ratio between the sliding length of the particle against the pipe wall and the total traveling length of the particle?*
- *Does the ratio of particle diameter over pipe diameter influence the sliding length per meter pipe?*

In section 6.1 an introduction to the modelling by means of a one-way coupled CFD-DEM model is given. This section also provides the geometry of the model and an overview of the assumptions and simplifications which are made. At the end of section 6.1 hypotheses are formed. An overview of the governing equations of the model is provided in section 6.2. First, the equations which resolve the flow are given in subsection 6.2.1, whereas the turbulence modelling is done by means of a LES model. Next, in subsection 6.2.2, the equations of the particle motion and the DEM model are given. The discretization schemes of both the fluid and particle motion are given in section 6.3. This section also describes the obtainment of the sliding lengths during the calculations. The modelling results are summarized in section 6.4. A sensitivity analysis is done using different sized particles and its outcome is described in subsection 6.4.3. A discussion of the modelling results is given in section 6.5. This chapter ends with an answer to the formed secondary research questions, conclusions and recommendations, provided in section 6.6. In Appendix B, more details about the mesh, modelling algorithms and figures from the simulations can be found.

6.1. Introduction - A Coupled CFD-DEM Analysis

Engineering problems consisting of fluid-structure or fluid-particle interaction are suitable to solve with coupled CFD-DEM models. Then, the fluid is solved by means of Computational Fluid Dynamics (CFD), whereas the motion of the particles is solved by means of a Discrete Element Method (DEM). In fact, the problem is divided into two parts, a fluid part and a particle part.

The coupling between the fluid part and the particle part can be done in different manners. The simplest option is the one-way coupling method, whereas the flow drives the particle, but the particle does not have influence on the flow. In Figure 6.1 the principle of a one-way coupled CFD-DEM method can be seen.

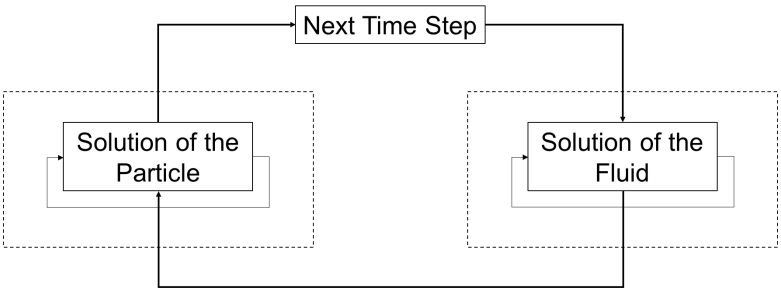

Figure 6.1: One-Way coupling method (Benra et al., 2011)

For this Master Thesis OpenFOAM is used to solve the motions of the fluid. Thereafter, the velocity field data is saved and transferred to MATLAB. MATLAB is used to calculate the forces on the particle from the fluid flow and, if required, to solve the DEM model during particle-wall interaction. The forces apply on the center of the particle, which is modeled as a point particle.

Model Geometry

In order to solve the fluid motion a mesh grid is required. The geometry is divided into cells on which boundary conditions can be applied.

The mesh grid is created by using the program Gmsh. Gmsh is a: "three-dimensional finite element mesh generator with built-in pre- and post-processing facilities"[1]. The structure of the mesh is comparable to the mesh used for the work of Munts et al. (2014). The inlet and outlet of the pipe consists of a squared mesh for one-third of the radius of the pipe. Between one-third of the radius and the complete radius the cell size decreases towards the outside of the pipe. The diameter of the mesh is equal to the diameter of the experimental setup (subsection 4.3.1). The length of the pipe in the simulation is chosen to be 3 meters, which is equal to twice the length of the pipe from the experiments. This is done due to the fact that one rotation in the experiment is equals a sliding distance of 3 meters.

In Figure 6.2 and Figure 6.3, the mesh generated by Gmsh shown in ParaView can be seen. "ParaView is an open-source, multi-platform data analysis and visualization application"[2]. In order to clarify the sideview, a midsection is removed and represented as a section with dashed lines. In Figure 6.2, the pipe diameter is given by D_{mp} and the total height is denoted as H_{mp}. The values for these and other model parameters are represented in Table 6.1. More details and pictures of the mesh can be found in Appendix B.

[1] Official website of Gmsh
[2] Official website of ParaView

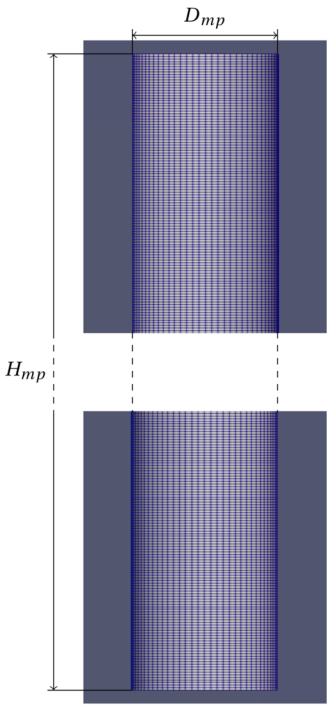

Figure 6.2: Sideview of the pipe mesh

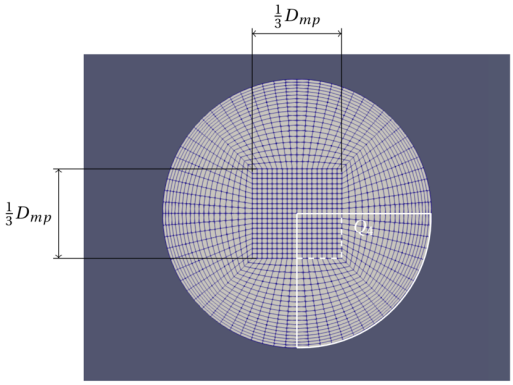

Figure 6.3: Mesh of the inlet and outlet of the model

Modelling Assumptions and Simplifications

The assumptions and simplifications used for the modelling are listed below. After each assumption or simplification there will be referred to the specific (sub)sections where it is used and/or clarified.

1. The particle is a point particle and follows the flow by means of a one-way coupling (section 6.1).
2. The flow is incompressible, which holds a constant density during the simulations (subsection 6.2.1).
3. The acceleration of the fluid is neglected, since large gradients only exist close to the wall, at positions where the particle will not come due to its geometry (subsection 6.2.1).
4. A polymetallic nodule is modeled as a sphere, thus the angularities are not taken into account. Also, the mass moment of inertia is not taken into account (subsection 6.2.2).
5. The influence of the wall (wall effect) on the settling velocity of a single sphere is not taken into account (subsection 6.2.2).
6. The mass decrease of the particle due to interactions with the wall during the simulations is neglected (subsection 6.3.2).

In section 6.5, a discussion is provided about these assumptions and simplifications.

6.1.1. Hypotheses

The following hypotheses are formed based on the secondary research questions given in this chapter:

– *Hypothesis 1:*

The ratio between the sliding length of the particle against the pipe wall and the total traveling length would be relatively small, most of the single particles would stay in the center of the pipe flow.

Considering the local concentration maps in vertical ascending pipes, from the work of Vlasák et al. (2014), it is expected that the majority of the simulations will show no particle wall collisions. The slurry concentrations are the highest in the center region of the pipe.

– *Hypothesis 2:*

The ratio particle diameter over pipe diameter does influence the sliding length, since smaller particles will follow the flow quicker than larger, heavier particles.

For smaller particles hold that they will follow the flow more instantaneously, compared to bigger particles. Therefore it is expected that smaller particles will interact more and longer with the pipe wall, resulting into larger sliding distances.

A validation or falsification of these hypotheses can be found in subsection 6.6.1.

6.2. Theory - Governing Equations of the Model

For the CFD-modelling it is chosen to work with OpenFOAM (Open source Field Operation And Manipulation). MATLAB is used to obtain the solution of the particle motion. In subsection 6.2.1 the governing equations to solve the fluid motion are given. Also, the turbulence modelling by means of a Large Eddy Simulation (LES) is given. In subsection 6.2.2 the governing equations to solve the particle motion are given. The calculation of the contact force with the wall is given, which is done with a (non-linear) spring-damper system. Before the governing equations are given for each part of the total solution, a list of most important modelling parameters are summarized in Table 6.1.

Table 6.1: Parameter overview

Symbol	Description	Unit	Value
D_{mp}	Pipe Diameter	[m]	0.150
H_{mp}	Pipe Length	[m]	3
Δt	Time Step	[s]	0.0025
ρ_f	Fluid Density	[kg/m^3]	1000
ν_f	Kinematic Fluid Viscosity	[m^2/s]	1.0035E-06
w_f	Internal Vertical Fluid Flow	[m/s]	4
A^+	van Driest Constant	[-]	26
d_p	Particle Diameter	[m]	0.050
V_p	Particle Volume	[m^3]	6.5450E-05
ρ_{part}	Particle Density	[kg/m^3]	1700
m_p	Particle Mass	[kg]	0.1113
$m_{a,p}$	Particle Added Mass	[kg]	0.0327
C_D	Coefficient of Drag	[-]	0.445
$d_{p,DEM}$	DEM Particle Diameter	[m]	0.055
k_{spr}	DEM Spring Constant	[N m^2]	1.77E-06
c_{dmp}	DEM Damping Constant	[kg/s]	0.700

6.2.1. Resolving the Fluid Flow

First, the general equations of motion are presented, which is followed by information about the modelling approach using a LES model. Thereafter, the boundary conditions with respect to the flow are given. Furthermore, a part about the fluid acceleration during the simulations and the reasoning behind modelling simplification three (section 6.1), is described. This subsection ends with a short explanation about the PIMPLE algorithm, used in for the calculations in OpenFOAM.

General Equations of Motion

Before the general equations of motion of the fluid flow are given, first the three conservation laws are presented. The fundament of fluid mechanics is given the following conservation laws:

- Conservation of mass
- Conservation of momentum
- Conservation of energy

Ling et al. (2013) stated that if the focus lies on the momentum coupling between a fluid and a particle, the conservation of energy equations of both parts is not considered. In Figure 6.1 it can be seen that this model only incorporates the coupling between the fluid and particle. Therefore, only conservation of mass and conservation of momentum are taken into account.

The first conservation law, the mass conservation law, states that mass is conserved over time in a closed system. In other words, in a fluid system mass cannot disappear from the system, nor be created (Hirsch, 2007). The mass conservation law is given by Equation 6.1. Using the incompressibility constraint, which states that the density of the fluid does not change over time, the mass conservation equation is referred to as the continuity equation. If the density of the fluid is constant over time, the first term of Equation 6.1 drops out. Leaving out the fluid density in the second term, because the fluid density cannot be equal to zero, results into the continuity equation. The continuity equation is also known as the divergence free field (Hirsch, 2007). In Equation 6.1, ρ_f represents the fluid density, which is chosen as $\rho_f = 1000\ \mathrm{kg/m^3}$, whereas $\mathbf{u}_f$ denotes the vector containing the fluid velocity in all three directions.

$$\frac{\partial \rho_f}{\partial t} + \nabla \cdot \left(\rho_f \mathbf{u}_f\right) = 0 \tag{6.1}$$

The second conservation law, the conversation of momentum, states that the momentum of a system is conserved, if there are no external forces acting on the system. Momentum is a vector quantity, in fluid mechanics often expressed in momentum per unit of volume, which is obtained by taking the product of density and velocity (Hirsch, 2007). The conservation of momentum equation is represented by Equation 6.2.

$$\rho \frac{\partial \mathbf{u}}{\partial t} + \rho \left(\mathbf{u} \cdot \nabla\right) \mathbf{u} = -\nabla p + \nabla \tau + \rho f_e \tag{6.2}$$

From the conservation of momentum equation, Equation 6.2, the motion of fluids can be described by the Navier-Stokes equations. Using the incompressibility constraint, and therefore using Equation 6.1, the Navier-stokes equations can be written as Equation 6.3. The Navier-Stokes equations describe the fluid flow in three directions.

$$\frac{\partial \rho_f \mathbf{u}_f}{\partial t} + \nabla \cdot \left(\rho_f \mathbf{u}_f \mathbf{u}_f\right) = -\nabla p + \nabla \cdot \left(\mu \left(\nabla \mathbf{u}_f + \nabla \mathbf{u}_f^T\right)\right) + \rho_f \mathbf{g} \tag{6.3}$$

Equation 6.3 can be divided by the fluid density on both sides (ρ_f), and using the kinematic fluid viscosity (ν_f), the equation can be rewritten as follows by Equation 6.4.

$$\frac{\partial \mathbf{u}_f}{\partial t} + \nabla \cdot \left(\mathbf{u}_f \mathbf{u}_f\right) = -\nabla p + \nabla \cdot \left(\nu_f \left(\nabla \mathbf{u}_f + \nabla \mathbf{u}_f^T\right)\right) + \mathbf{g} \tag{6.4}$$

In Equation 6.4, the left hand side refers to the inertia per volume. Whereas the first term represents the local variation of the fluid over time and the second term accounts for the convection, or movement of the fluid. The complete left hand side could also be written as a material derivative, represented by Equation 6.5.

$$\frac{D\mathbf{u}}{Dt} = \overbrace{\underbrace{\frac{\partial \mathbf{u}}{\partial t}}_{\text{Variation}} + \underbrace{\left(\mathbf{u} \cdot \nabla\right) \mathbf{u}}_{\text{Convection}}}^{\text{Inertia per volume}} \tag{6.5}$$

The first term on the right hand side of Equation 6.4, represents the diffusion, which accounts for the movement or motions of particles. The incompressible Navier-Stokes equations can therefore be shared under the group of convection-diffusion equations.

The Navier-Stokes equations are solved using a Large Eddy Simulation model (LES). LES models require a filtering approaching on the Navier-Stokes equations and uses sub-grid-scale models for the closure terms. More information about the filtering approach can be found in Goeree (2018). In the followup the turbulence modelling by means of a LES model is shortly explained.

Turbulence Modelling - Large Eddy Simulation

The smallest eddies will not influence the motions of the relatively large polymetallic nodules. Therefore it is chosen to construct a model using a Large Eddy Simulation (LES). In LES models the time-dependent flow equations are solved for the mean flow and largest eddies, whilst the smallest eddies are modeled using a sub-grid-scale model (Versteeg and Malalasekera, 1995). In OpenFOAM, different sub-grid-scale models can be selected. For this work the sub-grid-scale *kEqn* model is used [3]. The (default) values for the *kEqn* model are $C_e = 1.048$ and $C_k = 0.094$. Furthermore, the Van Driest (1956) damping function is applied, represented in Equation 6.6. This damping function is used in order to reduce the eddy viscosity to zero at the walls (Goeree, 2018). The van Driest coefficients are $A^+ = 26$ and $C_\delta = 0.158$, whereas the value of A^+ represents a smooth wall. In Equation 6.6, y^+ accounts for the distance from the wall normalized by a viscous length scale (Pope, 2000).

$$D = 1 - \exp\left(-y^+ / A^+\right) \tag{6.6}$$

The largest eddies (ℓ_L) during the simulations can have a length which is equal to half the pipe diameter (Goeree, 2018), whereas the smallest eddies are given by the Kolmogorov length scale (ℓ_k). The Kolmogorov length scale is obtained as follows by Equation 6.7.

$$\ell_k = 4\, D_p\, Re^{-0.78} \tag{6.7}$$

In Equation 6.7, D_p accounts for the pipe diameter and Re for the Reynolds number of the flow, which can be calculated using Equation 6.8. The Reynolds number is a dimensionless number which represents the ratio between the internal forces and the viscous forces. In Equation 6.8, w_f represents the (initial) vertical flow velocity of the pipe, D_p is the pipe diameter and ν_w accounts for the kinematic viscosity of water. The fluid is a newtonian fluid, which states that the viscosity of a fluid does not change along the strain with the flow. The kinematic viscosity of water at 20°C is $\nu_w = 1.0035 \cdot 10^{-6}$ m^2/s.

$$Re = \frac{w_f\, D_p}{\nu_w} \tag{6.8}$$

For a flow of $w_f = 4$ m/s through the pipe model of Figure 6.2, the Reynolds number is $Re = 6 \cdot 10^5$. Substituting this result into Equation 6.7, the smallest eddies (Kolmogorov length scale) are around $\ell_k = 19\ \mu$m, whereas the largest eddies (half of the pipe diameter) are $\ell_L = 75 \cdot 10^3\ \mu$m. Thus, the length of an eddy (ℓ_e) during the simulations is within the range as given by Equation 6.9.

$$\begin{aligned} \ell_k \leq \ell_e &\leq \ell_L \\ 19\,\mu\text{m} \leq \ell_e &\leq 75 \cdot 10^3\,\mu\text{m} \end{aligned} \tag{6.9}$$

In order to save computational time, synthetic eddies are created on the inlet boundary of the model. Further elaboration of the boundary conditions can be found in the following.

Boundary Conditions with respect to the Flow

Both velocity as pressure boundary conditions need to be specified in OpenFOAM. The boundary condition for the flow on the inlet of the pipe, shown in Figure 6.3, is a turbulent inlet condition. The turbulent inlet condition (command in OpenFOAM: turbulentInlet) generates a fluctuating component to a reference (mean) field[4]. The outlet of the pipe, also shown in Figure 6.3, consists of a zero gradient boundary condition. The zero gradient boundary condition, or Neumann boundary condition, sets all gradients to zero. The zero gradient boundary condition is also applied on the pressure terms at the inlet of the pipe and on the pipe wall. The fluid flow is not allowed to cross the wall, therefore a Dirichlet boundary condition is given to the pipe wall. The pipe wall of the model can be seen in Figure 6.2. The Dirichlet boundary condition is often

[3] OpenFOAM Extended Code Guide - Large Eddy Simulation (LES)
[4] OpenFOAM Extended Code Guide - Turbulent Inlet

referred to as the no-slip boundary condition. This boundary condition holds that the wall velocity is equal to the velocity of the fluid. Regarding the pressure boundary condition at the outlet of the pipe, it has a fixed boundary condition, whereas the value of the boundary is equal to the internal field value. In Table 6.2 an overview of the boundary conditions used in the model can be seen, for both the velocity and pressure. In Table 6.2, BC refers to boundary condition.

Table 6.2: Boundary conditions for the vertical turbulent pipe flow

Boundary	Velocity (BC)	Pressure (BC)
Inlet	Turbulent inlet	Zero gradient
Wall	No-slip	Zero gradient
Outlet	Zero gradient	Fixed value (internal field)

Acceleration of the Fluid

In a turbulent pipe flow the fluid accelerates differently on different locations inside the pipe. Locally the acceleration could be relatively high compared to the acceleration of the fluid in the center of the pipe. In Figure 6.4 a velocity vector field in a bend is shown, from which it can be seen that the velocity in the inner corner of the bend first accelerates rapidly, and after the corner the fluid decelerates, resulting into a very small flow velocity. A turbulent velocity field in a straight pipe is shown in Figure 6.5. This velocity profile shows large gradients or fluid accelerations, close to the pipe wall, but overall it is a rather constant profile. The acceleration of the fluid velocity can be calculated using Equation 6.10. Its representation is called the material derivative.

$$\frac{D\mathbf{u}_f}{Dt} = \frac{\partial \mathbf{u}_f}{\partial t} + \mathbf{u}_f \cdot \nabla \mathbf{u}_f \tag{6.10}$$

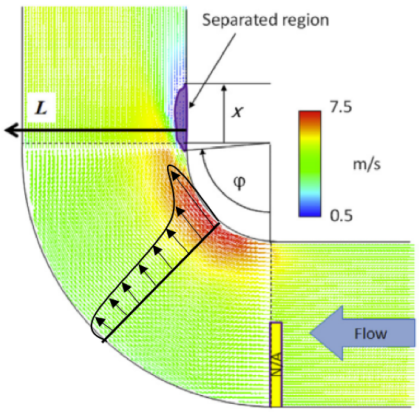

Figure 6.4: Turbulent fluid velocity vector field in a bend (Ebara et al., 2016)

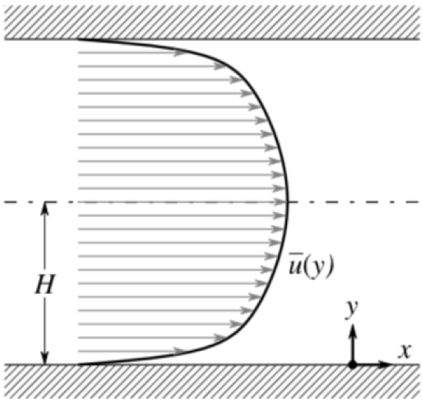

Figure 6.5: Turbulent mean fluid velocity field in a straight pipe (Nieuwstadt et al., 2016)

It can be concluded from Figure 6.4 and Figure 6.5, that the (mean) turbulent fluid velocity field in a bend is different than for a pipe. The largest gradients in a straight pipe exists close to the pipe wall, whilst for a pipe bend the largest gradients are dominantly present at the inner corner. Due to the size of polymetallic nodules from the Clarion-Clipperton Zone (CCZ), between 10 and 100 mm (Mero, 1965; Skornyakova and Murdmaa, 1992; Van Wijk, 2016), it can be concluded that the nodules will hardly experience the large fluid accelerations close to the wall. Therefore, the model is simplified by setting the material derivative, which accounts for the fluid acceleration, as shown by Equation 6.10, to zero. This simplification, given by Equation 6.11, is also of influence of the general equation of the particle motion, Equation 6.18, which is explained in subsection 6.2.2.

$$\frac{D\mathbf{u}_f}{Dt} = 0 \tag{6.11}$$

The PIMPLE Algorithm

The PIMPLE algorithm is used for calculations. This algorithm is a combination of two other algorithms, SIMPLE (Caretto et al., 1973) and PISO (Issa, 1986). The abbreviation SIMPLE stands for Semi-Implicit Method for Pressure Linked Equations. The abbreviation PISO stands for Pressure Implicit with Splitting of Operators. Whereas the SIMPLE algorithm is specialized in solving steady, incompressible flows and the PISO algorithm can solve time-dependent problems due to the extra pressure-corrector step (Munts et al., 2014). Thus, the advantage of the PIMPLE algorithm is that the time step could be enlarged and so there can be calculated with large Courant numbers (Holzmann, 2017). The Courant number (Courant et al., 1928) is obtained as follows by Equation 6.12. The Courant number is a criterion for which holds the convergence and stability of finite difference schemes (Hirsch, 2007).

$$CFL = \Delta t \sum_{i=1}^{n} \frac{u_{x_i}}{\Delta x_i} \tag{6.12}$$

6.2.2. Resolving the Particle Motion

In this section the equations of motions which account for the particle motion will be derived. First, the boundary and initial conditions with respect to the particle are given. Second, the general equations of motion are presented, which is followed by a separate section about the drag force and the contribution of added mass. Then, the final equations of the particle motion are given, which are only valid if there is no interaction with the pipe wall. The horizontal equation of motion will change during particle-wall interaction, which will be explained in the last part of this subsection.

Boundary and Initial Conditions with respect to the Particle

The initial conditions of the particle consists of both position as velocity. First the initial position is explained, which is followed by the initial conditions of the velocity.

The start position, or initial position, of the particle is randomly chosen over the inlet of the pipe. It must be secured that the particle boundary does not exceed the pipe wall, which holds that the center of the particle must be at least a particle radius distant from the wall, at the start position. Therefore the condition of Equation 6.13 must be satisfied during the determination of the start position. A schematic representation of this condition is given in Figure 6.6.

$$\sqrt{\left(x_p^2 + y_p^2\right)} \leq R_p - r_p \tag{6.13}$$

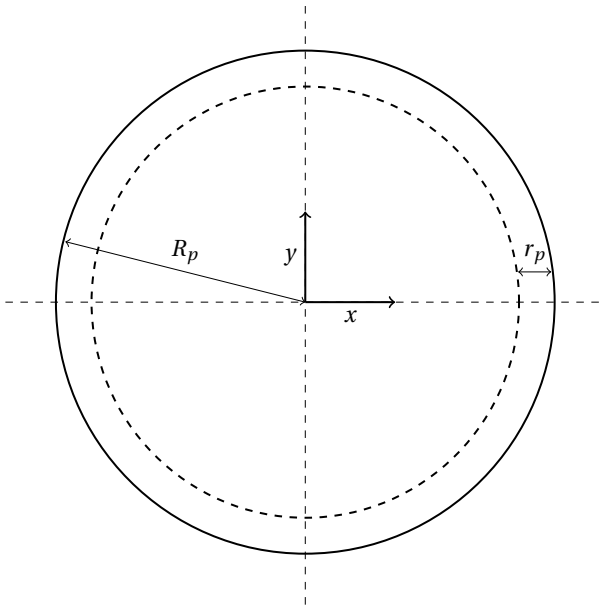

Figure 6.6: Schematic representation of the particle boundary condition in the pipe

In Equation 6.13, x_p and y_p represent the x- and y-coordinate of the center of the particle, whereas R_p and r_p represent the pipe radius and the radius of the particle, respectively. In order to secure that the condition of Equation 6.13 is always satisfied, a random angle ($0° \leq \alpha \leq 360°$) and random radius ($0 \leq R_{pos} \leq 1$) are generated by MATLAB. Next, the initial positions ($t = 0$) of x_p and y_p are calculated using Equation 6.14. The vertical initial position, denoted by $z_p(t = 0)$, which represents the z-coordinate of the center of the particle, is equal to one particle radius from the inlet. Thus, the particle starts exactly at the inlet of the pipe.

$$\begin{aligned} \alpha &= 2\,\pi\ (Rand\{0,1\}) \\ R_{pos} &= \sqrt{Rand\{0,1\}} \\ x_p(t=0) &= \left(R_p - r_p\right) R_{pos} \cos(\alpha) \\ y_p(t=0) &= \left(R_p - r_p\right) R_{pos} \sin(\alpha) \\ z_p(t=0) &= r_p \end{aligned} \tag{6.14}$$

Particles are released in the flow with no initial horizontal velocity, represented as u_p and v_p in Equation 6.16. The initial vertical particle velocity represented as w_p in Equation 6.16, is equal to the internal vertical fluid flow (w_f) minus the settling velocity of the released particle. If the initial vertical velocity of the particle is equal to zero, it would take too long for the particle to accelerate and reach a representative velocity during a simulation. The terminal settling velocity (v_t) is calculated using Equation 6.15 (Ferguson and Church, 2004). The parameters a and b are chosen as $a = 18$ and $b = 1.1$, equal to the choice in the work of Van Wijk (2016). The initial conditions of the particle velocity are shown in Equation 6.16.

$$v_t = \left(\frac{\rho_{part} - \rho_f}{\rho_f}\right) g\, d_p^2 \left(a\, \nu_f + \left[0.75\, b \left(\frac{\rho_{part} - \rho_f}{\rho_f}\right) g\, d_p^3\right]^{0.5}\right)^{-1} \tag{6.15}$$

$$\begin{aligned} u_p(t=0) &= 0 \\ v_p(t=0) &= 0 \\ w_p(t=0) &= w_f - v_t \end{aligned} \tag{6.16}$$

The particle used in the model is modeled as a sphere. This simplifies the modeling greatly, since a lot of equations use the radius of a particle or the particle volume. For example, the settling equation uses a particle diameter (d_p), or the equation for the drag force can also be written in terms of the particle diameter.

First, simulations are done using a particle with a particle diameter which is equal to one-third of the pipe diameter. This particle is referred to as *"Particle 1"*. In the sensitivity analysis of subsection 6.4.3, two smaller particles are released in the flow. *"Particle 2"*, which has a diameter of one-sixth of the pipe diameter and *"Particle 3"*, having a particle diameter of one-tenth of the pipe diameter. Further elaboration on the sensitivity analysis can be found in subsection 6.4.3. Figures of the particle during a simulation can be found in Appendix B.

General Equations of Motion

As stated before, an individual point particle is used during the simulations. The motion of an individual particle can be described using the second law of Newton, given by Equation 6.17. In Equation 6.17, $\mathbf{F}$ represents the sum of all forces which act on the particle, m_p is the mass of the particle and $\mathbf{a}_p$ gives the acceleration of the particle in each direction.

$$\mathbf{F} = m_p\, \mathbf{a}_p \tag{6.17}$$

The equation of motion of a particle in a non-uniform flow field is researched by Maxey and Riley (1983) and thereafter simplified by Ling et al. (2013). The equation of motion obtained by Ling et al. (2013) is given by Equation 6.18.

$$m_p \left(\frac{d\,\mathbf{u}_p}{dt}\right) = m_p\, \mathbf{g} + \rho_f\, V_p \left(\frac{D\,\mathbf{u}_f}{Dt} - \mathbf{g}\right) + \mathbf{F}_D + \mathbf{F}_a + \mathbf{F}_h \tag{6.18}$$

The left hand side of Equation 6.18 accounts for the force due to acceleration of the particle. The first term on the right hand side is the force caused by gravity, whereas the second term is recognized as the force due to

buoyancy. In the previous subsection, subsection 6.2.1, it is explained that the fluid acceleration, denoted as a material derivate in Equation 6.18, is not taken into account. Therefore, with Equation 6.11, Equation 6.18 can then be written as given by Equation 6.19.

$$m_p\left(\frac{d\,\mathbf{u}_p}{dt}\right) = \left(m_p - \rho_f\, V_p\right)\mathbf{g} + \mathbf{F}_D + \mathbf{F}_a + \mathbf{F}_h \tag{6.19}$$

The last term on the right hand side of Equation 6.19, is a history force, denoted by $\mathbf{F}_h$. The influence of this term is noted, however, for further modeling simplifications this term is not considered in this work and will therefore drop out of Equation 6.19.

Drag Force and Added Mass

In Equation 6.19, $\mathbf{F}_D$ denotes the drag force acting on a particle. For small particles ($d_p < 0.1$ mm) in a laminar flow, the drag force can be calculated using Stokes law. However, since particle has the size of a polymetallic nodule and is enclosed by a turbulent pipe flow, the drag force of Stokes will not hold. The drag force is calculated using the general equation for drag force. This equation is given by Equation 6.20. In Equation 6.20, C_D denotes the drag force coefficient of the particle. The projected area of the particle is given by A_p, since the particle is modeled as a sphere, this area is given by a circle in each direction. The fluid and particle velocity in each direction is denoted by $\mathbf{u}_f$ and $\mathbf{u}_p$, respectively.

$$\mathbf{F}_D = \frac{1}{2} C_D\, \rho_f\, A_p \left|\mathbf{u}_f - \mathbf{u}_p\right| \left(\mathbf{u}_f - \mathbf{u}_p\right) \tag{6.20}$$

The settling velocity of a particle is influenced by the presence of the wall, this effect is researched by Di Felice (1996). In the work of Goeree et al. (2017), the settling of a particle in a confined space is numerically modelled using an Immersed Boundary Method (IBM). The wall effect can be clearly seen from both studies, however, as stated in section 6.1, this effect is not taken into account. In a two-way coupled model, as used in Goeree et al. (2017), the wall effects the particle motion directly. In a one-way coupled model the fluid is not disturbed and influenced by the presence of a particle, as shown in Figure 6.1. It is unclear how to compensate for the drag force in a one-way coupled model, the drag force is therefore calculated using Equation 6.20.

The third term on the right hand side of Equation 6.19, $\mathbf{F}_a$, represents the added mass force. This force accounts for the effect that if a particle accelerates through a fluid, it must displace the fluid. The added mass in calculated using Equation 6.21. In Equation 6.21, V_p represents the volume of the particle, which is in this case the volume of a sphere.

$$\mathbf{F}_a = \frac{1}{2}\rho_f\, V_p \left(\left(\frac{D\,\mathbf{u}_f}{Dt}\right) - \left(\frac{d\,\mathbf{u}_p}{dt}\right)\right) \tag{6.21}$$

Again, as can be seen in Equation 6.21, in the added mass force the acceleration of the fluid is accounted for. With the reasoning as stated before in subsection 6.2.1 and Equation 6.11, this term is not taken into account. Therefore, the added mass force ($\mathbf{F}_a$) can be written as given by Equation 6.22.

$$\mathbf{F}_a = -\frac{1}{2}\rho_f\, V_p \left(\frac{d\,\mathbf{u}_p}{dt}\right) \tag{6.22}$$

The resulting equations for both the drag, Equation 6.20, as the added mass force, Equation 6.22, are substituted in the general equation of motion for the particle motion, Equation 6.19. The result of this substitution is given in the followup part of this subsection.

Final Equations of the Particle Motion

As stated before, Equation 6.20 and Equation 6.22, are substituted into Equation 6.19. Then, after rewriting, this results into Equation 6.23. Equation 6.23 is the total equation of motion in vertical direction. In horizontal direction the first term on the right hand side, containing the gravitational acceleration, is not of influence and therefore drops out of the equation. The equation which accounts for the horizontal motions of the particle is provided by Equation 6.25.

$$\left(m_p + \frac{1}{2}\rho_f\, V_p\right)\left(\frac{d\,\mathbf{u}_p}{dt}\right) = \left(m_p - \rho_f\, V_p\right)\mathbf{g} + \frac{1}{2} C_D\, \rho_f\, A_p \left|\mathbf{u}_f - \mathbf{u}_p\right| \left(\mathbf{u}_f - \mathbf{u}_p\right) \tag{6.23}$$

Rearranging the terms of Equation 6.23 results into Equation 6.24. Applying a simple integration over time on this equation, results into the vertical velocity. Another time integration gives the updated vertical position of the particle.

$$\left(\frac{d\,\mathbf{u}_p}{dt}\right) = \frac{\left(m_p - \rho_f V_p\right)\mathbf{g}}{\left(m_p + \frac{1}{2}\rho_f V_p\right)} + \frac{\frac{1}{2}C_D\,\rho_f\,A_p}{\left(m_p + \frac{1}{2}\rho_f V_p\right)}\left|\mathbf{u}_f - \mathbf{u}_p\right|\left(\mathbf{u}_f - \mathbf{u}_p\right) \tag{6.24}$$

Equation 6.23 holds in the vertical direction, in horizontal direction the force due to gravity and buoyancy is excluded, so the equation can be written as follows by Equation 6.25.

$$\left(m_p + \frac{1}{2}\rho_f V_p\right)\left(\frac{d\,\mathbf{u}_p}{dt}\right) = \frac{1}{2}C_D\,\rho_f\,A_p\left|\mathbf{u}_f - \mathbf{u}_p\right|\left(\mathbf{u}_f - \mathbf{u}_p\right) \tag{6.25}$$

Rearranging the terms of Equation 6.25 results into Equation 6.26. The horizontal equations of the particle motion can therefore be written as given by Equation 6.26.

$$\left(\frac{d\,\mathbf{u}_p}{dt}\right) = \frac{\frac{1}{2}C_D\,\rho_f\,A_p}{\left(m_p + \frac{1}{2}\rho_f V_p\right)}\left|\mathbf{u}_f - \mathbf{u}_p\right|\left(\mathbf{u}_f - \mathbf{u}_p\right) \tag{6.26}$$

With the particle acceleration known, from either Equation 6.24 for the vertical motion or Equation 6.26 for the horizontal motion, the velocity of the particle can be obtained. This velocity can be used to calculate the next position of the particle in the flow. The new position of the particle in the pipe can be calculated using Equation 6.27. Equation 6.27 shows the calculation of the three coordinates of the particle, denoted by vector $\mathbf{x}_p$. In Equation 6.27, vector $\mathbf{C}$ represents the integration constant, which is in this case represents the previous position of the particle.

$$\mathbf{x}_p = \int_{t_0}^{t_1} \mathbf{u}_p\,dt + \mathbf{C} \tag{6.27}$$

The equation for the vertical acceleration of the particle, Equation 6.24, and for the motions in the horizontal plane, Equation 6.26, will be discretized in subsection 6.3.1. In Appendix B, the algorithm which relates the particle position to the grid position, can be found. In short, this algorithm checks the closest grid point to the (new) position of the particle. This algorithm is also used to obtain the velocity data $\mathbf{u}_f$, necessary for Equation 6.24 and Equation 6.26, for example.

Wall Collision Model and Contact Force Calculation

Attached to the next position of the particle, calculated with Equation 6.27 is the presence of the pipe wall, which restricts the particle from freely moving around. When a particle collides with the wall due to the drag force, Equation 6.20, the wall will exert a force on the particle. The total contact force therefore is the sum of the hydrodynamical and collisional forces (Tsuji et al., 1993). The total contact force is assumed to be the normal force which can be used in the equation of Archard (1953), Equation 3.1. So, the contact force can be calculated using Equation 6.28.

$$\mathbf{F}_N = \mathbf{F}_D + \mathbf{F}_c \tag{6.28}$$

For modelling particle-particle interaction, Kloss et al. (2012) used a spring-dashpot system as schematically represented by Figure 6.7. The spring-dashpot model can also be used to model particle-wall interaction (Kloss et al., 2012).

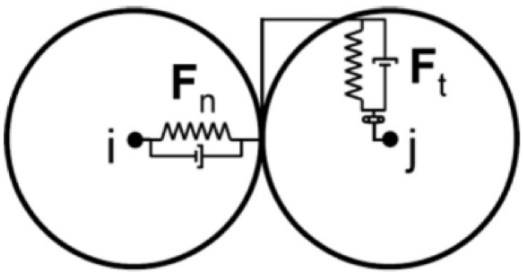

Figure 6.7: Spring-dashpot model (Kloss et al., 2012)

The modelling of the contact force, represented by $\mathbf{F}_c$ in Equation 6.28, is done with a non-linear spring-dashpot model. The method of a spring-dashpot DEM model, originates from the work of Cundall and Strack (1979).

$$\mathbf{F}_c = -\frac{k_{spr}}{\delta^2} - c_{dmp}\,\mathbf{u}_p \tag{6.29}$$

In Equation 6.29, δ represents the distance between the radius of the particle with unloaded springs (r_{pb}) and the particle radius (r_p). In an unloaded situation the spring-dashpot system creates an imaginary layer which is 10% greater in radius than the original particle. In Figure 6.8 a particle that is used in the model can be seen. With the introduction of the wall collision model, the condition of Equation 6.13 can be adapted in order active the springs and dampers. The activation criterion is given by Equation 6.30.

$$R_p - r_{pb} \leq \sqrt{\left(x_p^2 + y_p^2\right)} \leq R_p - r_p \tag{6.30}$$

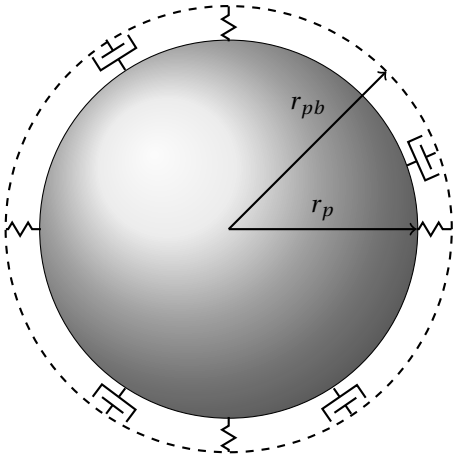

Figure 6.8: Schematic representation of the spring-damper system around the particle in the simulation

When the criterion of Equation 6.30 is satisfied, the spring-dashpot system becomes active. The collision force of Equation 6.29 will then be added (or subtracted) to the horizontal particle equation of motion, Equation 6.25. Thus, with the activation of the spring-dashpot system, the equation of motion in horizontal direction is given by Equation 6.31.

$$\left(m_p + \frac{1}{2}\rho_f V_p\right)\left(\frac{d\,\mathbf{u}_p}{dt}\right) = \frac{1}{2}C_D\,\rho_f\,A_p\left|\mathbf{u}_f - \mathbf{u}_p\right|\left(\mathbf{u}_f - \mathbf{u}_p\right) \pm \left(\frac{-k_{spr}}{\delta^2} - c_{dmp}\,\mathbf{u}_p\right) \tag{6.31}$$

Rearranging the terms of Equation 6.31 results into Equation 6.32.

$$\left(\frac{d\,\mathbf{u}_p}{dt}\right) = \frac{\frac{1}{2}C_D\,\rho_f\,A_p}{\left(m_p + \frac{1}{2}\rho_f\,V_p\right)}\left|\mathbf{u}_f - \mathbf{u}_p\right|\left(\mathbf{u}_f - \mathbf{u}_p\right) \pm \frac{\left(\frac{-k_{spr}}{\delta^2} - c_{dmp}\,\mathbf{u}_p\right)}{\left(m_p + \frac{1}{2}\rho_f\,V_p\right)} \tag{6.32}$$

After a collision the velocity and position of the particle can be calculated, by using Equation 6.32. With this result, the normal force during the collision can be obtained, using Equation 6.33.

Due to the geometry of the pipe, whereas the center of the pipe is taken as the origin of an axis system, the collisional force changes its direction. Therefore it is chosen to divide the pipe into four quarters, as can be seen in Figure 6.9. The drag force, as given by Equation 6.32, adapts automatically to its direction and quarter, because the first velocity difference is taken as an absolute difference, whilst the other velocity difference is taken as relative. In order to obtain the normal force, with the orientation per quarter of the pipe in mind, the

collision force is needed to be summed or subtracted from the drag force. In Figure 6.9 the orientation of the normal forces are schematically represented.

$$F_N = \overbrace{\frac{1}{2} C_D \rho_f A_p \left|\mathbf{u}_f - \mathbf{u}_p\right| \left(\mathbf{u}_f - \mathbf{u}_p\right)}^{F_D} \pm \overbrace{\left(\frac{-k_{spr}}{\delta^2} - c_{dmp}\,\mathbf{u}_p\right)}^{F_C} \tag{6.33}$$

The normal force, calculated by Equation 6.33, is used to calculate the wall friction force which substituted into the equation of the vertical particle motion. Since the particle will decelerate in vertical direction during particle-wall interaction. The procedure to do this can be found in subsection 6.3.2.

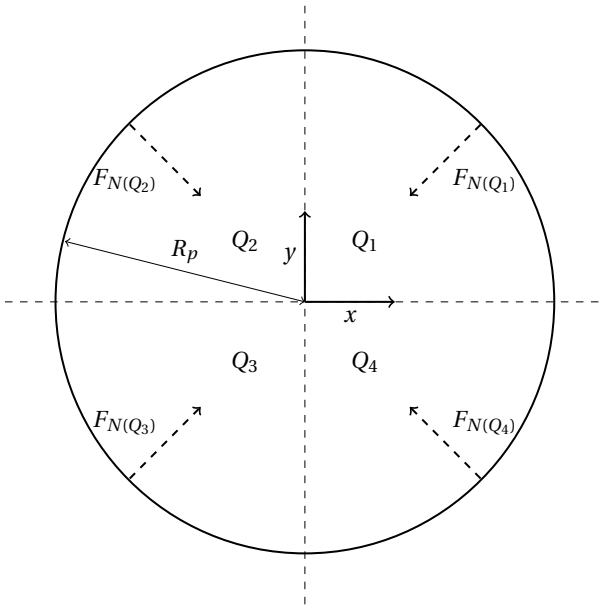

Figure 6.9: Orientation of the resulting normal force (F_N) during interaction of the particle with the pipe wall

The values for the spring constant (k_{spr}) and damper constant (c_{dmp}), in Equation 6.33, are chosen that the calculated normal force will not be greater than the normal force in the experiments of chapter 4. This is done because of the usage of the value for the material specific wear rate (k). The values are determined as $k_{spr} = 1.77 \cdot 10^{-6}$ Nm^2 for the spring constant, and $c_{dmp} = 0.7$ kg/s for the damping constant. The maximum value for δ^2, which denotes the distance between the particle boundary and the particle boundary including the spring-damper system, is chosen equal to 10^{-6} m. In order to model a very small fluid film between the particle and the wall during a collision.

6.3. Method - Calculations

In subsection 6.3.1 the numerical discretization schemes are given and explained. First, the equations of the fluid motion are discretized, whereafter the discretized particle motion equations follow. In subsection 6.3.2, the calculation of the collision forces between the particle and the pipe wall are explained. Two types of particle-wall interaction are distinguished, a collision which takes one time step and a sliding collision, which takes several consecutive time steps.

6.3.1. Numerical Discretization Schemes

First, the discretization schemes with respect to the fluid are given, which is followed by the discretization schemes of the particle motion.

Discretization with respect to the Fluid Motion

For the numerical discretization of the Navier-Stokes, different settings in OpenFOAM are used. Before the different discretization are presented, the Navier-Stokes equation is revisited here, Equation 6.3.

$$\frac{\partial \rho_f \mathbf{u}_f}{\partial t} + \nabla \cdot \left(\rho_f \mathbf{u}_f \mathbf{u}_f\right) = -\nabla p + \nabla \cdot \left(\mu \left(\nabla \mathbf{u}_f + \nabla \mathbf{u}_f^T\right)\right) + \rho_f \mathbf{g} \tag{6.3 revisited}$$

In Table 6.3 the discretization schemes are summarized, which are used by OpenFOAM (Launchbury, 2016). Further mathematical elaboration of the terms can be found for example in the OpenFOAM Extended Code Guide.

Table 6.3: Discretization schemes with respect to the fluid motion

Keyword OpenFoam	Term	Type
ddtSchemes	First and second time derivative $\left(\frac{\partial}{\partial t}, \frac{\partial^2}{\partial^2 t}\right)$	Backward
gradSchemes	Gradient (∇)	Gauss linear
divSchemes	Convection term	Gauss limitedLinear 1.0
divSchemes	Diffusion term ($\nabla\cdot$)	Gauss linear
laplacianSchemes	Laplacian terms (∇^2)	Gauss linear uncorrected
interpolationSchemes	Interpolation	Linear
snGradSchemes	Surface normal gradients	Uncorrected

In Table 6.2, the boundary conditions with respect to the flow velocity are given. The wall of the model consists of a no-slip boundary condition. As stated in subsection 6.2.1, the no-slip (or Dirichlet) boundary condition holds that the wall velocity is equal to the velocity of the fluid. The discretization of the no-slip boundary condition in x-direction, is given by Equation 6.34. Equation 6.34 is also valid for the other directions if there is a wall section present. As can be seen from Equation 6.34 it is discretized using the backward Euler method, which is done for first and second derivates regarding Table 6.3.

$$\left(\frac{\partial u_i(t)}{\partial x}\right)_{wall} = \left(\frac{u_i(t) - u_i(t-1)}{\Delta x}\right)_{wall} = 0 \tag{6.34}$$

Discretization with respect to the Particle Motion

The general equation of the particle motion in the vertical direction, without a a collision is given by Equation 6.24 and for the horizontal direction by Equation 6.26. The discretization is done by using a forward Euler method, also known as the explicit Euler method. This holds that the information of the previous time is used to calculated the next time step. The derivation of the discretization is given in Equation 6.35 for the vertical direction and Equation 6.37 for the horizontal direction. Before the discretization is given of both of the directions, first Equation 6.24 and Equation 6.26 are repeated, for clarification.

$$\left(\frac{d\,\mathbf{u}_p}{d\,t}\right) = \frac{\left(m_p - \rho_f V_p\right)\mathbf{g}}{\left(m_p + \frac{1}{2}\rho_f V_p\right)} + \frac{\frac{1}{2} C_D \rho_f A_p}{\left(m_p + \frac{1}{2}\rho_f V_p\right)} \left|\mathbf{u}_f - \mathbf{u}_p\right| \left(\mathbf{u}_f - \mathbf{u}_p\right) \tag{6.24 revisited}$$

Discretization of Equation 6.24, using the forward Euler method, results into Equation 6.35.

$$\left(\frac{\mathbf{u}_p(t) - \mathbf{u}_p(t-1)}{\Delta t}\right) = \frac{\left(m_p - \rho_f V_p\right)\mathbf{g}}{\left(m_p + \frac{1}{2}\rho_f V_p\right)} + \frac{\frac{1}{2} C_D \rho_f A_p}{\left(m_p + \frac{1}{2}\rho_f V_p\right)} \left|\mathbf{u}_f(t-1) - \mathbf{u}_p(t-1)\right| \left(\mathbf{u}_f(t-1) - \mathbf{u}_p(t-1)\right) \tag{6.35}$$

Rearranging the terms of Equation 6.35 results into Equation 6.36, which can be used to calculate the next velocity in vertical direction.

$$\mathbf{u}_p(t) = \mathbf{u}_p(t-1) + \left(\frac{\left(m_p - \rho_f V_p\right)\mathbf{g}}{\left(m_p + \frac{1}{2}\rho_f V_p\right)} + \frac{\frac{1}{2} C_D \rho_f A_p}{\left(m_p + \frac{1}{2}\rho_f V_p\right)} \left|\mathbf{u}_f(t-1) - \mathbf{u}_p(t-1)\right| \left(\mathbf{u}_f(t-1) - \mathbf{u}_p(t-1)\right)\right) \Delta t \tag{6.36}$$

For the horizontal direction, Equation 6.26 is discretized and directly rearranged, the result is given in Equation 6.37.

$$\left(\frac{d\,\mathbf{u}_p}{d\,t}\right) = \frac{\frac{1}{2} C_D \rho_f A_p}{\left(m_p + \frac{1}{2}\rho_f V_p\right)} \left|\mathbf{u}_f - \mathbf{u}_p\right| \left(\mathbf{u}_f - \mathbf{u}_p\right) \tag{6.26 revisited}$$

$$\mathbf{u}_p(t) = \mathbf{u}_p(t-1) + \left(\frac{\frac{1}{2} C_D \rho_f A_p}{\left(m_p + \frac{1}{2}\rho_f V_p\right)} \left|\mathbf{u}_f(t-1) - \mathbf{u}_p(t-1)\right| \left(\mathbf{u}_f(t-1) - \mathbf{u}_p(t-1)\right) \right) \Delta t \tag{6.37}$$

When the condition of Equation 6.30 is satisfied, the equation of motion of the particle will contain the collision term, Equation 6.23. The discretization is then given by Equation 6.38, until the condition of Equation 6.30 is no longer satisfied. The place of the collision should also be taken into account, as explained in subsection 6.2.2, therefore the last term should be added or subtracted from Equation 6.38. Again, first the equation of motion for the horizontal direction in case of particle-wall interaction is repeated, Equation 6.32.

$$\left(\frac{d\,\mathbf{u}_p}{dt}\right) = \frac{\frac{1}{2} C_D \rho_f A_p \left|\mathbf{u}_f - \mathbf{u}_p\right| \left(\mathbf{u}_f - \mathbf{u}_p\right)}{\left(m_p + \frac{1}{2}\rho_f V_p\right)} \pm \frac{\left(\frac{-k_{spr}}{\delta^2} - c_{dmp}\,\mathbf{u}_p\right)}{\left(m_p + \frac{1}{2}\rho_f V_p\right)} \tag{6.32 revisited}$$

$$\mathbf{u}_p(t) = \mathbf{u}_p(t-1) + \left(\frac{\frac{1}{2} C_D \rho_f A_p}{\left(m_p + \frac{1}{2}\rho_f V_p\right)} \left|\mathbf{u}_f(t-1) - \mathbf{u}_p(t-1)\right| \left(\mathbf{u}_f(t-1) - \mathbf{u}_p(t-1)\right) \pm \frac{\left(\frac{-k_{spr}}{\delta^2} - c_{dmp}\,\mathbf{u}_p(t-1)\right)}{\left(m_p + \frac{1}{2}\rho_f V_p\right)} \right) \Delta t \tag{6.38}$$

The normal force, given by Equation 6.33, is discretized as follows by Equation 6.39.

$$F_N = \overbrace{\frac{1}{2} C_D \rho_f A_p \left|\mathbf{u}_f - \mathbf{u}_p\right| \left(\mathbf{u}_f - \mathbf{u}_p\right)}^{F_D} \pm \overbrace{\left(\frac{-k_{spr}}{\delta^2} - c_{dmp}\,\mathbf{u}_p\right)}^{F_C} \tag{6.33 revisited}$$

$$F_N(t-1) = \frac{1}{2} C_D \rho_f A_p \left|\mathbf{u}_f(t-1) - \mathbf{u}_p(t-1)\right| \left(\mathbf{u}_f(t-1) - \mathbf{u}_p(t-1)\right) \pm \left(\frac{-k_{spr}}{\delta^2} - c_{dmp}\,\mathbf{u}_p(t-1)\right) \tag{6.39}$$

6.3.2. Normal Forces and Sliding Lengths due to Particle-Wall Interaction

The normal forces are calculated using Equation 6.33, or in the discretized form, Equation 6.39. Two types of particle-wall interaction are distinguished, a collision at a single point in time and a sliding collision which lasts several consecutive time steps. Figures containing particle-wall interactions during the simulations can be found in Appendix B.

During particle-wall interaction, whether it concerns a collision or sliding interaction, a normal force is applied. With the exertion of the normal force a wall resistance force (F_w) can be obtained, using the friction law of Coulomb. The friction law of Coulomb is given by Equation 6.40.

$$F_w = \mu_w F_N \tag{6.40}$$

In Equation 6.40, F_w represents the wall friction force and F_N the normal force. The wall friction coefficient, which is material dependent, is given by μ_w. Its value is chosen as $\mu_w = 0.36$, the kinetic friction coefficient of copper and steel[5]. Thus, with the result of the normal force, a friction force can be obtained and substituted into the force balance in vertical direction. During particle-wall interaction, the equation of motion in vertical direction is given by Equation 6.41.

$$m_p \left(\frac{d\,w_p}{dt}\right) = \left(\rho_f V_p - m_p\right) g + F_D + F_a - F_w \tag{6.41}$$

During particle-wall interaction, the DEM model is pushing the particle away from the wall. As given in Equation 6.29 the collision force is obtained from a non-linear spring-damper system. Next, using the drag force acting on the particle during the interaction, the normal force on the particle can be calculated, using Equation 6.33. In subsection 6.3.2 it is explained that two sliding cases can be distinguished. These two cases resulted into two different applied normal forces from the DEM model, Equation 6.39. First the point interaction is discussed, which is followed by a separate part about sliding interaction and its resultant normal force.

[5] Wikipedia: Friction

Point Interaction

As can be seen from Equation 6.41, the wall friction works opposite to the motion of the particle, is decelerating. Thus, the propagation in upward direction will be smaller with the friction of the wall than the propagation without the wall friction force. The difference between these two cases can be expressed as a distance. The result of this difference is taken as the sliding length. A schematically representation of this case is given by Figure 6.10, whereas Δh represents the difference in height, based on exertion of the wall friction force.

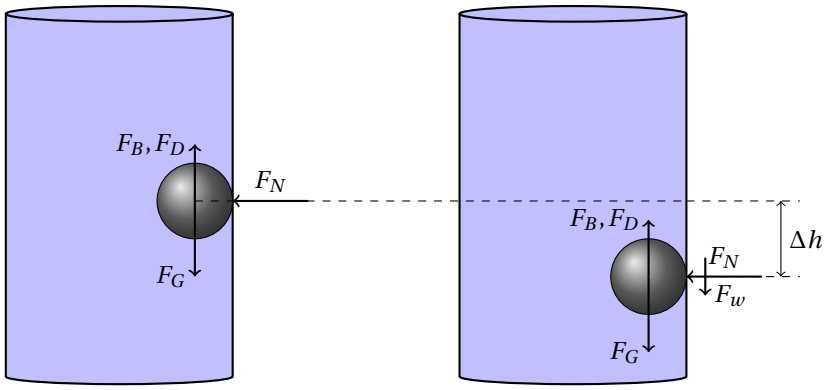

Figure 6.10: Particle collision with and without wall friction force

In case of a point interaction, the difference is height (Δh), or in fact the sliding distance due to a point interaction, is calculated using Equation 6.42. In Equation 6.42, the normal force (F_N) is obtained using Equation 6.33.

$$\Delta h = \left(\frac{F_w}{m_p}\right)(\Delta t)^2 = \left(\frac{\mu_w F_N}{m_p}\right)(\Delta t)^2 \tag{6.42}$$

In Figure 6.11, the particle velocity, obtained with and without the effect of the wall friction force, F_w, is plotted against time. The effect of Equation 6.40 can clearly be seen, the particle decelerates at $t = 0.36$ s, the time of the point interaction with the pipe wall.

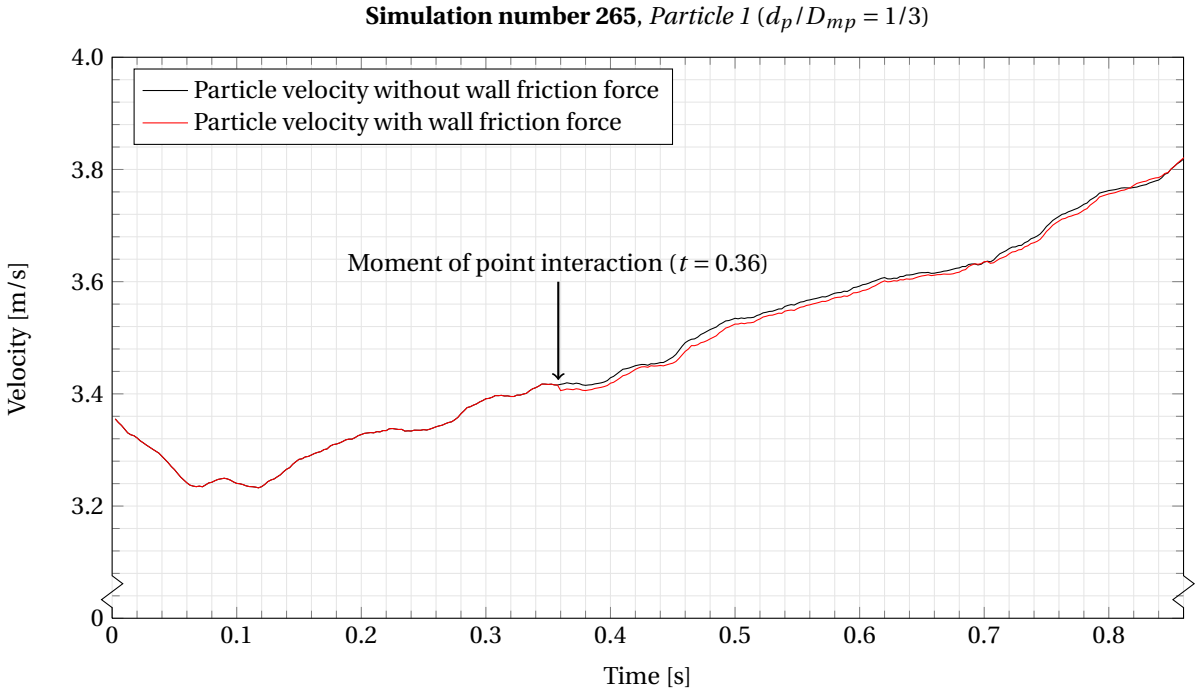

Figure 6.11: Vertical particle velocity with and without the influence of a wall friction force

In Figure 6.12, the applied normal force on *Particle 1* during a point interaction is plotted against the simulation time, whereat the duration of the point interaction is enlarged. This normal force is applied on both of the situations shown in Figure 6.11, however, as explained earlier, this normal force is not taken into account as a wall friction force in the black velocity profile. In Appendix B, section B.6, figures are shown how a point interaction between the particle and the wall appears during a simulation.

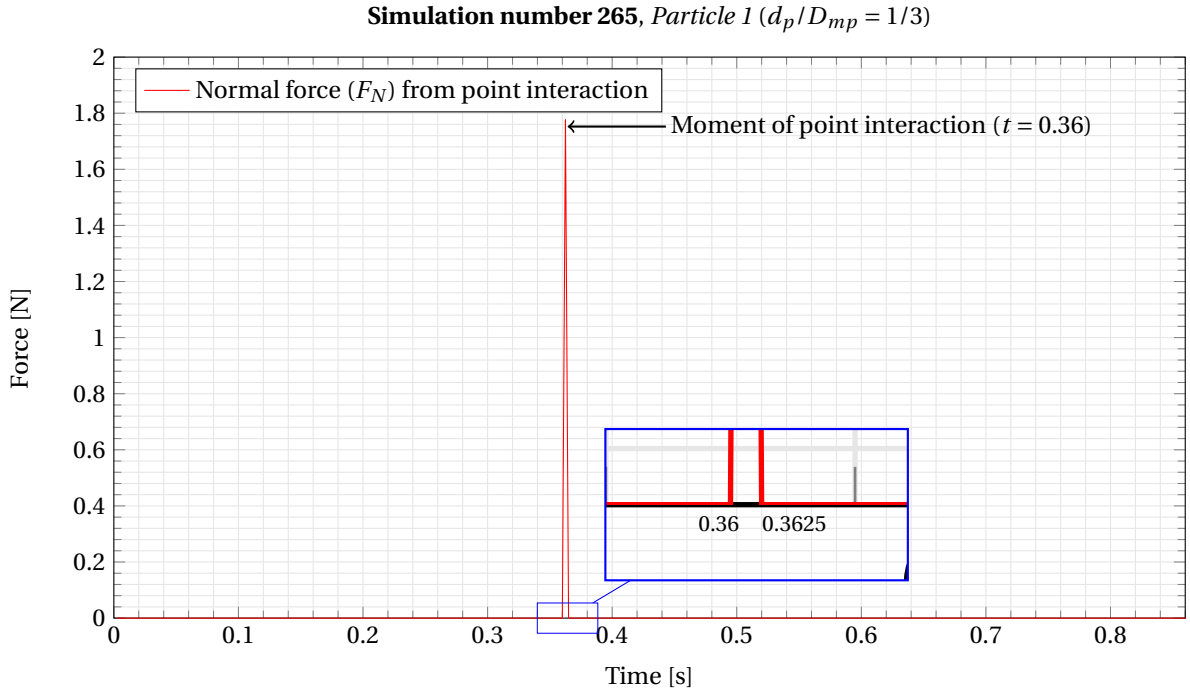

Figure 6.12: Normal force during point interaction, obtained from Equation 6.39, plotted against simulation time

Sliding Interaction

The second case, in which consecutive time steps give the sliding path, the total sliding length is given by the distance between the start and end of the consecutive time series. The sliding distance can be obtained using Equation 6.43. In Equation 6.43, $\boldsymbol{x}_i$ represents the vector containing the x-, y- and z-coordinate, respectively. The algorithm which determines whether the time steps are consecutive, is given in Appendix B, section B.5. In Figure 6.14, the sliding of a nodule against the pipe wall is schematically represented. In Figure 6.14, the darkening of the circle, which represents the spherical particle from the simulations, gives the propagation in time. In Appendix B, section B.6, other figures of both the point interaction, as the sliding particle along the pipe wall during the MATLAB simulations, can be found.

$$\begin{aligned} \Delta \boldsymbol{x}_i\,(T_{cons}) &= \boldsymbol{x}_i\,(T_{end}) - \boldsymbol{x}_i\,(T_{start}) \\ \rightarrow L_{cons} &= \sqrt{\left(\sum_{i=1}^{3} (\Delta \boldsymbol{x}_i\,(T_{cons}))^2\right)} \end{aligned} \tag{6.43}$$

In case of a point interaction with the wall Equation 6.42 is used to obtain the sliding distance, in case of sliding along the pipe wall in consecutive time steps, Equation 6.43 is used. In order to calculate the sliding distance over a set of simulations, since they will consists both interaction types, the result of Equation 6.42 will be added to the result of Equation 6.43. Thus, the total sliding length (L_{slide}), obtained during a simulation, is calculated using Equation 6.44. The second term of Equation 6.44 refers to the summation of all of the point interactions, as explained in the previous part.

$$L_{slide} = L_{cons} + \sum_{i=1}^{n} (\Delta h)_i \tag{6.44}$$

In Figure 6.13 the applied normal force during sliding, F_N, is plotted against simulation time, t. In order to express the shape of the graph, it is chosen not to plot the entire simulation time. Besides, the interaction with the wall was only in the first time steps of the simulation, thereafter the DEM criteria was not valid any longer, so the normal force became zero. In Figure 6.14 a representation of the sliding interaction between the particle and the wall can be seen.

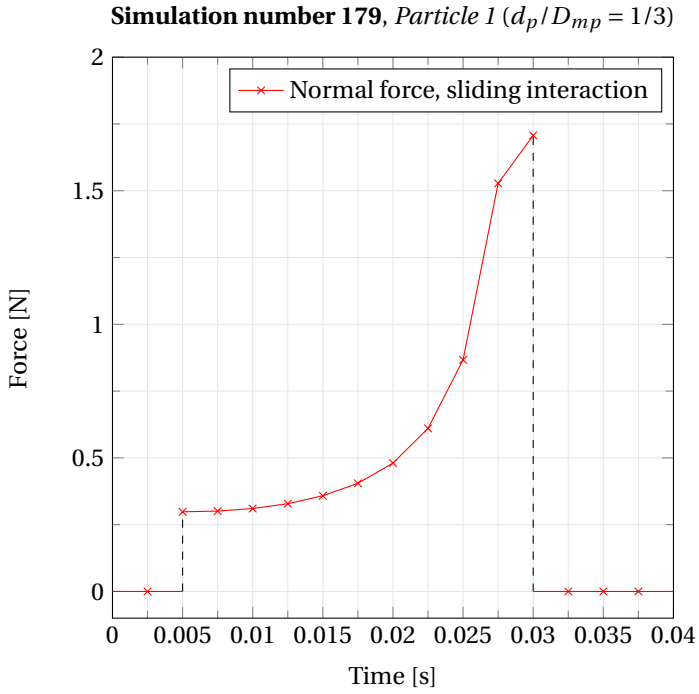

Figure 6.13: Normal force during sliding contact, obtained from Equation 6.39, plotted against simulation time

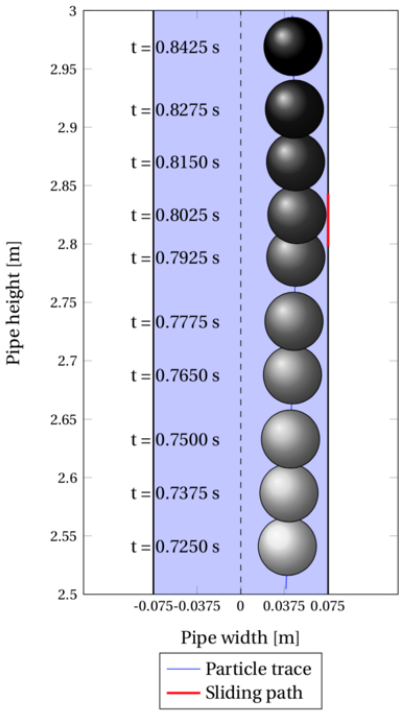

Figure 6.14: Sliding of the particle along the pipe wall

6.4. Modelling Results

An overview of the results from the CFD-DEM simulations is given in this section. First, in subsection 6.4.1 the simulations without wall contact are discussed. This is followed by subsection 6.4.2, which includes the simulations with wall contact. Next, in subsection 6.4.3, a sensitivity analysis is made. In Table 6.4 an overview of the simulations is given. Each of the 300 simulations describe an unique different starting position, determined by Equation 6.14, at the pipe inlet. The initial conditions of the particle velocity, which are equal for each simulation, are given by Equation 6.16.

Table 6.4: Results of the simulations

Symbol	Description	Unit	Value
d_p/D_{mp}	Ratio particle diameter/pipe diameter	[-]	1/3
N_{sim}	Number of simulations	[-]	300
NC_{sim}	Number of simulations with interaction	[-]	47
L_{pipe}	Total simulated pipe length	[m]	900
L_{slide}	Available sliding length	[m]	141
L_{slide}/L_{pipe}	Ratio sliding length/pipe length	[%]	15.67

6.4.1. Results I - Simulations without Wall Contact

A total number of 300 simulations are done, for a particle diameter which is equal to one-third of the pipe diameter, whereas in 253 simulations the particle did not collide with the wall. The used particle is referred to as *"Particle 1"*. The start positions of *Particle 1* are plotted in Figure 6.15 and are represented as a '+'. In Figure 6.15, the black dashed line represents the boundary which the center of the particle cannot cross. Otherwise a part of the particle would be outside of the pipe. Therefore, the distance between the wall and the particle boundary is equal to the radius of the used particle.

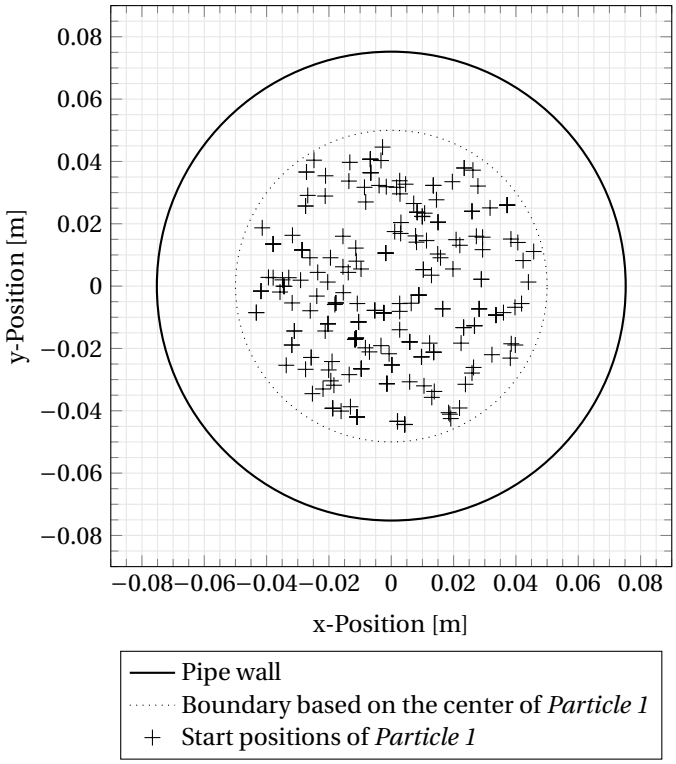

Figure 6.15: Start positions of *Particle 1* $(d_p/D_{mp} = 1/3)$ without pipe wall interaction

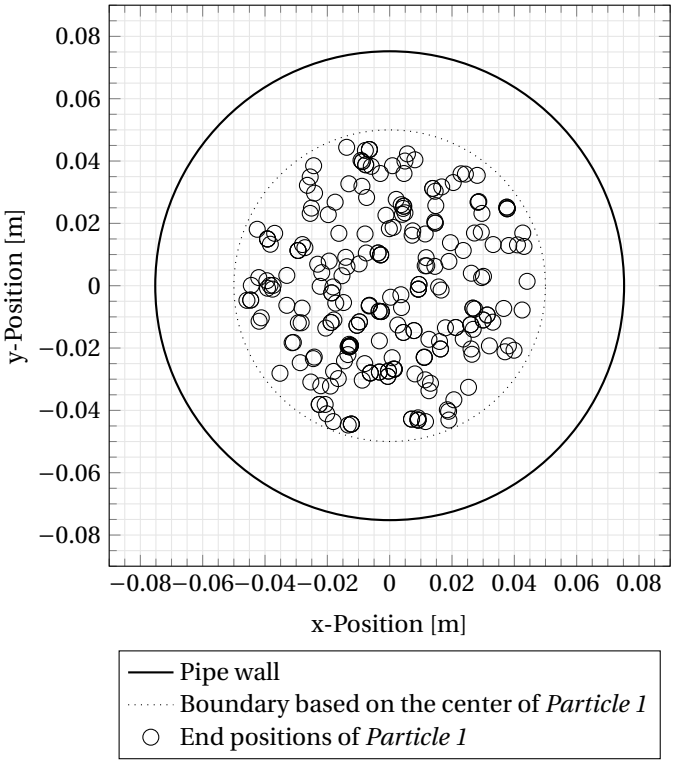

Figure 6.16: End positions of *Particle 1* $\left(d_p/D_{mp} = 1/3\right)$ without pipe wall interaction

Vlasák et al. (2014) stated that the particles migrate from the wall in a vertical pipe flow. This can also be seen in Figure 6.16, where the end positions of the single particle simulations using *Particle 1* are shown, represented by a black 'o'.

6.4.2. Results II - Simulations with Wall Contact

A total number of 300 simulations are done with *Particle 1* $\left(d_p/D_{mp} = 1/3\right)$, whereas in 47 simulations the particle did interact with the wall. In subsection 6.3.2 it is stated that two types of collisions are considered, a point interaction and a sliding interaction. However, if the particle would be in constant sliding interaction with the wall, during those 47 simulations, the sliding length would be equal to 47 times the pipe length. This results into a (maximum) sliding path of 141 meter, since the length of the pipe is 3 meter.

The total simulated length using *Particle 1* is 900 meter. If the sliding path of 141 meter is considered and compared to the total simulated length, it can be concluded that the sliding length is 15.67% of the total length. Considering a sliding distance of 141 meter and the results of Figure 4.17, the remaining nodule mass would be equal to 99.75% of its initial mass. Compared to a nodule weight of 400 grams, the mass loss due to abrasion equals 1 gram.

The total length of the VTS spans 5000 meter, so if the particle is in contact with the pipe wall for 15.67%, this would be equivalent to a sliding length of 783.5 meter. In Figure 4.17 the remaining nodule mass of plotted against the sliding distance. According to the experimental results, for a sliding distance of 783.5 meter, the remaining nodule mass would be equal to 98% of its initial mass.

However, the calculated sliding length of the model, obtained by Equation 6.44, is 3.43 meter. This length is 0.38% of the total simulated length of 900 meter. This calculated value would be equivalent to a sliding length in the VTS of 20 meter. A sliding length of this distance is hardly noticeable according to the results of the single nodule experiments. Therefore none conclusions are drawn based on the calculated sliding lengths of the model.

The start positions, whereas the particle did collide with the wall, are plotted in Figure 6.17. And in Figure 6.18 the end positions of the particle, which have had a collision can be seen.

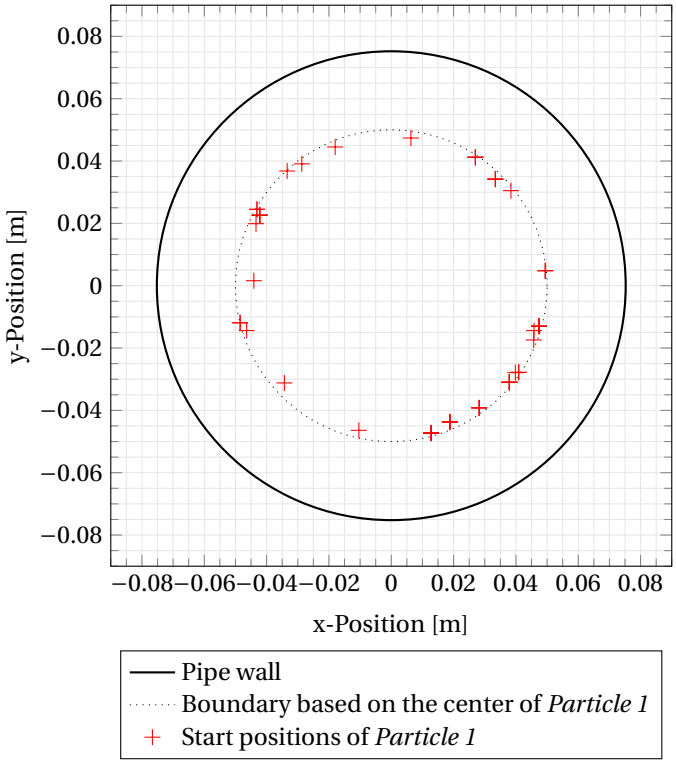

Figure 6.17: Start positions of *Particle 1* $(d_p/D_{mp} = 1/3)$ with pipe wall interaction

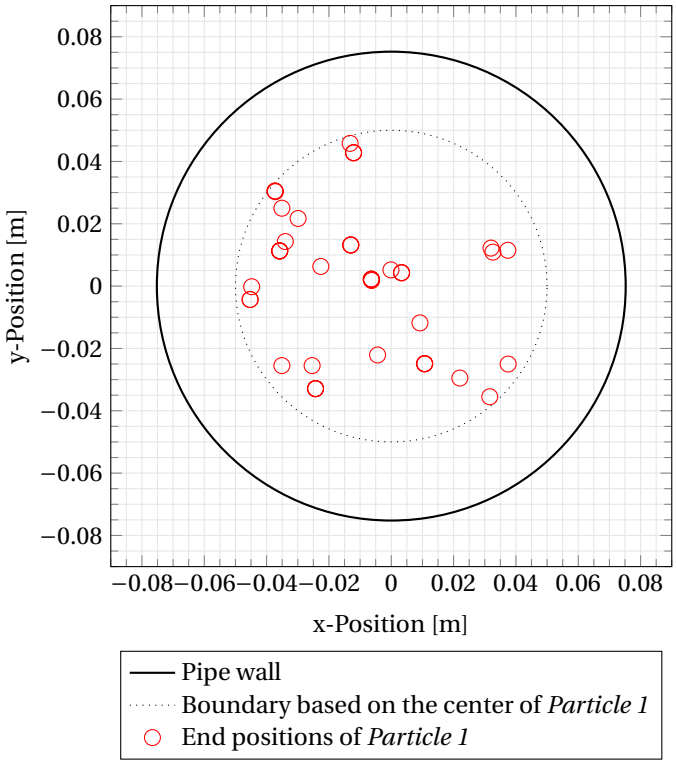

Figure 6.18: End positions of *Particle 1* $(d_p/D_{mp} = 1/3)$ with pipe wall interaction

6.4.3. Model Sensitivity Analysis

The previous simulations were done using a particle diameter being one-third of the pipe diameter ($d_p/D_{mp} = 1/3$). In this section this particle is referred to as "*Particle 1*". The next set of simulations is done using a particle diameter of one-sixth ($d_p/D_{mp} = 1/6$), which is called "*Particle 2*". The last particle, "*Particle 3*", is one-tenth ($d_p/D_{mp} = 1/10$) of the pipe diameter. The parameters used for the sensitivity analyses, related to the different particles, are summarized in Table 6.5. For each ratio the settings for the pipe flow was the same, the settings for the CFD part are given in Table 6.1. For the calculation of the settling velocity (v_t), Equation 6.15 is used, using a = 18 and b = 1.1 (Van Wijk, 2016).

Table 6.5: Parameter overview used for the sensitivity analysis of the model

Symbol	Unit	*Particle 1*	*Particle 2*	*Particle 3*
d_p/D_{mp}	[-]	1/3	1/6	1/10
d_p	[m]	0.0500	0.0250	0.0150
V_p	[m^3]	$6.55{\cdot}10^{-5}$	$8.18{\cdot}10^{-6}$	$1.77{\cdot}10^{-6}$
ρ_{part}	[kg/m^3]	1700	1700	1700
m_p	[kg]	0.1113	0.0139	0.0030
$m_{a,p}$	[kg]	0.0327	0.0041	$8.84{\cdot}10^{-4}$
C_D	[-]	0.445	0.445	0.445
$d_{p,DEM}$	[m]	0.0550	0.0275	0.0165
v_t	[m/s]	0.6447	0.4553	0.3519

The spring and damper constant, $k_{spr} = 1.77{\cdot}10^{-6}$ Nm^2 and $c_{dmp} = 0.7$ kg/s, respectively, used for *Particle 1*, cannot be applied to the smaller particle sizes. Both need to be scaled, otherwise the motion is either damped or the particle will literally shoot from the pipe wall to the other side of the pipe.

In the work of Brändle de Motta et al. (2013), equations for the spring stiffness and damping coefficient are given. The equation for the spring stiffness is given by Equation 6.45 and for the damping coefficient by Equation 6.46.

$$k_{spr} = -\frac{m_e\left(\pi^2 + [\ln(e_d)]^2\right)}{[N_c \Delta t]^2} \tag{6.45}$$

$$c_{dmp} = -\frac{2\, m_e\, [\ln(e_d)]}{[N_c \Delta t]} \tag{6.46}$$

In Equation 6.45, and also in Equation 6.46, m_e denotes the effective particle mass, which is equal to the particle mass in case of a particle-wall collision (Brändle de Motta et al., 2013). The term in the denominator ($N_c \Delta t$) represents the numerical collision duration. The collision coefficient is represented by e_d.

In order to tune the spring and damping coefficient for the sensitivity analysis, two assumptions are made. First, it is assumed that the numerical collision duration is independent of the particle size. Second, the collision coefficient for each particle size is the same. Therefore it can be concluded, that the particle mass is the only parameter which can be scaled in Equation 6.45 and Equation 6.46. Thus, the mass ratio of *Particle 2* with respect to *Particle 1*, is taken as the ratio for the spring and damping constant, for *Particle 2*. This also holds for *Particle 3*. The resulting spring and damping coefficients can be seen in Table 6.6. The sizes and dimensions of the different particles are given by Table 6.5. In Table 6.5, d_p/D_{mp} gives the ratio particle diameter/pipe diameter, k_{spr} represents the spring constant and c_{dmp} denotes the damping constant.

Table 6.6: Spring and damper constant for different particle sizes

Symbol	Unit	*Particle 1*	*Particle 2*	*Particle 3*
d_p/D_{mp}	[-]	1/3	1/6	1/10
k_{spr}	[N m^2]	1.77E-06	2.21E-07	4.78E-08
c_{dmp}	[kg/s]	0.7000	0.0875	0.0189

For both *Particle 2* as *Particle 3*, 50 simulations are done, equivalent to a total traveling distance of 150 meter per particle. The simulation showed in 7 of the 50 simulations particle-wall interaction for *Particle 2*, which coincides with a maximum sliding length of 21 meter. In Figure 6.19 the start end final positions of *Particle 2*, with particle-wall interaction, can be seen. For *Particle 3* the total number simulations with particle-wall interaction was 8, thus 24 meter of maximum sliding length. In Figure 6.20 the start end final positions of *Particle 3*, with particle-wall interaction, can be seen. The results are summarized in Table 6.7. In Table 6.7, N_{sim} represents the total number of simulations and NC_{sim} denotes the number of simulations with particle-wall interaction. Furthermore, L_{pipe} gives the total simulated length and L_{slide} represents the maximum available sliding distance.

Table 6.7: Overview of the results using different particle sizes

Symbol	Unit	Value		
d_p/D_{mp}	[-]	1/3	1/6	1/10
N_{sim}	[-]	300	50	50
NC_{sim}	[-]	47	7	8
L_{pipe}	[m]	900	150	150
L_{slide}	[m]	141	21	24
L_{slide}/L_{pipe}	[%]	15.67	14.00	16.00

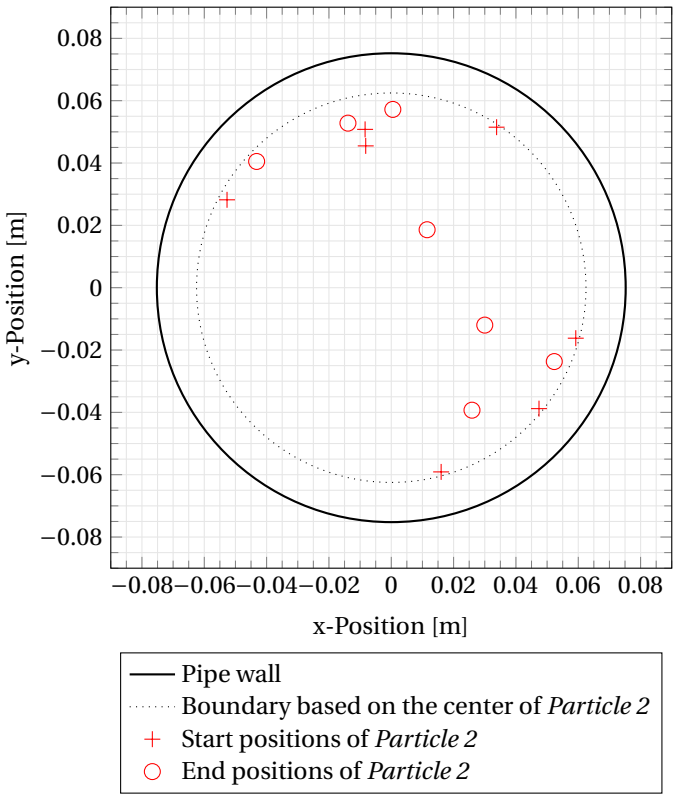

Figure 6.19: Start and end positions of *Particle 2* $(d_p/D_{mp} = 1/6)$ with pipe wall interaction

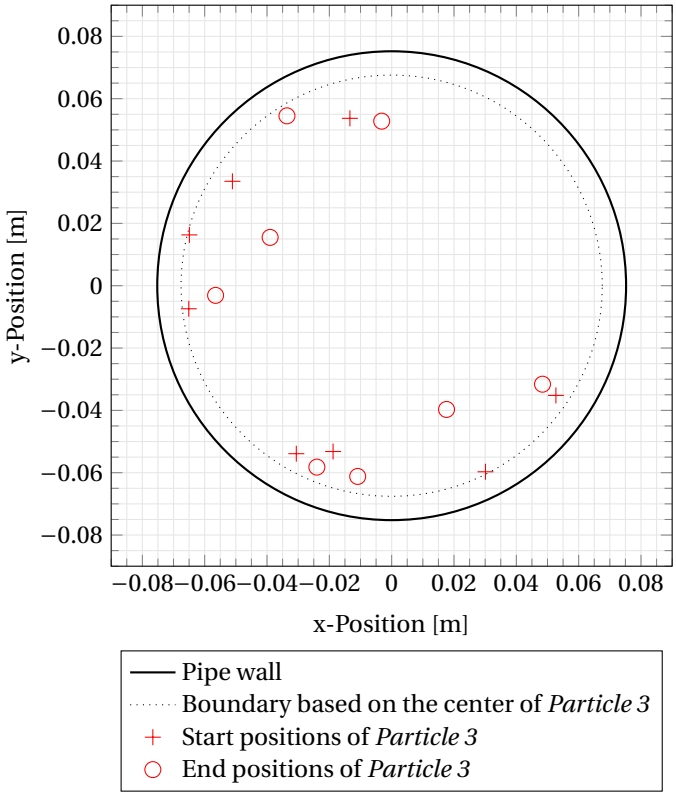

Figure 6.20: Start and end positions of *Particle 3* $(d_p/D_{mp} = 1/10)$ with pipe wall interaction

In Table 6.8 the normalized results over the total number of simulations using different d_p/D_{mp} ratios can be seen. It can be concluded from Table 6.8, that the ratio between the sliding length (L_{slide}) and the pipe length (L_{pipe}), is independent from the particle size.

Table 6.8: Normalized values of the results using different particle sizes

Symbol	Unit	*Particle 1*	*Particle 2*	*Particle 3*
d_p/D_{mp}	[-]	1/3	1/6	1/10
L_{pipe}	[m]	3	3	3
L_{slide}	[m]	0.47	0.42	0.48
L_{slide}/L_{pipe}	[-]	0.16	0.14	0.16

6.5. Discussion and Evaluation of the Model

First, the modelling assumptions and simplifications from section 6.1 are discussed. Second, the discussion on the one-way coupled model is given. This section ends with a discussion about the obtained results from the model.

Discussion on the Modelling Assumptions and Simplifications

1. The particle is a point particle and follows the flow by means of a one-way coupling (section 6.1).

   The point particle has a mass and spherical dimensions, but it only uses the information of the fluid field of the nearest grid point. A better approach might be to compute an average velocity based on all of the grid points which are 'occupied' by the particle. However, this costs much more computational time and the flow is not disturbed by the presence of the particle, thus it cannot be concluded whether this approach is indeed better.

2. The flow is incompressible, which holds a constant density during the simulations (subsection 6.2.1).

The incompressible constraint states that the density of the fluid does not change over time. Due to the fact that the particle does not change in mass during the simulations, no fine particles are created during the simulations. In real life conditions smaller particles could dissolve into the fluid, especially the clay or fine sediment content of the larger sized nodules, which could lead to a changing density of the carrier fluid. An example of a real nodule can be seen in Figure 2.12.

3. A polymetallic nodule is modeled as a sphere, thus the angularities are not taken into account. Also, the mass moment of inertia is not taken into account (subsection 6.2.1).

   Because the angularities are not taken into account, the coefficient of drag (C_D) could be chosen equal in each direction. This makes the modelling approach much simpler. Angularities could be taken into account using certain shape factors for example.

4. The acceleration of the fluid is neglected, since large gradients only exist close to the wall, at positions where the particle will not come due to its geometry (subsection 6.2.2).

   The material derivative of the fluid accounts for the fluid acceleration. The largest gradients in a turbulent pipe flow can be found close to the wall. Due to the size of the particles and its mass, they will not be influence by these gradients. Therefore the fluid acceleration, or material derivative, can be neglected.

5. The influence of the wall (wall effect) on the settling velocity of a single sphere is not taken into account (subsection 6.2.2).

   From the work of Di Felice (1996) and for example Goeree et al. (2017), the effect of the wall on the settling of a single particle, it can be concluded that there should be corrected for the presence of a wall. However, it is unclear how this effect should be incorporated in a one-way coupled model, since in two-way coupled models, if they are well constructed, this effect should happen automatically. Therefore the effect is not taken into account in this work.

6. The mass decrease of the particle due to interactions with the wall during the simulations is neglected (subsection 6.3.2).

   Although the effect of abrasive wear cause a decrease in mass, as shown by Figure 4.17, the mass loss due to sliding and/or point interaction(s) are not taken into account in the model. The maximum sliding length during a simulation is equal to the total pipe length, which is 3 meter. This would cause a negligible mass loss as shown by Figure 4.17 and therefore the mass decrease is not taken into consideration. However, if the effect is taken into account, it should be noted that the second law of Newton, as given by Equation 6.17, is not valid if the mass is not constant. An example of a variable (decreasing) mass during its motion is the take-off of a rocket.

Discussion on the One-Way Coupled CFD-DEM model

The one-way coupled CFD-DEM model is a simplified approach, but given the time this was the best solution. With the flow field data obtained by OpenFOAM and its transportation to MATLAB, many particles could be released in the flow. However, the disadvantage of this approach is that the same flow field is used and therefore is limited to its dimensions. For a new pipe flow, for a longer or wider pipe for example, a new simulation is required. The mesh script (for Gmsh), which can be found in Appendix B, is suitable to change the pipe geometry very quickly.

Discussion on the Modeling Results

The results of the model, as given in section 6.4, stated that 15% of the simulations had shown interaction with the pipe wall. However, theses results are only related to this flow field and this pipe geometry. Nothing could be stated on the scaling of this value in larger pipes or if this 15% also holds on other turbulent flow fields.

The grid size influences the CFD results. During the simulations the only one grid has been used, which can be found in Appendix B. A grid convergence study could point out the quality of the grid and whether is grid is good, or not, to generate a reliable flow field.

Another discussion point is the closure model of the Large Eddy Simulation. As stated in subsection 6.2.1, the eddies on sub-grid-scale are modeled using the *kEqn* model. The use of other sub-grid-scale models,

like the Smagorinsky (Smagorinsky, 1963) or WALE (Wall-adapting local eddy-viscosity model) (Nicoud and Ducros, 1999) models, might influence the flow field.

6.6. Conclusions and Recommendations

The following secondary research questions were formed at the beginning of this chapter:

- *What is the ratio between the sliding length of the particle against the pipe wall and the total traveling length of the particle?*
- *Does the ratio of particle diameter over pipe diameter influence the sliding length per meter pipe?*

6.6.1. Hypotheses

The following hypotheses have been formed in subsection 6.1.1.

- *Hypothesis 1:*

  The ratio between the sliding length of the particle against the pipe wall and the total traveling length would be relatively small, most of the single particles would stay in the center of the pipe flow.

  The first hypothesis has been validated. The majority of the simulations will show no collisions, was indeed valid. From the work of Vlasák et al. (2014) it is known that particles will tend away from the pipe wall, in a vertical flow.

- *Hypothesis 2:*

  The ratio particle diameter over pipe diameter does influence the sliding length, since smaller particles will follow the flow quicker than larger, heavier particles.

  The second hypothesis has been falsified. From the results of the sensitivity analysis in subsection 6.4.3, it has been seen that for each of the different used particle diameters, in 15% of the simulations there was particle-wall interaction. The available sliding length is therefore equal for each of the cases, however, the calculated length over the total available length differs. It has been noticed that with the smallest particle size more point-interactions took place, instead of sliding interaction with the pipe wall.

6.6.2. Conclusions

What is the ratio between the sliding length of the particle against the pipe wall and the total traveling length of the particle?

From Table 6.4 it can be concluded that around 15% of the simulations had interaction with the pipe wall. If this 15% is taken as a theoretical maximum for the sliding length along the wall, this would be equivalent to a section of 750 meter. Compared to the results from Figure 4.17, roughly 98% of the initial mass would remain. In case the calculated sliding length is used, which was around 1% of the total length, it would be comparable to 50 meters of sliding in the VTS. From Figure 4.17 it can be concluded that only 0.1% of the original nodule mass would be lost.

The mass loss due to abrasive wear on a single nodule, is estimated to be between 0.1% and 2% of the original nodule mass. A typical nodule mass is in the order of a 400 gram, thus the mass loss due to abrasive wear is in the order of 0.4 - 8 gram.

Does the ratio of particle diameter over pipe diameter influence the sliding length per meter pipe?

From the sensitivity analysis, using *Particle 1*, *Particle 2* or *Particle 3*, it can be concluded that the collisions appeared in 15% of the simulations, as shown in Table 6.8. This conclusion is based on the obtained flow field from OpenFOAM and this pipe geometry (and mesh). A conclusion on how this number is influenced in larger pipes, is speculative at the moment.

6.6.3. Recommendations

Fluid Modelling related Recommendations

As stated in the discussion of the model, section 6.5, the influence of sub-grid-scale models on the total turbulent flow field should be investigated. With the nominal size of the polymetallic nodules, the effect of using a different model might be negligible, however, it is not investigated in this work.

It is also recommended to run longer simulations, the flow simulation in this work was only one second. It should be noted that this will take a lot of computational time and space, since the simulation of one second already took roughly 200 GB of data storage.

Particle Modelling related Recommendations

In this work, as stated in section 6.1, modelling of the polymetallic nodules in the simulations has been done as spheres. For further research, it is recommended to take the irregular shapes of the nodules into account. Zhong et al. (2016), did research on DEM/CFD-DEM modelling of non-spherical particulate systems. Another method could be, via for example an immersed boundary condition (Goeree et al., 2017). Using this method would imply that a complete CFD model can be used, whereas the fluid and solid part are coupled.

It is also recommended to investigate the DEM model better. In this work the spring-damper system is tuned on the results of the experiments. Further research must point out how to adapt the spring-damper system to the physical properties of a polymetallic nodule for example.

Furthermore, the step towards a model with extra particles added instead of a single particle should be made. When multiple particles are used, include the effect of hindered settling. This could be calculated with the equation of (Richardson and Zaki, 1954) for example.

7

Conclusions and Recommendations

Before the conclusions and recommendations are given in section 7.1 and section 7.2, respectively, the secondary research questions, which are sorted per chapter, are summarized here.

- Analysis - Polymetallic Nodules from the Clarion-Clipperton Zone (chapter 2):
  - *What causes the renewed interest of deep sea mining of polymetallic nodules?*
  - *How come that the Clarion-Clipperton Zone is so suitable for deep sea mining purposes?*
- Theory - Degradation of Brittle Agglomerates (chapter 3):
  - *Which types of wear mechanisms could be encountered during slurry transport?*
  - *How can particle degradation be quantified?*
  - *What is the effect of wear mechanisms on brittle agglomerates?*
- Scale Model Experiments I - Degradation of a Polymetallic Nodule (chapter 4):
  - *Is the equation of Archard applicable for polymetallic nodule degradation due to abrasive wear?*
  - *Does the sliding velocity influence the degradation due to abrasive wear?*
- Scale Model Experiments II - Degradation of a Batch of Polymetallic Nodules (chapter 5):
  - *Is the equation of Archard applicable to quantify the degradation due to abrasion for a batch of nodules?*
  - *Until what extent does polymetallic nodule degradation propagate?*
- Modelling - Single Particle in a Vertical Turbulent Pipe Flow (chapter 6):
  - *What is the ratio between the sliding length of the particle against the pipe wall and the total traveling length of the particle?*
  - *Does the ratio of particle diameter over pipe diameter influence the sliding length per meter pipe?*

7.1. Conclusions

Analysis - Polymetallic Nodules from the Clarion-Clipperton Zone

The Clarion-Clipperton Zone has a nodule abundance of 15 kg/m^2, which makes it the most abundant region in the world. With the increasing demand of mineral resources the coming years, this area will become very interesting. For example the rising demand for cobalt, as shown in Figure 1.2. The coming years cobalt becomes more valuable because of its unique properties and its applicability in many modern applications (Shedd et al., 2017). The total amount of nodules in the CCZ is estimated to be 21 billions of tons (ISA, 2010). With this estimation the ISA concluded that the amount of cobalt could be 0.05 billion tons, which should be enough to satisfy the growing demand for the coming years.

Theory - Degradation of Brittle Agglomerates

Four different failure mechanisms are responsible for particle degradation during slurry transport: abrasion, attrition, chipping and fragmentation. Each mechanism is an effect of the exertion of a force in a specific direction. In this research particle degradation is quantified as an effect of abrasive wear. This done by means of the equation of Archard (Archard, 1953). Brittle agglomerates, as the name states, are soft materials. For polymetallic nodules the hardness varies between the 1-4 Moh (Mero, 1965). According to Van den Berg and Alvarez Grima (2006) it is likely that materials with a hardness of less than 5, are more effected by abrasive wear than impact wear.

Scale Model Experiments I - Degradation of a Polymetallic Nodule

The degradation experiments using a single nodule showed that the equation of Archard (1953) can be used to assign the effect of abrasive wear to nodule degradation. A value for the material specific wear rate (k) of polymetallic nodules was obtained. With these results it is concluded that the remaining mass of a single nodule is 97%, in the worst case, after a sliding length of 1000 meters. It should be stated that these conclusions are drawn using polymetallic nodules from the Clarion-Clipperton Zone and with the Abrasive Wear Tester, the experimental setup in the MTI laboratory.

Scale Model Experiments II - Degradation of a Batch of Polymetallic Nodules

In an abandoned mineshaft in Freiberg, degradation experiments using polymetallic nodules from the Clarion-Clipperton Zone are conducted bij IHC MTI. The results of these tests are mimicked in the Abrasive Wear Tester at the MTI laboratory. Results showed that the degradation in the experimental setup in Kinderdijk was stronger than compared to the results of the degradation experiments in Freiberg. This was an expected result since the Freiberg tests are done in a vertical orientated setup, whilst the setup in Kinderdijk was horizontally orientated. A production of fine material was clearly seen when an initial Particle Size Distribution is compared to the distribution after a test run. It can be concluded that, due to particle-particle interaction, the equation of Archard (1953) with a specific wear rate determined by single nodule degradation experiments, is not entirely applicable to quantify degradation due to abrasion using a batch of nodules.

Modelling - Single Particle in a Vertical Turbulent Pipe Flow

A one-way coupled CFD-DEM model is made to simulate a single particle in a vertical turbulent pipe flow. The one-way coupling between the flow and the particle holds that the flow has influence on the motions of the particle, but not on the contrary. OpenFOAM was used to obtain the results for the pipe flow. When a particle was released in the pipe flow two types collisions are distinguished, a point interaction and sliding interaction. The sum of these interactions is taken to obtain the total sliding length per meter pipe. With the DEM model normal forces are obtained from the collisions, which can be substituted, together with the obtained sliding distance and the experimentally determined specific wear rate (k), in the equation of Archard (1953). After 300 simulations, which is equivalent to a particle path of 900 meter, using a particle size which equals one-third of the pipe diameter, it can be concluded that 15% of the simulations had a interaction with the wall. This results was also seen in the simulations which used a particle diameter of one-sixth and one-tenth of the pipe diameter. The 15% can be seen as a maximum sliding length, since this would indicate that a nodule is continuously at the wall, which is not representative since particles will tend migrate from the wall (Vlasák et al., 2014). With this 15% sliding length of the total pipe length an upper boundary is set. Comparing the calculated length from the model with the results of the single nodule experiments, the mass loss would be 0.5%, comparable to a few grams of an average nodule.

7.2. Recommendations

Analysis - Polymetallic Nodules from the Clarion-Clipperton Zone

During the experiments at the MTI laboratory, it became clear that polymetallic nodules are very brittle. With the sieving of the nodules many nodules broke on the sieve. Especially with the dry nodules from the furnace, for the density measurements, caution is required. It appeared that the nodules, once dried out, had lost their strength. Therefore caution is required when working with (dried) polymetallic nodules.

Theory - Degradation of Brittle Agglomerates

It is recommended to perform research while using polymetallic nodules from the zone which is considered to mine in the future. Lessons could be learned from degradation research of other materials, however, the best insight in the degradation behaviour is provided using the desired material.

In order to quantify particle degradation due to abrasive wear, it is recommended that other wear mechanisms are excluded as good as possible. Pumps and bends in experimental setups resulted into impact (fragmentation) wear on particles. For testing the effect of abrasive wear, pumps and bends should not be present in an experimental setup.

Scale Model Experiments I - Degradation of a Polymetallic Nodule

The experiments resulted into a material specific wear rate (k), inside the Abrasive Wear Tester, and it has proven a linear degradation trend during the experiments. However, it is interesting to research the effect of bends for example on this value for k. When using crushed nodules they are less susceptible to impact wear, so abrasive wear should then prevail and the value could be compared.

When testing the behaviour of degradation on polymetallic nodules, it is strongly recommended to work with real manganese nodules. This should give the best insight in the degradation processes. It is also recommended to exclude the effect of other wear mechanisms as good as possible.

Scale Model Experiments II - Degradation of a Batch of Polymetallic Nodules

During the sieving analysis of the fine material after the batch experiments, it was seen that there were a lot of clay particles present. It is recommended to do a chemical analyses of the fractions under the 63 μm to indicate the clay content versus polymetallic nodule content. In the MTI laboratory the smallest sieve size was 38 μm, it is recommended to analyze this fraction with more sieves.

For further batch experiments it would be interesting to see the effect of degradation due to abrasion on a narrow PSD. For example a PSD with only one sieve size, like Van Laarhoven (2010) did using only particles of 1.4 mm. Using different PSD curves and compare the effect of abrasive wear on these curves could also result in valuable information, is the cumulative production of fines of each of the curves comparable, or completely different.

Modelling - Single Particle in a Vertical Turbulent Pipe Flow

In this model several assumptions and simplifications are used. For the single nodule simulations it is therefore recommended to extend the model with the wall effect (Di Felice, 1996). Also, the acceleration of the fluid is not taken into account in the coupling, although these large gradients are only exists close to the wall, for some particles not available due to their size, but for the smaller particles it might lead to extra particle-wall collisions. Furthermore, particles are modeled as a point-particle, which could also be adapted using an immersed boundary method for example, as shown by Goeree et al. (2017). The particles are modeled as a sphere, although the polymetallic nodules are rather angular. Angularities of the nodules will not only affect the flow dynamics, but also the particle dynamics. Therefore, the effect of angularities on particle movements in a flow should be researched.

The model could be extended to a two-way coupled model, whereas the particle has influence on the flow. Also, the simulations of this Master Thesis were done using single particles, whilst simulations using multiple particles are closer to reality. DEM models could be used to obtain the forces of particle-particle interactions, as done now for the particle-wall interaction. It is also recommended to do more research on the spring and damper constant used in the model. Research should point out if these values be related towards the material properties of polymetallic nodules.

It is further recommended to research the scaling of the results from the simulations. In the sensitivity analysis different particle - pipe diameter ratios are tested, but a longer pipe is not considered. It is interesting to see what a longer pipe flow does to the 15% particle-wall collisions.

Bibliography

J.F. Archard. Contact and Rubbing of Flat Surfaces. *Journal of Applied Physics*, 24(3):981–988, 1953. ISSN 0021-8979. doi: 10.1063/1.1721448.

E. Baker and Y. Beaudoin. *Deep Sea Minerals: Manganese Nodules, a physical, biological, environmental, and technical review.* 2013. ISBN 9788277011202.

G.N. Baturin. *The Geochemistry of Manganese and Manganese Nodules in the Ocean*, volume 2. 1987. ISBN 978-94-010-8167-2. doi: 10.1007/978-94-009-3731-4. URL http://link.springer.com/10.1007/978-94-009-3731-4.

W.J. Beekman. *Measurements of the Mechanical Strength of Granules and Agglomerates.* PhD thesis, Delft University of Technology, 2000.

F.K. Benra, H.J. Dohmen, J. Pei, S. Schuster, and B. Wan. A Comparison of One-Way and Two-Way Coupling Methods for Numerical Analysis of Fluid-Structure Interactions. *Journal of Applied Mathematics*, 2011. ISSN 1110757X. doi: 10.1155/2011/853560.

J.C. Brändle de Motta, W.P. Breugem, B. Gazanion, J.L. Estivalezes, S. Vincent, and E. Climent. Numerical modelling of finite-size particle collisions in a viscous fluid. *Physics of Fluids*, 25(8):1–9, 2013. ISSN 10706631. doi: 10.1063/1.4817382.

J.T. Burwell. Survey of Possible Wear Mechanisms. *Wear*, 1(2):119–141, 1957. ISSN 00431648. doi: 10.1016/0043-1648(57)90005-4.

S.E. Calvert and D.S. Cronan. Geochemistry of Oceanic Ferromanganese Deposits. *Philosophical Transactions of the Royal Society of London*, 290(1366):43–73, 1978.

L.S. Caretto, A.D. Gosman, S.V. Patankar, and D.B. Spalding. Two Calculation Procedures for Steady, Three-Dimensional Flows with Recirculation. *Proceedings of the Third International Conference on Numerical Methods in Fluid Mechanics*, 19:60–68, 1973. doi: 10.1007/BFb0112677. URL http://www.springerlink.com/index/10.1007/BFb0112677.

R. Courant, K.O. Friedrichs, and H. Lewy. Uber die Partiellen Differenzgleichungen der Mathematischen Physik. *Mathematische Annalen*, 100:32–74, 1928. doi: 10.1007/BF01448839. URL https://doi.org/10.1007/BF01448839.

D.S. Cronan. Overview of Mineral Resources in the EEZ. In *Ocean Resources: Assessment and Utilisation*, volume 1, pages 105–111. Springer Netherlands, 1990. ISBN 9789400921313. doi: 10.1007/978-94-009-2131-3. URL https://doi.org/10.1007/978-94-009-2131-3{_}8.

P.A. Cundall and O.D.L. Strack. A discrete numerical model for granular assemblies. *Géotechnique*, 29(1):47–65, 1979. ISSN 0016-8505. doi: 10.1680/geot.1979.29.1.47. URL http://www.icevirtuallibrary.com/doi/10.1680/geot.1979.29.1.47.

S.J. Dasselaar, E. De Hoog, S.C.W. De Jong, J. Van Stappen, T. Mueller, J.M. Van Wijk, W.B.A. Boomsma, and R. Rotterveel. Development and demonstration of a test setup for large scale slurry transport tests (D6.21). Technical report, IHC MTI (Blue Mining), 2018a.

S.J. Dasselaar, E. De Hoog, S.C.W. De Jong, J. Van Stappen, T. Mueller, J.M. Van Wijk, and R. Rotterveel. Development and demonstration of a test setup for large scale slurry transport tests (D5.52). Technical report, IHC MTI (Blue Mining), 2018b.

E. De Hoog. *Coarse Particle Slurry Flow in Inclined Pipes and Vertical S-bends.* MSc thesis, Delft University of Technology, 2016.

E. De Hoog. Preliminary nodule PSD from Freiberg experiments. *IHC MTI B.V. Memo (M18-037)*, 2018.

R. Di Felice. A relationship for the wall effect on the settling velocity of a sphere at any flow regime. *International Journal of Multiphase Flow*, 22(3):527–533, 1996. ISSN 03019322. doi: 10.1016/0301-9322(96)00004-3.

I. Dreiseitl. About Geotechnical Properties of the Deep Seabed Polymetallic Nodules. In 18^{th} *International Conference on Transport and Sedimentation of Solid Particles*, pages 67–74. 11-15 September 2017, Prague, Czech Republic, 2017. ISBN 9788377172698.

I. Dreiseitl and A. Kondratenko. Geotechnical research in the exploration area of interoceanmetal joint organization. In *Deep Sea Minerals and Mining 3 International Conference*, 4-8 June 2012, VNIIOkeangeologia St. Petersburg, Russia, 2012.

S. Ebara, H. Takamura, H. Hashizume, and H. Yamano. Characteristics of flow field and pressure fluctuation in complex turbulent flow in the third elbow of a triple elbow piping with small curvature radius in three-dimensional layout. *International Journal of Hydrogen Energy*, 41(17):7139–7145, 2016. ISSN 03603199. doi: 10.1016/j.ijhydene.2016.02.068. URL http://dx.doi.org/10.1016/j.ijhydene.2016.02.068.

R.I. Ferguson and M. Church. A Simple Universal Equation for Grain Settling Velocity. *Journal of Sedimentary Research*, 74(6):933–937, 2004. URL http://dx.doi.org/10.1306/051204740933.

G.P. Glasby. *Marine Manganese Deposits*. Elsevier, 1977. ISBN 0444415246.

J.C. Goeree. *Drift-flux modeling of hyper-concentrated solid-liquid flows in dredging applications*. PhD thesis, Delft University of Technology, 2018.

J.C. Goeree, G.H. Keetels, and C. Van Rhee. Particle settling using the Immersed Boundary Method. In 18^{th} *International Conference on Transport and Sedimentation of Solid Particles*, pages 81–88. 11-15 September 2017, Prague, Czech Republic, 2017.

P. Halbach, M. Özkara, and J. Hense. The influence of metal content on the physical and mineralogical properties of pelagic manganese nodules. *Mineralium Deposita*, 10(4):397–411, 1975. ISSN 00264598. doi: 10.1007/BF00207897.

J.R. Hein. Prospects for Rare Earth Elements From Marine Minerals. *International Seabed Authority*, (February):2–5, 2012.

J.R. Hein, F. Spinardi, N. Okamoto, and K. Mizell. Critical metals in manganese nodules from the Cook Islands EEZ, abundances and distributions. *Ore Geology Reviews*, 68:97–116, 2015. ISSN 0169-1368. doi: 10.1016/j.oregeorev.2014.12.011. URL http://www.sciencedirect.com/science/article/pii/S0169136814003679.

C. Hirsch. *Numerical Computation of Internal & External FLows*. Elsevier, second edition, 2007. ISBN 9780750665940.

T. Holzmann. *Mathematics, Numerics, Derivations and OpenFOAM®*. Leoben, fourth edition, 2017. doi: 10.13140/RG.2.2.27193.36960. URL www.holzmann-cfd.de.

I. Hutchings and P. Shipway. Tribology. In *Tribology - Friction and Wear of Engineering Materials*, pages 165–236. Elsevier Ltd., 2 edition, 2017. ISBN 0301-679X. doi: 10.1016/S0301-679X(98)00079-6. URL http://dx.doi.org/10.1016/B978-0-08-100910-9.00006-4.

ISA. A geological model of polymetallic nodule deposits in the Clarion Clipperton Fracture zone. *International Seabed Authority*, 2010. ISSN 13514180. doi: 10.1007/s13398-014-0173-7.2.

R.I. Issa. Solution of the Implicitly Discretised Fluid Flow Equations by Operator-Splitting. *Journal of Computational Physics*, 62(1):40–65, 1986. ISSN 10902716. doi: 10.1016/0021-9991(86)90099-9.

C. Kloss, C. Goniva, A. Hager, S. Amberger, and S. Pirker. Models, algorithms and validation for opensource DEM and CFD-DEM. *Progress in Computational Fluid Dynamics, An International Journal*, 12(2/3):140–152, 2012. ISSN 1468-4349. doi: 10.1504/PCFD.2012.047457. URL http://www.inderscience.com/link.php?id=47457.

D.R. Launchbury. *Unsteady Turbulent Flow Modelling and Applications*. Springer Vieweg, Horw, Switzerland, 2016. ISBN 9783658119119. doi: 10.1007/978-3-658-11912-6.

Y. Ling, M. Parmar, and S. Balachandar. A scaling analysis of added-mass and history forces and their coupling in dispersed multiphase flows. *International Journal of Multiphase Flow*, 57:102–114, 2013. ISSN 03019322. doi: 10.1016/j.ijmultiphaseflow.2013.07.005. URL http://dx.doi.org/10.1016/j.ijmultiphaseflow.2013.07.005.

V. Marchig and P. Halbach. Internal Structures of Manganese Nodules Related to Conditions of Sedimentation. *TMPM Tschermaks Mineralogische und Petrographische Mitteilungen*, 30(2):81–110, 1982. ISSN 00413763. doi: 10.1007/BF01082497.

M.R. Maxey and J.J. Riley. Equation of motion for a small rigid sphere in a nonuniform flow. *Physics of Fluids*, 26(4):883–889, 1983. ISSN 10706631. doi: 10.1063/1.864230.

J.L. Mero. *The Mineral Resources of the Sea*, volume 1. Elsevier, 1965. ISBN 9780444403940. doi: 10.1016/S0422-9894(08)70767-0.

S.A. Miedema. *The Delft Sand, Clay and Rock Cutting Model*. IOS Press BV, 3rd edition, 2015a. ISBN 978-94-6186-537-3.

S.A. Miedema. *OE4607 Introduction Dredging Engineering. MSc Offshore & Dredging Engineering Delft University of Technology*. 2015b. ISBN 978-94-6186-536-6. doi: 10.13140/RG.2.1.2643.2488.

R. Mukhopadhyay, A.K. Ghosh, and S.D. Iyer. Manganese Nodules and Crusts. In *The Indian Ocean Nodule Field*, chapter 6. second edition, 2018. ISBN 9780128054741. doi: 10.1016/B978-0-12-805474-1.00006-3.

E.A. Munts, S.J. Dasselaar, H. Bugdayci, J.C. Goeree, and C. Van Rhee. Numerical investigation of sand-water mixture behavior in a centrifugal dredge pump. *Hydrotransport*, (19):29–41, 2014.

J. Murray and A.F. Renard. Report on deep-sea deposits based on the specimens collected during the voyage of the h.m.s. challenger in the years 1872-1876. Technical report, 1876. URL https://archive.org/details/reportonscientif02grearich.

F. Nicoud and F. Ducros. Subgrid-scale modelling based on the square of the velocity gradient tensor. *Flow, Turbulence and Combustion*, (62):183–200, 1999.

F.T.M. Nieuwstadt, B.J. Boersma, and J. Westerweel. *Turbulence: Introduction to Theory and Applications of Turbulent Flows*. Springer, 2016. ISBN 9783319315997. doi: 10.1007/978-3-319-31599-7.

M. Nimmo. Clarion-Clipperton Zone Project, Pacific Ocean. Technical report, Tonga Offshore Mining Limited, 2013.

M. Petrica, C. Katsich, E. Badisch, and F. Kremsner. Study of abrasive wear phenomena in dry and slurry 3-body conditions. *Tribology International*, 64:196–203, 2013. ISSN 0301679X. doi: 10.1016/j.triboint.2013.03.028. URL http://dx.doi.org/10.1016/j.triboint.2013.03.028.

R. Pitchumani, O. Zhupanska, G.M.H. Meesters, and B. Scarlett. Measurement and characterization of particle strength using a new robotic compression tester. *Powder Technology*, 143-144:56–64, 2004. ISSN 00325910. doi: 10.1016/j.powtec.2004.04.007.

S.B. Pope. *Turbulent Flows*. Cambridge University Press, Cambridge, 2000. ISBN 9780511840531. doi: 10.1088/0957-0233/12/11/705.

J.F. Richardson and W.N. Zaki. Sedimentation and fluidisation: Part i. *Trans. Instn. Chem. Engrs.*, 32:S82–S100, 1954. ISSN 02638762. doi: 10.1016/S0263-8762(97)80006-8. URL http://linkinghub.elsevier.com/retrieve/pii/S0263876297800068.

K.B. Shedd, E.A. Mccullough, and D.I. Bleiwas. Global trends affecting the supply security of cobalt. *Mining Engineering Magazine*, (December):37–42, 2017. ISSN 00265187.

N.S. Skornyakova and I.O. Murdmaa. Local Variations in Distribution and Composition of Ferromanganese Nodules in the Clarion-Clipperton Nodule Province. *Marine Geology*, 103(1-3):381–405, 1992. ISSN 00253227. doi: 10.1016/0025-3227(92)90028-G.

J. Smagorinsky. General circulation experiments with the primitive equations i. the basic experiment. *Monthly Weather Review*, 91(3):99–164, 1963.

G.W. Stachowiak and A.W. Batchelor. *Engineering Tribology (Fourth Edition)*. 4^{th} edition, 2014. ISBN 978-0-12-397047-3. doi: 10.1016/B978-0-12-397047-3.00011-4. URL http://linkinghub.elsevier.com/retrieve/pii/B9780123970473000114.

Y. Tsuji, T. Kawaguchi, and T. Tanaka. Discrete particle simulation of two-dimensional fluidized bed. *Powder Technology*, (77):79–87, 1993. ISSN 00325910. doi: 10.1016/0032-5910(93)85010-7.

A. Usui. Regional variation of manganese nodule facies on the Wake-Tahiti transect: Morphological, chemical and mineralogical study. *Marine Geology*, 54(1-2):27–51, 1983. ISSN 00253227. doi: 10.1016/0025-3227(83)90007-5.

A. Van Beek. *Advanced engineering design - Lifetime performance and reliability*. Delft, 5^{th} edition, 2012. ISBN 978-90-810406-1-7.

C.H. Van den Berg and M.G. Alvarez Grima. Effects of Degradation on Slurry Performance. In 13^{th} *International Conference on Transport and Sedimentation of Solid Particles*, pages 39–47. 18-20 September 2006, Tbilisi, Georgia, 2006.

E.R. Van Driest. On Turbulent Flow Near a Wall. *Journal of the Aeronautical Sciences*, 23(11):1007–1011, 1956. ISSN 1936-9956. doi: 10.2514/8.3713. URL http://arc.aiaa.org/doi/10.2514/8.3713.

B. Van Laarhoven. *Breakage of agglomerates*. PhD thesis, Technical University Delft, 2010.

J.M. Van Wijk. *Vertical Hydraulic Transport for deep sea mining*. PhD thesis, Delft University of Technology, 2016.

J.M. Van Wijk. The Influence of Nodule Degradation on the Vertical Hydraulic Transport of Manganese Nodules. In 18^{th} *International Conference on Transport and Sedimentation of Solid Particles*, pages 385–392. 11-15 September 2017, Prague, Czech Republic, 2017. ISBN 9788377172698.

P.N.W. Verhoef. *Wear of rock cutting tools: Implications for the site investigation of rock dredging projects*. PhD thesis, 1997.

S. Verichev, V. Drobadenko, N. Malukhin, A. Vilmis, P. Lucieer, J. Heeren, and B. Van Doesburg. Assessment of Different Technologies for Vertical Hydraulic Transport in Deep Sea Mining Applications. In *31$ˆ{st}$ International Conference on Ocean, Offshore and Artic Engineering*, June 10-15, 2012, Rio de Janeiro, Brazil, 2012. ISBN 978-0-7918-4490-8. doi: 10.1115/OMAE2012-83156. URL http://proceedings.asmedigitalcollection.asme.org/proceeding.aspx?doi=10.1115/OMAE2012-83156.

H.K. Versteeg and W. Malalasekera. *An Introduction to Computational Fluid Dynamics, The Finite Volume Method*. Prencite Hall, London, 1995. ISBN 0-470-23515-2. doi: 10.2514/1.22547.

P. Vlasák, Z. Chára, J. Krupička, and J. Konfršt. Experimental investigation of coarse particles-water mixture flow in horizontal and inclined pipes. *Journal of Hydrology and Hydromechanics*, 62(3):241–247, 2014. ISSN 0042-790X. doi: 10.2478/johh-2014-0022. URL http://www.degruyter.com/view/j/johh.2014.62.issue-3/johh-2014-0022/johh-2014-0022.xml.

P. Vlasák, Z. Chára, J. Konfršt, and J. Krupička. Experimental investigation of coarse particle conveying in pipes. *EPJ Web of Conferences*, 92:02111, 2015. ISSN 2100-014X. doi: 10.1051/epjconf/20159202111. URL http://www.epj-conferences.org/10.1051/epjconf/20159202111.

U. Von Stackelberg. Growth history of manganese nodules and crusts of the Peru Basin. *Geological Society, London, Special Publications*, 119(1):153–176, 1997. ISSN 0305-8719. doi: 10.1144/GSL.SP.1997.119.01.11. URL http://sp.lyellcollection.org/lookup/doi/10.1144/GSL.SP.1997.119.01.11.

A.V. Wegorzewski and T. Kuhn. The influence of suboxic diagenesis on the formation of manganese nodules in the Clarion Clipperton nodule belt of the Pacific Ocean. *Marine Geology*, 357:123–138, 2014. ISSN 00253227. doi: 10.1016/j.margeo.2014.07.004. URL http://dx.doi.org/10.1016/j.margeo.2014.07.004.

K.C. Wilson. A unified physically-based analysis of solid-liquid pipeline flow. In *Proceedings Hydrotransport*, volume 4, pages 1–16, Cranfield, UK, 1976.

R.C. Worster and D.F. Denny. Hydraulic Transport of Solid Material in Pipes. pages 563–586, 1955.

J. Zenhorst. *Degradation of Poly-Metallic Nodules in a Dredge Pump*. MSc thesis, Delft University of Technology, 2016.

W. Zhong, A. Yu, X. Liu, Z. Tong, and H. Zhang. DEM/CFD-DEM Modelling of Non-spherical Particulate Systems: Theoretical Developments and Applications. *Powder Technology*, 302:108–152, 2016. ISSN 1873328X. doi: 10.1016/j.powtec.2016.07.010. URL http://dx.doi.org/10.1016/j.powtec.2016.07.010.

K.H. Zum Gahr. Microstructure and Wear of Materials. In *Tribology Series*, volume 10, chapter 4, pages 80–131. 1987. ISBN 9780444427540. doi: 10.1016/S0167-8922(08)70722-3.

A

Table Data

In section A.1 a list of containments inside a polymetallic nodule, originated from the Clarion-Clipperton Zone (CCZ), can be found (Mero, 1965). The followup section, section A.2, provides tables with weight and volume information of the nodules during the density measurements. An overview of the test data of the single nodule experiments in the Abrasive Wear Tester (AWT), chapter 4, can be found in section A.3. The obtained value for the specific wear rate (k) for polymetallic nodules is calculated using two approaches. The result of these approaches can be found in section A.4. In the last section of this appendix, section A.5, additional data for the batch experiments of chapter 5 is provided in tables.

A.1. Metal Content Data

Additional data for subsection 2.3.1. This table, Table A.1, gives a list of weight percentages of elements inside polymetallic nodules from the Clarion-Clipperton Zone (CCZ). The bold symbols denote the elements which are most usable and promising for our modern industry.

Table A.1: Weight percentages of elements inside polymetallic nodules from the CCZ (Mero, 1965)

Element	Chemical Symbol	Average [%]	Minimum [%]	Maximum [%]
Manganese	**Mn**	**24.2**	**8.2**	**41.1**
Iron	**Fe**	**14.0**	**2.4**	**26.6**
Silicon	Si	9.4	1.3	20.1
Aluminum	Al	2.9	0.8	6.9
Sodium	Na	2.6	1.5	4.7
Calcium	Ca	1.9	0.8	4.4
Magnesium	Mg	1.7	1.0	2.4
Nickel	**Ni**	**0.99**	**0.16**	**2.0**
Potassium	K	0.8	0.3	3.1
Titanium	Ti	0.67	0.11	1.7
Copper	**Cu**	**0.53**	**0.028**	**1.6**
Cobalt	**Co**	**0.35**	**0.014**	**2.3**
Barium	Ba	0.18	0.08	0.64
Lead	Pb	0.09	0.02	0.36
Strontium	Sr	0.081	0.024	0.16
Zirconium	Zr	0.063	0.009	0.12
Vanadium	V	0.054	0.021	0.11
Molybdenum	Mo	0.052	0.01	0.15
Zinc	Zn	0.047	0.04	0.08
Yttrium	Y	0.033	0.016	0.045
Boron	B	0.029	0.007	0.06
Lanthanum	La	0.016	0.009	0.024
Ytterbium	Yb	0.0031	0.0013	0.0066
Chromium	Cr	0.001	0.001	0.007
Scandium	Sc	0.001	0.001	0.003
Gallium	Ga	0.001	0.0002	0.003
Silver	Ag	0.0003	-	0.0006

A.2. Density Measurement Data

Additional data for subsection 2.3.4. In Table A.2 the volume, mass and particle density of the wet polymetallic nodules are given. The decrease in mass of the nodules due to the drying process in the furnace (at 105°C) is given in Table A.3. The last table of this appendix provides an overview of the physical properties of the ten tested nodules of the Kinderdijk batch, Table A.4. It summarizes the results of the water content (w), particle density (ρ_{part}), dry density (ρ_{dry}), porosity (n), void ratio (e) and solids density (ρ_s).

Table A.2: Wet density measurements of the ten tested Kinderdijk nodules

Nodule	V_{nod} [cm^3]	m_w [g]	ρ_{part} [g/cm^3]
1	277.09	478.59	1.727
2	307.88	542.71	1.763
3	215.51	385.55	1.789
4	261.69	454.91	1.738
5	215.51	349.72	1.623
6	169.33	286.12	1.690
7	23.09	39.26	1.700
8	7.70	10.67	1.386
9	3.85	6.52	1.694
10	2.89	4.78	1.656

Table A.3: Wet and dry weight of the ten tested Kinderdijk nodules

Nodule	m_w [g]	m_d [g] (2h)	m_d [g] (4h)	m_d [g] (22h)	m_d [g] (28h)
1	478.59	453.21	427.20	336.16	332.21
2	542.71	513.03	478.56	372.41	367.92
3	385.55	361.95	336.85	269.38	266.99
4	454.91	424.85	394.21	314.63	312.04
5	349.72	322.05	297.08	240.93	239.80
6	286.12	264.97	242.51	196.18	195.20
7	39.26	33.57	29.36	25.19	25.19
8	10.67	8.81	7.67	7.01	7.01
9	6.52	4.89	4.35	4.11	4.11
10	4.78	4.07	3.57	3.27	3.27

Table A.4: Physical properties of the ten tested Kinderdijk nodules

Nodule	w [%]	ρ_{part} [g/cm^3]	ρ_d [g/cm^3]	n [%]	e [-]	ρ_s [g/cm^3]
1	44.06	1.727	1.199	52.93	1.12	2.547
2	47.51	1.763	1.195	56.89	1.32	2.772
3	44.41	1.789	1.239	55.12	1.23	2.761
4	45.79	1.738	1.192	54.70	1.21	2.632
5	45.84	1.623	1.113	51.11	1.05	2.276
6	46.58	1.690	1.153	53.80	1.16	2.495
7	55.86	1.700	1.091	61.06	1.57	2.801
8	52.21	1.386	0.911	47.65	0.91	1.740
9	58.64	1.694	1.068	62.75	1.68	2.867
10	46.18	1.656	1.133	52.42	1.10	2.381
Average	**48.71**	**1.677**	**1.127**	**54.84**	**1.21**	**2.497**

A.3. Test Data of the Measurements in the Abrasive Wear Tester

The first five of tests were used to find the optimal rotational velocity of the Abrasive Wear Tester (Figure 4.2). It was found that at 1.75 Hz the nodule does not get lifted from the pipe wall or starts rolling along the wall. Test number 8 was lost. Table A.5 provides additional data for section 4.4. In Table A.5, 'Weight 1' represents the mass of the nodule before the test (m_1) and 'Weight 2' gives the mass of the nodule after a test (m_2). The remaining mass (m_n) is given in %. The remaining mass are plotted against sliding distance in Figure 4.17.

Table A.5: Test data of the measurements in the Abrasive Wear Tester

Measurement					Nodule properties		
Testnumber	Weight 1 [g]	Weight 2 [g]	Remaining mass [%]	Total sliding distance [m]	Length [cm]	Width [cm]	Height [cm]
Test 6 (>65)	376.92	371.45	98.55	600	10	8	6
Test 7 (>65)	289.75	285.50	98.53	600	9	6.5	6
Test 9 (>65)	328.83	322.91	98.20	690	10	8	6
Test 10 (>65)	405.13	404.06	99.74	900	11	8	7.5
Test 11 (>65)	345.63	343.68	99.44	300	11	7	6
Test 12 (>65)	432.10	429.70	99.44	300	12	7	6
Test 13 (>65)	410.78	406.52	98.96	375	10	7	6
Test 14 (>65)	Broken Nodule			300	10	8	7
	340.83	314.07	92.15				
Test 15 (>65)	383.46	377.70	98.50	300	10	8	7
Test 16 (>65)	364.90	360.17	98.70	300	9	7	7
Test 17 (>45)	287.60	287.40	99.93	225	9.5	7	5.5
Test 18 (>70)	629.36	625.75	99.43	210	12	8.5	8
Test 19 (>70)	431.48	429.72	99.59	210	10	8.5	7
Test 20 (>70)	Broken Nodule			330	11	9	7
	540.13	499.22	92.43				
Test 21 (>65)	Broken Nodule			210	10	7	6
	361.21	350.48	97.03				
Test 22 (>70)	504.14	501.84	99.54	210	10	9	5.5
Test 23 (>70)	502.54	497.85	99.07	375	10.5	10	6
Test 24 (>70)	460.99	454.84	98.67	510	10.5	10	5
Test 25 (>70)	384.57	381.21	99.13	450	9	8	5.5
Test 26 (>65)	344.00	339.72	98.76	450	11	8	6
Test 27 (>65)	309.73	305.87	98.75	690	10	6	6

A.4. Specific Wear Rate Check

The data from Figure 4.18 is represented in Table A.6. The first column corresponds with Equation 4.3 and the second column corresponds with Equation 4.14.

$$k = \frac{m_1 - m_2}{F_N \, s \, \rho_{part}} \tag{4.3 revisited}$$

$$k = \frac{m_1 - m_2}{F_N \, \rho_{part} \left(\int_{t=t_0}^{t=t_n} v_{slide} \, dt \right) n_{slide}} \tag{4.14 revisited}$$

Table A.6: Specific wear rates, depending on distance and velocity integral

Test number	k · (10^{-9}) [m^2/N]	k · (10^{-9}) [m^2/N]
6	4.2977	4.3383
7	4.2936	4.3254
9	4.6129	4.6490
10	0.5126	0.5161
11	3.3212	3.3374
12	3.3512	3.3621
13	4.8474	4.8803
15	8.7834	8.8876
16	7.7147	7.7576
17	0.5450	0.5471
18	4.9795	5.0781
19	3.4121	3.4025
22	3.8880	3.9161
23	4.4125	4.5090
24	4.5905	4.6246
25	3.3610	3.4001
26	4.7368	4.8018
27	3.2378	3.2462
Average	**4.1610**	**4.1988**

A.5. PSD data of the Batch Experiments

This section provides additional Particle Size Distribution (PSD) data from section 5.3. As stated in subsection 5.3.1, the batch experiments in Kinderdijk are split into two parts. First a distance of 4500 meters is tested, whereafter the tester is completely emptied and the batch is sieved. The test of the first 4500 meter will be referred to as *'Test 1'*. The test of the second 4500 meter will be referred to as *'Test 2'*. The recalculated weight is based on Equation 5.2.

In Table A.7 the cumulative diameter data of Figure 5.2 is given.

Table A.7: PSD data from the Freiberg testing trials (Dasselaar et al., 2018b)

d_X [mm]	d_X [mm] initial	d_X [mm] after 8900 m
d_0	1.84	0.06
d_{10}	6.26	3.32
d_{20}	7.85	6.36
d_{30}	9.00	8.11
d_{40}	10.20	9.60
d_{50}	11.40	11.30
d_{60}	12.80	13.00
d_{70}	14.10	15.00
d_{80}	16.70	18.40
d_{90}	20.10	23.20
d_{100}	29.40	29.00

In Table A.8, the PSD data is given before *Test 1*. The data in Table A.8 corresponds with Figure 5.4. In Table A.9, the cumulative diameter of the both the initial Kinderdijk and Freiberg batch are compared.

Table A.8: Complete PSD data of the Kinderdijk nodules, before *Test 1*

Initial (before *Test 1*)				
Sieve size [mm]	Weight [g]	Recalculated weight [g]	Percentage [%]	Cum. Percentage [%]
31.5	0	0.00	0.00	100.00
22.4	214.6	145.93	7.95	92.05
16	504.2	342.86	18.69	73.36
11.2	831.5	565.42	30.82	42.54
8	600.7	408.48	22.26	20.27
5.6	185.1	125.87	6.86	13.41
1.4	361.9	246.09	13.41	0.00
Total	2698.00	1843.64	100	

Table A.9: Initial PSD data of the Kinderdijk batch and the Freiberg batch

d_X [mm]	d_X [mm] initial Kinderdijk	d_X [mm] initial Freiberg
d_0	1.40	1.84
d_{10}	4.53	6.26
d_{20}	7.90	7.85
d_{30}	9.40	9.00
d_{40}	10.84	10.20
d_{50}	12.36	11.40
d_{60}	13.92	12.80
d_{70}	15.48	14.10
d_{80}	18.27	16.70
d_{90}	21.70	20.10
d_{100}	31.50	29.40

In Table A.10, the PSD data is given after *Test 1*. The data in Table A.10 corresponds with Figure 5.14. In Table A.11, the cumulative diameters of the Kinderdijk batch are given before and after *Test 1*.

Table A.10: Complete PSD data of the Kinderdijk nodules, after *Test 1* in the Abrasive Wear Tester

4500 m (after *Test 1*)				
Sieve size [mm]	Weight [g]	Recalculated weight [g]	Percentage [%]	Cum. Percentage [%]
31.5	0.00	0.00	0.00	100.00
22.4	169.90	115.53	6.68	93.32
16	353.80	240.58	13.90	79.42
11.2	515.50	350.54	20.26	59.16
8	509.20	346.26	20.01	39.15
5.6	170.80	116.14	6.71	32.44
4	130.00	88.40	5.11	27.33
2.8	56.00	38.08	2.20	25.13
2	58.82	58.82	3.40	21.73
1.4	24.59	24.59	1.42	20.31
1	44.89	44.89	2.59	17.71
0.710	50.25	50.25	2.90	14.81
0.500	58.00	58.00	3.35	11.46
0.250	112.32	112.32	6.49	4.97
0.180	35.29	35.29	2.04	2.93
0.125	23.96	23.96	1.38	1.54
0.090	12.64	12.64	0.73	0.81
0.075	5.17	5.17	0.30	0.51
0.063	2.62	2.62	0.15	0.36
0.045	4.51	4.51	0.26	0.10
0.038	1.03	1.03	0.06	0.04
0.000	0.71	0.71	0.04	0.00
Total	2339.98	1730.31	100.00	

Table A.11: PSD data of the Kinderdijk nodules, before and after *Test 1*

d_X [mm]	d_X [mm] before *Test 1*	d_X [mm] after *Test 1*
d_0	1.40	0.00
d_{10}	4.53	0.44
d_{20}	7.90	1.35
d_{30}	9.40	4.84
d_{40}	10.84	8.14
d_{50}	12.36	9.74
d_{60}	13.92	11.40
d_{70}	15.48	13.77
d_{80}	18.27	16.27
d_{90}	21.70	20.87
d_{100}	31.50	31.50

In Table A.12, the PSD data is given after *Test 2*. The data in Table A.12 corresponds with Figure 5.15. In Table A.13, the cumulative diameters of the Kinderdijk batch are given before *Test 1* and after *Test 2*.

Table A.12: Complete PSD data of the Kinderdijk nodules, after *Test 2* in the Abrasive Wear Tester

9000 m (After *Test 2*)				
Sieve size [mm]	Weight [g]	Recalculated weight [g]	Percentage [%]	Cum. Percentage [%]
31.5	0.00	0.00	0.00	100.00
22.4	136.40	92.75	5.47	94.53
16	254.20	172.86	10.19	84.35
11.2	473.60	322.05	18.98	65.37
8	540.60	367.61	21.66	43.71
5.6	199.10	135.39	7.98	35.73
4	78.50	53.38	3.15	32.58
2.8	25.50	17.34	1.02	31.56
2	18.02	76.83	4.53	27.04
1.4	10.42	35.01	2.06	24.97
1	7.29	52.18	3.07	21.90
0.710	8.54	58.79	3.46	18.43
0.500	8.44	66.44	3.92	14.52
0.355	8.95	65.11	3.84	10.68
0.250	7.98	64.14	3.78	6.90
0.180	5.32	40.60	2.39	4.51
0.125	5.28	29.24	1.72	2.79
0.090	4.48	17.12	1.01	1.78
0.075	6.42	11.59	0.68	1.09
0.063	2.13	4.75	0.28	0.81
0.045	6.46	10.97	0.65	0.17
0.038	1.05	2.08	0.12	0.04
0.000	0.05	0.76	0.04	0.00
Total	1808.74	1696.99	100.00	

Table A.13: PSD data of the Kinderdijk nodules, initial and after *Test 2*

d_X [mm]	d_X [mm] before *Test 1*	d_X [mm] after *Test 2*
d_0	1.40	0.00
d_{10}	4.53	0.34
d_{20}	7.90	0.84
d_{30}	9.40	2.52
d_{40}	10.84	6.88
d_{50}	12.36	8.93
d_{60}	13.92	10.41
d_{70}	15.48	12.37
d_{80}	18.27	14.90
d_{90}	21.70	19.55
d_{100}	31.50	31.50

B

Details of the Modelling Algorithms

First, in section B.1, details of the mesh grid and the used program to generate the mesh (Gmsh) is given. In the followup section, section B.2, figures of the mesh are shown. For future research, or for those who are interested, the source code of the mesh is given in section B.3. Two algorithms, which are used in the simulations in chapter 6, are explained in detail in section B.4 and section B.5, respectively. The first algorithm search the closest grid coordinates with respect to the particle, and the second algorithm is used to recognize contact with the pipe wall. The last section, section B.6, provides figures from the 3D MATLAB simulations.

B.1. Mesh Grid (Gmsh)

The mesh used for the CFD calculations is made by using Gmsh. Gmsh is a: “three-dimensional finite element mesh generator with built-in pre- and post-processing facilities”[1]. The mesh programmed by Gmsh can be opened by OpenFOAM. The advantage of Gmsh is that the mesh can also be adapted using a script, the script (source code) of the mesh can be found in section B.3.

At the inlet and outlet of the model, the center of is made of a square mesh. The total length and width is one-third of the pipe diameter. The mesh size is 18x18 cells. Towards the outside of the pipe, the cell size decreases, because more detail is required in calculations. Each quarter of the pipe consists of 18x19 cells, thus a total of 1368 cells. With the cells from the squared center, the total number of cells at the inlet becomes 1692. It is chosen to make the squared cells at the center as cubic as possible. Therefore the number of layers in the pipe is the height of the pipe, divided by the width of one cell in the squared section. This holds that the total number of cells in the model is equal to 1895040, see Table B.1. The total number of grid point is equal to 1938209. Figures of the mesh, shown in the Gmsh environment, are given in section B.2.

Table B.1: Specification of the total number of cells in the pipe geometry

	Total cells in direction				
Q_4 section	Length	Width	Height	Total cells in Q_4	Total cells in pipe geometry
Square section	9	9	1120	90720	362880
Circular section	19	18	1120	383040	1532160
					1895040

B.2. Figures of the Mesh

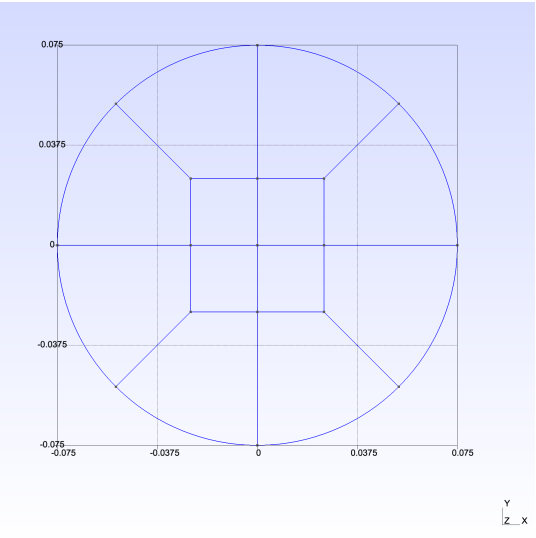

Figure B.1: Inlet / Outlet of the pipe (2D representation without mesh grid)

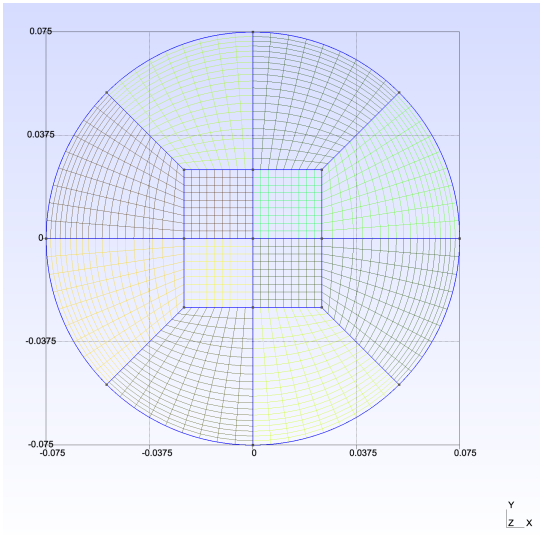

Figure B.2: Inlet / Outlet of the pipe (with 2D meshing)

[1] Official website of Gmsh

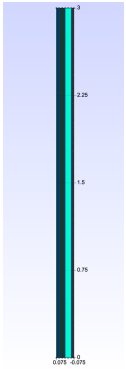

Figure B.3: 3D overview of the pipe

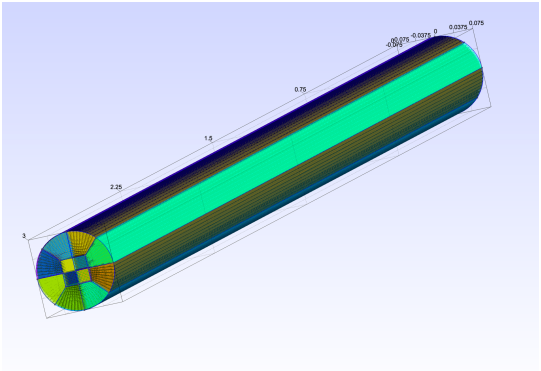

Figure B.4: Complete pipe (with 3D meshing)

B.3. Source Code of the Mesh

```
// Define geometry of the pipe

  r = 0.075;        // Radius of the pipe [m]
  H = 20*(2*r);     // Height of the pipe [m]
  b = 3;            // Geometry inner square (r/b)
  A = 10;           // Transfinite line (number of sides (#boxes = sides-1))
  L = 20*56;        // Layers in extrude
  C = 2;            // Ratio between square mesh and mesh in circle part

// Define points
Point(1) = {0, 0, 0, 1.0};
Point(2) = {(r/b), 0, 0, 1.0};
Point(3) = {r, 0, 0, 1.0};
Point(4) = {0, (r/b), 0, 1.0};
Point(5) = {0, r, 0, 1.0};
Point(6) = {(r/b), (r/b), 0, 1.0};
Point(7) = {r*Cos(Pi/4), r*Sin(Pi/4), 0, 1.0};

// Define lines
Line(1) = {1, 2};
Line(2) = {2, 3};
Line(3) = {1, 4};
Line(4) = {4, 5};
Line(5) = {2, 6};
Line(6) = {4, 6};
Line(7) = {6, 7};

Circle(8) = {7, 1, 3};        // Outer circle arc lower
Circle(9) = {7, 1, 5};        // Outer circle arc upper

// First quarter
Line Loop(1) = {1, 5, -6, -3};
Plane Surface(1) = {1};
Transfinite Surface{1} = {1, 2, 6, 4};
Transfinite Line {1, 3, 5, 6, 8, 9} = A Using Progression 1.0;
Recombine Surface{1};

Line Loop(2) = {4, -9, -7, -6};
Plane Surface(2) = {2};
Transfinite Surface {2} = {5, 7, 6, 4};
```

```
Transfinite Line {2, 4, 7} = C*A Using Progression 0.95;
Recombine Surface {2};

Line Loop(3) = {2, -8, -7, -5};
Plane Surface(3) = {3};
Transfinite Surface {3} = {2, 6, 7, 3};
Recombine Surface {3};

// Make second quarter
Symmetry {0, 1, 0, 0} { Duplicata { Surface{1}; Surface{3}; Surface{2}; }}

// Make complete circle
Symmetry {1, 0, 0, 0} { Duplicata { Surface{2}; Surface{3}; Surface{1}; Surface{10}; Surface{15}; Surface{20}; }}

Transfinite Line {27, 32, 40, 34, 41, 50, 45, 30, 25, 14, 12, 13, 22, 17} = A Using Progression 1;
Transfinite Line {-26, 29, -46, 21, -18} = C*A Using Progression 0.95;

Transfinite Surface {10} = {13, 2, 1, 17};
Transfinite Surface {15} = {13, 30, 2, 3};
Transfinite Surface {20} = {17, 42, 13, 30};
Transfinite Surface {23} = {53, 4, 5, 49};
Transfinite Surface {28} = {49, 61, 60, 53};
Transfinite Surface {33} = {4, 53, 60, 1};
Transfinite Surface {38} = {60, 98, 17, 1};
Transfinite Surface {43} = {61, 60, 98, 115};
Transfinite Surface {48} = {98, 115, 42, 17};
Recombine Surface {23, 28, 33, 43, 48, 38, 20, 10, 15};

// Extrude to pipe
Extrude {0, 0, H} { Surface{23}; Surface{2}; Surface{3}; Surface{1}; Surface{33}; Surface{28}; Surface{43}; Sur-
face{38}; Surface{48}; Surface{20}; Surface{10}; Surface{15}; Layers{L}; Recombine;}

Transfinite Volume{1} = {49, 53, 4, 5, 116, 117, 126, 122};
Transfinite Volume{2} = {6, 4, 5, 7, 133, 137, 116, 117};
Transfinite Volume{3} = {2, 6, 7, 133, 137, 138, 139, 3};
Transfinite Volume{4} = {2, 1, 121, 116, 137, 6, 138, 4};
Transfinite Volume{5} = {141, 126, 53, 4, 1, 60, 121, 116};
Transfinite Volume{6} = {126, 141, 60, 122, 143, 61, 49, 53};
Transfinite Volume{7} = {60, 61, 143, 141, 154, 98, 115, 150};
Transfinite Volume{8} = {1, 60, 98, 17, 164, 121, 141, 154};
Transfinite Volume{9} = {150, 154, 164, 166, 42, 17, 98, 115};
Transfinite Volume{10} = {166, 164, 177, 173, 17, 13, 30, 42};
Transfinite Volume{11} = {121, 138, 2, 1, 17, 164, 13, 177};
Transfinite Volume{12} = {138, 2, 3, 139, 177, 13, 30, 173};

// Surfaces (Patches in openFoam)
Physical Surface("inlet") = {3, 2, 1, 23, 33, 28, 43, 38, 10, 15, 20, 48};
Physical Surface("outlet") = {182, 72, 94, 160, 138, 116, 314, 292, 226, 204, 248, 270};
Physical Surface("wall") = {85, 107, 63, 239, 195, 182, 173, 305, 261};

// Volumes (Cells in openFoam)
Physical Volume("grid") = {7, 9, 8, 6, 5, 1, 2, 4, 3, 11, 12, 10};
```

B.4. Particle Coordinates with respect to the Grid

As stated before, in section B.1, the grid consist of 1938209 grid points. In order to check which grid point (x_g, y_g, z_g) is the closest to the center of the particle (x_p, y_p, z_p), this algorithm is made. In short it works as follows, first the coordinates of the particle are subtracted from each grid particle. Next, the absolute value is taken from each element and then each row is summed. This results into a single vector with positive values, whereas the minimal value corresponds to the shortest distance between the particle and the specific grid point. An example is given in the followup. Lets assume a grid is given by matrix A and the particle coordinates are given by vector p represented in Equation B.1.

$$A = \begin{bmatrix} 0 & 6 & 13 \\ 1 & 7 & 14 \\ 2 & 8 & 15 \\ 3 & 9 & 16 \\ 4 & 10 & 17 \end{bmatrix} \quad p = \begin{bmatrix} 2 & 9 & 16 \end{bmatrix} \tag{B.1}$$

Now, the particle coordinates are subtracted from matrix A, which results into matrix B. Next, the absolute value of all elements is taken. Thereafter, the sum of each element per row of matrix $|B|$ is taken, resulting in vector C, whereas the lowest value will correspond to the closest grid point with respect to the particle coordinates. The result is given in Equation B.2, where the minimum value is encircled.

$$B = A - p = \begin{bmatrix} -2 & -3 & -3 \\ -1 & -2 & -2 \\ 0 & -1 & -1 \\ 1 & 0 & 0 \\ 2 & 1 & 1 \end{bmatrix} \rightarrow |B| = \begin{bmatrix} 2 & 3 & 3 \\ 1 & 2 & 2 \\ 0 & 1 & 1 \\ 1 & 0 & 0 \\ 2 & 1 & 1 \end{bmatrix} \rightarrow C = \begin{bmatrix} 8 \\ 5 \\ 2 \\ \textcircled{1} \\ 4 \end{bmatrix} \tag{B.2}$$

Thus, with the determination of the lowest value, the corresponding row with the closest grid coordinates can be found in matrix A. Now, the fluid information of this point is substituted into the equation of drag, Equation 6.20, for example.

B.5. Contact Recognition with the Pipe Wall

This algorithm is made for subsection 6.3.2, Contact Recognition with the Pipe Wall. The distance between the center of the pipe and the center of the particle is continuously calculated during a simulation. If this distance becomes larger than the radius of the pipe minus the particle boundary, which is marked as the particle diameter with small springs, then the springs become active. The moment that the springs become active the coordinates of the center of the particle will be used to determine the interaction point at the wall. For the vertical coordinate it is obvious that interaction point is on the same level as the center of the particle. For the determination of the x- and y-coordinates of the interaction point, polar coordinates are used. With the x- and y-coordinates of the particle the angle with the horizontal axis can be calculated. Using the angle and the radius of the pipe, the interaction coordinates can be obtained.

If the particle springs are still active in the followup time step, which holds that the hydrodynamic forces exerting on the particle are greater than the spring forces on the particle, a sliding path on the wall is the result. During a simulation all the time steps with active springs are saved in a vector. Two cases can be distinguished, point interaction and sliding interaction. These two cases can be separated by checking the derivative between the times.

An example of the recognition procedure is given in the following. Let the interaction times, in seconds, be given by vector T_1 in Equation B.3.

$$T_1 = [1, 2, 3, 4, 5, 8, 10] \tag{B.3}$$

Then, the differences between each element of vector T_1 can be obtained. The result is given by Equation B.4, in which m represents the number of elements in the vector.

Consecutive time steps can be recognized when the difference between the time steps is equal to one, so when $dT_1 = 1$. This is used recognize point interactions, because when $dT_1 \neq 1$, it holds that time steps in Equation B.3 are not consecutive. For sliding path recognition, if $dT_1 \neq 1$ in Equation B.4, it will be set to zero. This gives the following result:

$$\begin{gathered} dT_1 = [T_1(2) - T_1(1),\ T_1(3) - T_1(2),\ \ldots,\ T_1(m) - T_1(m-1)] \\ \rightarrow dT_1 = [1,\ 1,\ 1,\ 1,\ 3,\ 2] \\ dT_1 \neq 1 \rightarrow dT_1 = 0 \\ \rightarrow dT_1 = [1,\ 1,\ 1,\ 1,\ 0,\ 0] \end{gathered} \tag{B.4}$$

The result from Equation B.4 is used to make a new time vector, T_2. This time vector will start with a zero, followed by vector dT_1 and end with a zero. The result is given by Equation B.5. Next, the differences between each element of vector T_2 are taken again (as also done for vector T_1 in Equation B.4.

$$\begin{gathered} T_2 = [0,\ [dT_1],\ 0] \\ \rightarrow T_2 = [0,\ 1,\ 1,\ 1,\ 1,\ 0,\ 0,\ 0] \end{gathered} \tag{B.5}$$

From Equation B.5 it can be seen that the time vector T_2 is one element longer than the original time vector T_1. So, if the difference between the elements of T_2 is taken, which results into a vector which is one element shorter in general, the lengths will be equal again. This holds that the elements in dT_2 will directly correspond to the elements of time vector T_1. But first, the differences of T_2 are taken and the result can be seen in Equation B.6.

$$dT_2 = [1,\ 0,\ 0,\ 0,\ -1,\ 0,\ 0] \tag{B.6}$$

With the result of Equation B.6 the consecutive time steps in T_1 can be distinguished. When $dT_2 = 1$ the consecutive steps start and if $dT_2 = -1$ it ends. So, from dT_2 it can be seen that the first element until the fifth element in T_1 will be consecutive. The result of the consecutive time steps is given by Equation B.7.

$$T_{cons} = [1,\ 2,\ 3,\ 4,\ 5] \tag{B.7}$$

The result of Equation B.7 can be used to plot the path on the pipe wall and obtain its length. The sliding length is determined with Equation B.8. In Equation B.8, vector $\boldsymbol{x}_i$ represents a vector containing the x-, y- and z-coordinates, respectively.

$$\begin{gathered} \Delta \boldsymbol{x}_i\,(T_{cons}) = \boldsymbol{x}_i\,(T_{end}) - \boldsymbol{x}_i\,(T_{start}) \\ \rightarrow L_{cons} = \sqrt{\left(\sum_{i=1}^{3} (\Delta \boldsymbol{x}_i\,(T_{cons}))^2\right)} \end{gathered} \tag{B.8}$$

B.6. Figures from 3D MATLAB Simulations

In the model sensitivity analysis of subsection 6.4.3, three different particles were used. The largest particle, referred to as *Particle 1*, had a particle diameter equal to one-third of the pipe diameter. *Particle 2* consists of a particle diameter equal to one-sixth of the pipe diameter, and *Particle 3* of one-tenth of the pipe diameter. In Figure B.5, a point interaction of *Particle 1* with the pipe wall can be seen. A sliding interaction of this particle with the wall is given by Figure B.6. The algorithm that detects a sliding or point interaction was explained in the previous section, section B.5. In Figure B.7 and Figure B.8 the point and sliding interaction of *Particle 2* can be seen. This is also shown in Figure B.9 and Figure B.10, only then for *Particle 3*.

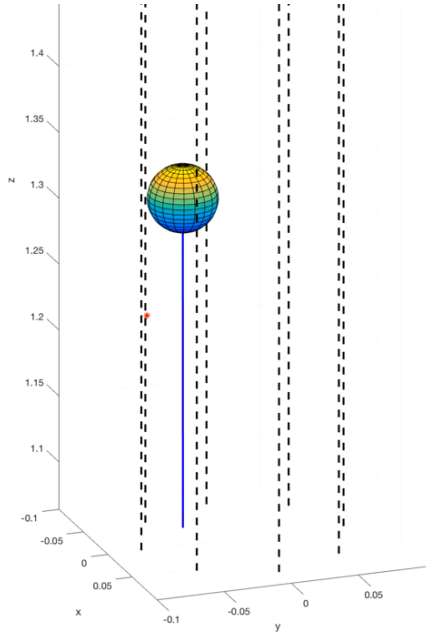

Figure B.5: *Particle 1* with a point interaction with the pipe wall

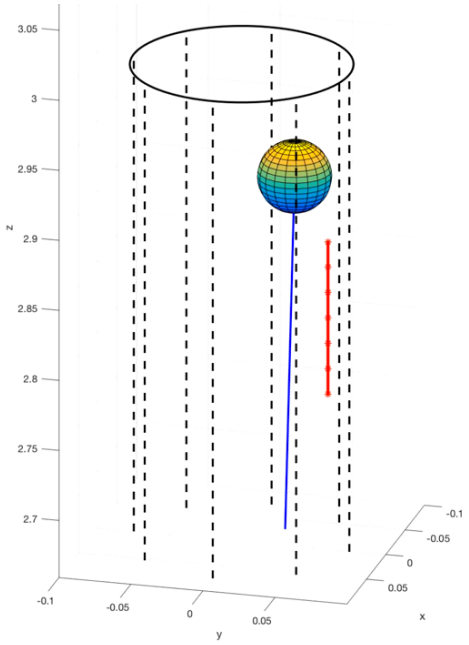

Figure B.6: *Particle 1* with a sliding interaction with the pipe wall

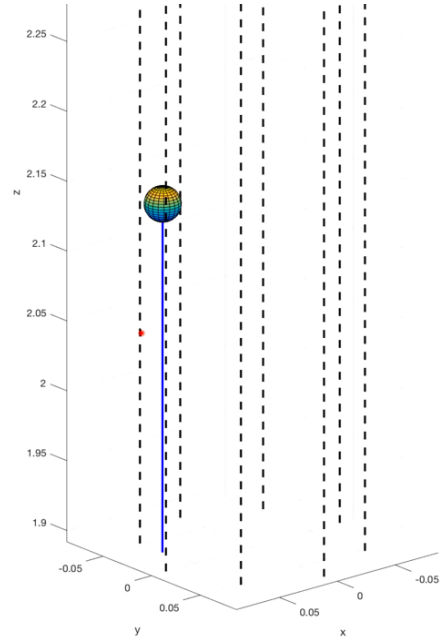

Figure B.7: *Particle 2* with a point interaction with the pipe wall

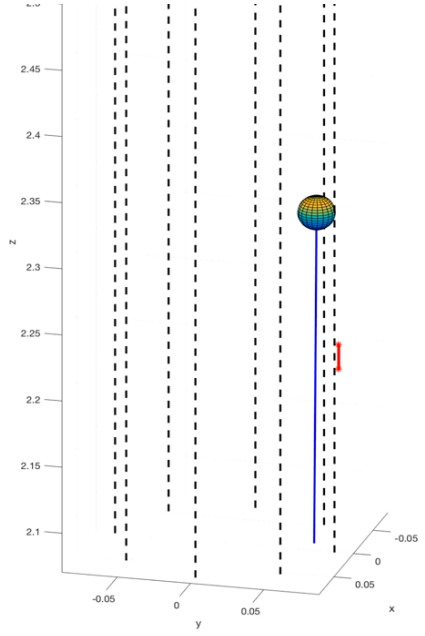

Figure B.8: *Particle 2* with a sliding interaction with the pipe wall

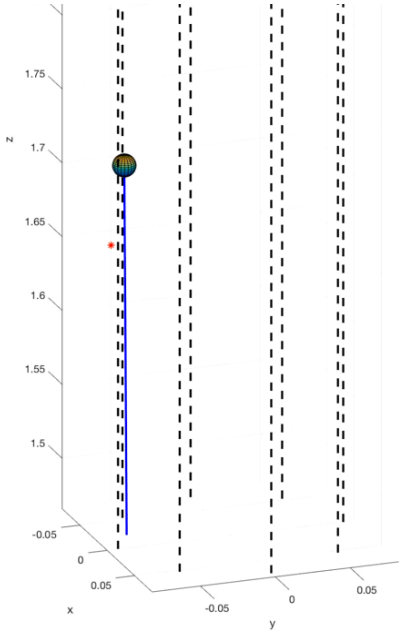

Figure B.9: *Particle 3* with a point interaction with the pipe wall

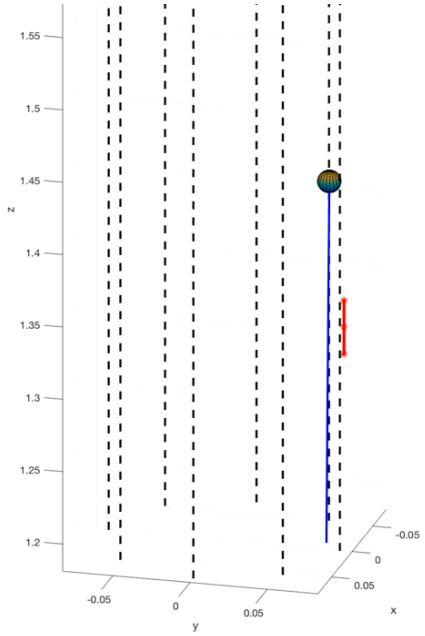

Figure B.10: *Particle 3* with a sliding interaction with the pipe wall

C

Additional Information of the Kinderdijk Experiments

The sections in this appendix are related to chapter 4, Scale Model Experiments I. In section C.1 a measurement scheme is provided to perform measurements using the Abrasive Wear Tester, Figure 4.2. The second section of this appendix, section C.2, gives a kinematic analysis of the test setup. The goal of the kinematic analysis was to calculate the pipe angle during the motions of the setup (AWT) and compare this result with the measured pipe angle.

C.1. Measurement Scheme for the Abrasive Wear Tester

This scheme will work as a guide to perform the wear measurements using the Abrasive Wear Tester at the MTI laboratory in Kinderdijk.

Before the test run

1. Determine the weight of the nodule (m_1) and its dimensions (data in Excel sheet)
2. Place the nodule in the **empty** pipe while its having a horizontal position
3. Close both of the ends of the tester with flanges and fill it completely with water
4. Determine on beforehand the desired sliding distance (s) and denote the total number of steps
5. Place the pipe in its initial test position (right end closest to the ground)
6. Start the camera for video recording and the timer (Dewesoft)
7. Start the electrical engine

During the test run

1. Control if the nodule is still sliding along the lower pipe wall and if its not broken
2. Keep an eye on the number of steps (distance)
3. Export the video file (at least 5 sliding distances from both sides)
4. Place a new nodule (for a new test) in a bucket filled with water

After the test run

1. After the desired measurement length is reached, stop the engine (the pipe should be in its initial position again)
2. Empty the pipe, collect the fines as good as possible (collect at least one liter from the outflow)
3. Open the flange (make sure the nodule does not fall) and weigh the nodule (m_2)
4. Open the other flange and clean the rest of the pipe (collect the fines)
5. Place the fines in the oven (not too long due to the clay content!)
6. Sieve the fines when possible
7. Fill in the Excel sheet with the obtained data

C.2. Kinematic Solution of the Pipe Angle of the Abrasive Wear Tester

Due to the geometry of the rod mechanism it is chosen to simulate the motion of the pipe in MATLAB. Therefore, the kinematics of the rod mechanism should be understood. To simplify the rod mechanism it is divided into two triangles, which can be seen in Figure C.1. Next, all the triangles are calculated to make a simulation in order to keep track of the pipe angle.

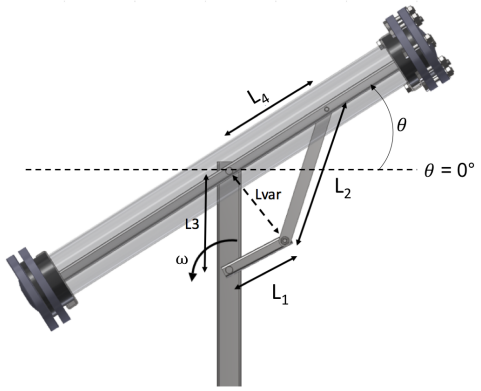

Figure C.1: Schematic representation of the pipe angle

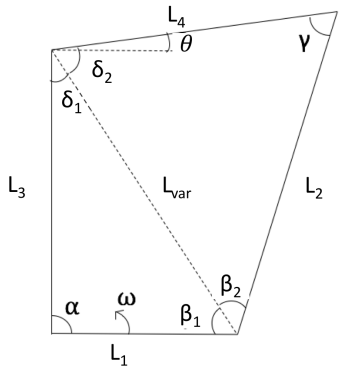

Figure C.2: Schematic representation of the angles of the AWT

The first triangle consists of L_1, L_3 and L_{var}. Whereas L_1 represents the rotating bar connected to the electrical engine, L_3 marks the distance between both of the rotational points and L_{var} is an imaginary bar between the end of L_1 and the central rotation point of the pipe. The angles of the triangle and the length of L_{var} can be calculated with the cosine-rule. The rule, for the first triangle, is defined as follows:

$$L_{var}^2 = L_1^2 + L_3^2 - 2L_1L_3\cos(\alpha) \tag{C.1}$$

Next, L_{var} is calculated as a function of the rotational angle α, which drives the system.

$$L_{var} = \sqrt{L_3^2 + L_1^2 - 2L_1L_3\cos(\alpha)} \tag{C.2}$$

Interesting about Equation C.2 is the situation when α equals 0° or 270°, this holds that the rotating section L_1 is pointing upwards or downwards. What follows is that the first triangle does not exist, so at this point $\delta_1 = 0°$. At the other angles of α the cosine-rule can be applied again, which is represented in Equation C.3.

$$\delta_1 = \begin{cases} \cos^{-1}\left(\frac{L_{var}^2+L_3^2-L_1^2}{2L_{var}L_3}\right) & \text{if: } 0° \le \alpha < 90° \quad \text{and if: } 270° < \alpha < 360° \\ 0 & \text{if: } \alpha = 90° \quad \text{and if: } \alpha = 270° \\ -\cos^{-1}\left(\frac{L_{var}^2+L_3^2-L_1^2}{2L_{var}L_3}\right) & \text{if: } 90° < \alpha < 270° \end{cases} \tag{C.3}$$

With the angle intervals of Equation C.3, β_1 can be calculated. Because the angles shift from positive to negative, it is necessary to take the absolute value of the angle(s) on some intervals. The calculation of β_1 is represented in Equation C.4.

$$\beta_1 = \begin{cases} 180 - \alpha - \delta_1 & \text{if: } 0° \le \alpha < 90° \\ 180 - |\alpha| - |\delta_1| & \text{if: } 90° \le \alpha \le 270° \\ |\alpha| - 180 - \delta_1 & \text{if: } 270° < \alpha < 360° \end{cases} \tag{C.4}$$

With the three angles of the first triangle known, it is possible to calculate the angles of the second triangle. First is started with angle δ_2, which is, together with δ_1, part of the pipe angle. With the information of the variable length of L_{var} during the rotation of rod L_1 and the cosine-rule, δ_2 is calculated as follows.

$$\delta_2 = \cos^{-1}\left(\frac{L_{var}^2 + L_4^2 - L_2^2}{2\,L_{var}\,L_4}\right) \tag{C.5}$$

The same principle as δ_2 holds for β_2, the calculation is shown by Equation C.6. And together with γ it will form the second triangle of 180° again. The angles β_2 and γ are not exclusively needed in order to calculate the pipe, but these are used to check the system.

$$\beta_2 = \cos^{-1}\left(\frac{L_{var}^2 + L_2^2 - L_4^2}{2\,L_{var}\,L_2}\right) \tag{C.6}$$

$$\gamma = 180 - \delta_2 - \beta_2 \tag{C.7}$$

Now that all the angles of both of the triangles are known, the pipe angle θ, is computed as represented by Equation C.8. The pipe angle θ represents the angle of the pipe compared to the horizontal, therefore 90° is subtracted from the summation of angles δ_1 and δ_2, so that the pipe angle is zero if it is in a horizontal position. The horizontal is represented as a dotted black line in Figure C.1.

$$\theta = \delta_1 + \delta_2 - 90 \tag{C.8}$$

An animation of the experimental setup is made, in order to calculate the pipe angle during a rotation of the setup. A snapshot of the animation can be seen in Figure C.3, whereas the dotted green line represents the imaginary bar between the triangles.

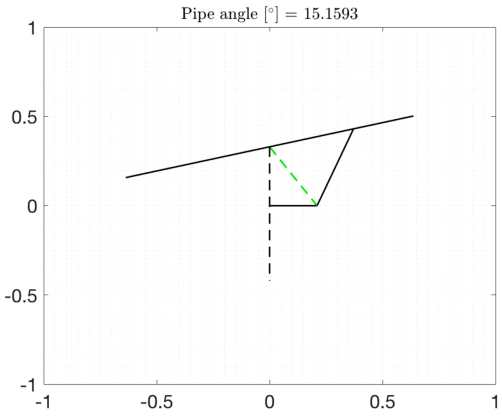

Figure C.3: Animation of the experimental setup (snapshot)

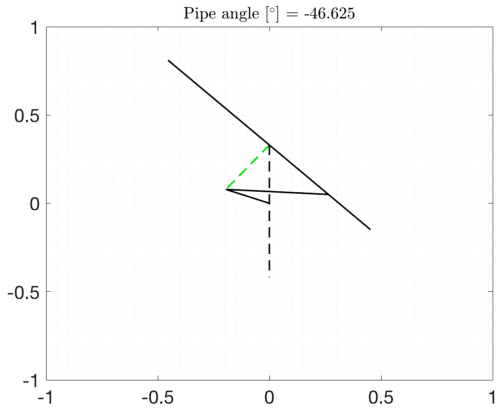

Figure C.4: Animation of the experimental setup (snapshot)